Alma Mater Studiorum - Università di Bologna

DOTTORATO DI RICERCA IN

CHIMICA

Ciclo 33

Settore Concorsuale: 03/A2 - MODELLI E METODOLOGIE PER LE SCIENZE CHIMICHE

Settore Scientifico Disciplinare: CHIM/02 - CHIMICA FISICA

NANOSTRUCTURED SYSTEMS FOR ELECTROCATALYSIS OF REDUCTION REACTIONS FOR ENERGY CONVERSION APPLICATIONS

Presentata da: Jacopo Isopi

Coordinatore Dottorato

Domenica Tonelli

Supervisore

Massimo Marcaccio

Co-supervisore

Francesco Paolucci

Esame finale anno 2021

Abstract

The ORR is a fundamental process for sustaining life and it is also utilized in biosensing analysis. Additionally, this process is applicable to artificial energy devices such as fuel cells and metal-air based batteries. The reaction requires a platinum-based catalyst to reduce the activation barrier. This is neither cheap nor environmentally friendly to extract and is one of the weakest parts of the fuel cell technology. One of the most promising materials as alternative catalysts are carbon-based, graphene and carbon nanotubes (CNT) derivatives. Subsequently, ORR on a carbon-based substrate involves the less efficient two electrons process and the optimal four electrons process. New synthetic strategies to produce tunable graphene-based materials utilizing graphene oxide (GO) as a base inspired the first part of this work. The key term for these materials would be that they are "tunable", the synthesis procedures for their preparation should be based on a slight modification of known and relatively easy chemical processes. Oxidized parts of the molecules can be reduced in the presence of compounds capable of adding functional groups or heteroatoms to the carbon lattice.

Hydrogen Evolution Reaction (HER) from water using sustainable electrocatalysts and powered by renewable energy from solar and wind can be used to store green energy in to molecular hydrogen which can then be burned directly or through fuel cells with oxygen. HER too is a slow process requiring also platinum or palladium as catalyst. Cheaper alternatives as nickel and nickel alloys are not as efficient as platinum but by engineering the surface topography on a nano-level and the surface environment, the current performance can be just a baseline to improve upon. In the second part of this work, we develop and use a technique for Ni nanoparticles electrodeposition using $NiCl_2$ as precursor in the presence of ascorbate ligands. Electrodeposition of nano-nickel onto flat glassy carbon (GC) and onto nitrogen-doped reduced graphene oxide (rGO-N) substrates are studied. In a preliminary study, the effects of a thin layer polymer of intrinsic microporosity (PIM-1) are investigated on (i) nickel nanoparticle growth and (ii) enhancing electrocatalysis by suppressing interfacial hydrogen bubble formation. In 0.5 M NaCl (as a model for seawater) nickel nanoparticle electrocatalysts grown directly into PIM-1 show activity approaching that observed for bare platinum nanoparticles when increasing the current density.

Using CO_2 in the atmosphere as carbon feedstock, CO_2RR can be used to generate carbon neutral fuels and, as a possible long game strategy, even capture back carbon out of the atmosphere effectively reverting the cumulative effects of centuries of fossil fuels usage obtaining useful building blocks for the chemical industry as byproduct. State of the art catalysts for CO_2RR requires rare metals rhenium or rhodium. In recent years significant research has been done on non-noble metals

and molecular systems to use as electro and photo-catalysts (artificial photosynthesis). As Cu-Zn alloys show good CO_2RR performance, here we applied the same nanoparticle electrosynthesis technique using as precursors $CuCl_2$ and Cl_2Zn and observed successful formation of the nanoparticles and a notable activity in presence of CO_2. Using rhenium complexes as catalysts is another popular approach and di-nuclear complexes have a positive cooperative effect. More recently a growing family of pre-catalysts based on the earth-abundant metal manganese, has emerged as a promising, cheaper alternative. Here we study the cooperative effects of di-nuclear manganese complexes derivatives when used as homogeneous electrocatalysts, as well as a rhenium functionalized polymer used as heterogeneous electrocatalyst. Lastly, we characterized the electrochemical behavior of three π-extended Zn porphyrin systems on which electron delocalization over a conjugation of polycyclic aromatic hydrocarbon and the metal ion significantly decreases the electrical potential needed to drive the chemical reduction of CO_2.

Table of contents

Chapter III

Chapter IV

Preface

In the book The Mysterious Island, Jules Verne described a world where “water will one day be employed as fuel, that hydrogen and oxygen which constitute it, used singly or together, will furnish an inexhaustible source of heat and light, of an intensity of which coal is not capable”. The book was published in 1874, meaning this vision is nearly 150 years old. Its almost disturbing actuality should not surprise us, really. The chemical science of energy production and storage is grounded in the abundance and simplicity of few key reactions already known centuries ago. Oxidation of carbon and hydrogen into CO_2 and H_2O is the easiest way to release energy chemically, from coal in a powerplant, to sugar in a biological system, to the flame of a blowtorch burning molecular hydrogen. On the other hand, reduction of CO_2 and water splitting are the opposite reactions trough which energy is trapped in chemical bonds since cyano-bacteria were alive on this planet. With few exceptions, the energy economy, both biological and artificial, on this world is based on few fundamental reactions: Oxygen Reduction Reaction (ORR), CO_2 Reduction Reaction (CO_2RR) , Hydrogen reduction and carbon oxidation. The environmental impact of traditional fossil fuels used to meet the ever-growing global energy demand is causing and will continue to cause problems that will require a great scientific and technological effort for a transition to a more sustainable landscape. Renewable sources as wind and solar hold great promises in this regard, but the electrical world cannot solve the problem remaining in its bubble: chemical energy vectors are crucial in the optimal integration of renewable sources. Using fuel cells as well as metal-air batteries for powering the transport sector or for grid stabilization would help the transition and bridge the renewable grid to the devices powered by an internal source of energy. There is one major problem about these reactions: they are slow and require expensive noble metal catalysts to run. In many instances the world natural supply of these resources happens to be in politically unstable areas and are cause of controversies about human rights violations in mines and geopolitical disputes between superpowers. The key strategy for bridging the gap between renewable grid energy production and the chemical energy vectors is to develop cheap and durable electrocatalysts for mass production.

The ORR is a fundamental process for sustaining life and it is also utilized in biosensing analysis. Additionally, this process is applicable to artificial energy devices such as fuel cells and metal-air based batteries. The reaction requires a platinum-based catalyst to

reduce the activation barrier. This is neither cheap nor environmentally friendly to extract and is one of the weakest parts of the fuel cell technology. One of the most promising materials as alternative catalysts are carbon-based, graphene and carbon nanotubes (CNT) derivatives. Subsequently, ORR on a carbon-based substrate involves the less efficient two electrons process and the optimal four electrons process. New synthetic strategies to produce tunable graphene-based materials utilizing graphene oxide (GO) as a base inspired the first part of this work. The key term for these materials would be that they are "tunable", the synthesis procedures for their preparation should be based on a slight modification of known and relatively easy chemical processes. Oxidized parts of the molecules can be reduced in the presence of compounds capable of adding functional groups or heteroatoms to the carbon lattice.

Hydrogen Evolution Reaction (HER) from water using sustainable electrocatalysts and powered by renewable energy from solar and wind can be used to store green energy in to molecular hydrogen which can then be burned directly or through fuel cells with oxygen. HER too is a slow process requiring also platinum or palladium as catalyst. Cheaper alternatives as nickel and nickel alloys are not as efficient as platinum but by engineering the surface topography on a nano-level and the surface environment, the current performance can be just a baseline to improve upon. In the second part of this work, we develop and use a technique for Ni nanoparticles electrodeposition using $NiCl_2$ as precursor in the presence of ascorbate ligands. Electrodeposition of nano-nickel onto flat glassy carbon (GC) and onto nitrogen-doped reduced graphene oxide (rGO-N) substrates are studied. In a preliminary study, the effects of a thin layer polymer of intrinsic microporosity (PIM-1) are investigated on (i) nickel nanoparticle growth and (ii) enhancing electrocatalysis by suppressing interfacial hydrogen bubble formation. In 0.5 M NaCl (as a model for seawater) nickel nanoparticle electrocatalysts grown directly into PIM-1 show activity approaching that observed for bare platinum nanoparticles when increasing the current density.

Using CO_2 in the atmosphere as carbon feedstock, CO_2RR can be used to generate carbon neutral fuels and, as a possible long game strategy, even capture back carbon out of the atmosphere effectively reverting the cumulative effects of centuries of fossil fuels usage obtaining useful building blocks for the chemical industry as byproduct. State of the art catalysts for CO_2RR requires rare metals rhenium or rhodium. In recent years significant research has been done on non-noble metals and molecular systems to use as electro and photo-catalysts (artificial photosynthesis). As Cu-Zn alloys show good CO_2RR

performance, here we applied the same nanoparticle electrosynthesis technique using as precursors $CuCl_2$ and Cl_2Zn and observed successful formation of the nanoparticles and a notable activity in presence of CO_2. Using rhenium complexes as catalysts is another popular approach and di-nuclear complexes have a positive cooperative effect. More recently a growing family of pre-catalysts based on the earth-abundant metal manganese, has emerged as a promising, cheaper alternative. Here we study the cooperative effects of di-nuclear manganese complexes derivatives when used as homogeneous electrocatalysts, as well as a rhenium functionalized polymer used as heterogeneous electrocatalyst. Lastly, we characterized the electrochemical behavior of three π-extended Zn porphyrin systems on which electron delocalization over a conjugation of polycyclic aromatic hydrocarbon and the metal ion significantly decreases the electrical potential needed to drive the chemical reduction of CO_2.

Chapter I

Electrocatalysis of Oxygen Reduction Reaction by Graphenic Systems.

Introduction to ORR

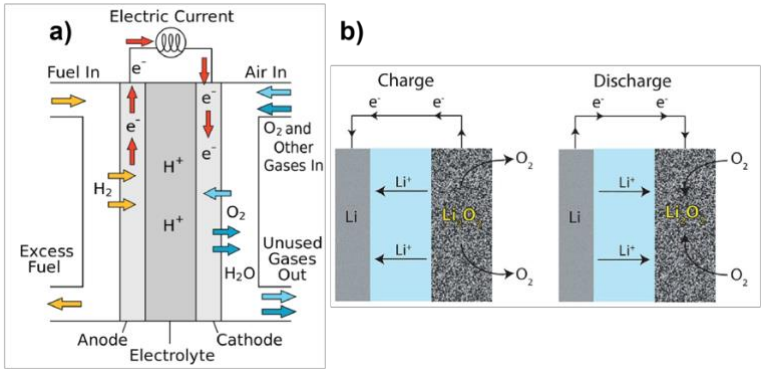

Scheme 1 Functioning principle of (a) an H_2/O_2 fuel cell and (b) a lithium-air battery. Two electrochemical devices using oxygen reduction reaction at the cathode.

Oxygen Reduction Reaction (ORR) is a fundamental process for life as it is involved in the cellular respiration. It is also very important from a technological standpoint, in particular in the field of energy conversion, in systems as fuel cells and metal-air batteries. Such energy devices are indeed of great interest, as they can allow environmentally sustainable energy production with water as the only waste product.[1,2] Moreover, metal-air batteries have theoretically a rather high energy density and mastering such technology would represent a great step forward to overcome the obsolescence of internal combustion engines.[3]

In real world application devices, it is desirable for the ORR to occur at potentials close to thermodynamic equilibrium potential values as much as possible. The ORR has a very slow kinetic and thus it needs an electrocatalyst for an efficient utilization. The difference from the thermodynamic potential and where the reaction actually takes place is called overpotential η and it is what the catalyst minimizes.

$$\eta = E - E_{eq}$$

The expression relating the over-potential, η, and the net current is known as the Butler-Volmer equation:

$$i = i_0 \left\{ exp\left(\beta \frac{nF}{RT}\eta\right) - exp\left(-[1-\beta]\frac{nF}{RT}\eta\right)\right\}$$

where i is the ORR current density, i_o is the exchange current density, n is the number of electrons transferred in the rate-determining step, β is the transfer coefficient, η is the over-potential of ORR, F is the Faraday constant, R is the gas constant and T is the temperature in K.

The first term in the Butler-Volmer equation represents the anodic reaction, while the second term represents the cathodic reaction. A plot of the Butler-Volmer equation gives the polarization curve as shown in Figure 1.

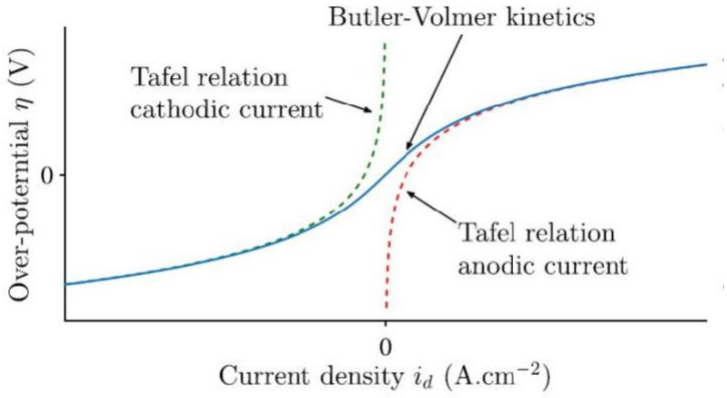

Figure 1 Current density in relation with overpotential according to the Butler-Volmer equation.

At high overpotentials region, the Butler-Volmer equation simplifies to Tafel equation:

$$i_a = i_0 exp\left(\beta \frac{nF}{RT}\eta\right)$$

$$\eta_a = b_a log\left(\frac{i_a}{i_o}\right)$$

$$b_a = 2.303\frac{RT}{\beta nF}$$

A plot of η versus log(i_c), also known as the Tafel plot, gives a linear relationship, with slope 2.303RT/βnF, known as the Tafel slope where the intercept yields i_o. The Tafel slope gives the information about the mechanism of the ORR. The higher the Tafel slope, the

faster the overpotential increases with current density. With a low Tafel slope, the electrochemical reaction is able to obtain a high current density, at low overpotential. Better catalysts lead to lower slopes.

The oxygen reduction can mainly follow two different pathways: a less efficient 2-electrons way, where oxygen is converted in peroxide, and a 4-electrons way that leads to water production.[4–6] To have an optimal catalyst, it is required not only the minimization of η, but also a high selectivity towards the most efficient 4-electrons process (Scheme 2).

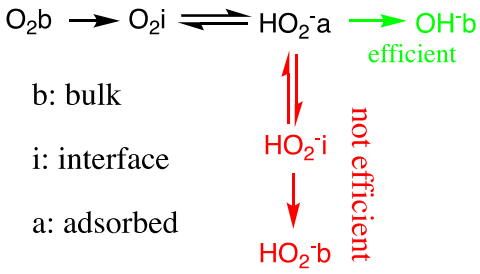

Scheme 2 The two main reaction pathways ORR undergoes on a catalyst surface: a less efficient one involving the transfer of 2 electrons (red) and a more valuable one leading to the complete reduction of O_2 with the exchange of 4 electrons (green).

As shown in *table 1* standard potentials for O_2 reduction in H_2O and H_2O_2 are highly influenced by pH and, in the case of the formation of the superoxide O_2^-, of the solvent. The pH susceptibility is caused by the fact that the process involves a protonic/ hydroxyl transfer coupled with the electron transfer:

$$O + mH^+ + ne^- \leftrightarrow R$$

So, from the relationship:

$$E^f = E^0 - 2.303\frac{mRT}{nF}pH$$

you get a lowering of the thermodynamic potential of 58 mV per unit of pH

Table 1 Principal reduction reactions of O_2 in acidic, alkaline conditions and in aprotic solvents. Standard potentials of super-oxides in aprotic solvents are not reported as are strongly influenced by the specific solvent used.

Electrolyte	ORR reactions	Thermodynamic electrode potential at standard conditions, V
Acidic aqueous solution	$O_2 + 4H^+ + 4e^- \rightarrow H_2O$	1.229
	$O_2 + 2H^+ + 2e^- \rightarrow H_2O_2$	0.70
	$H_2O_2 + 2H^+ + 2e^- \rightarrow 2H_2O$	1.76
Alkaline aqueous solution	$O_2 + H_2O + 4e^- \rightarrow 4OH^-$	0.401
	$O_2 + H_2O + 2e^- \rightarrow HO_2^- + OH^-$	–0.065
	$HO_2^- + H_2O + 2e^- \rightarrow 3OH^-$	0.867
Non-aqueous aprotic solvents	$O_2 + e^- \rightarrow O_2^-$	a
	$O_2^- + e^- \rightarrow O_2^{2-}$	b

Platinum based materials are the current state of the art catalysts used in commercial devices with a high selectivity towards the 4-electrons process and an overall sensible activity and stability, although it offers limited commercialization of fuel cells due to its limited availability on Earth and high cost.[7,8] The importance of ORR, together with the need of expensive catalysts, mainly platinum-based, has stimulated the scientific community to the search for a cheaper, efficient and reliable substitute of the precious metal.

Among the variety of new materials, one of the most promising for energy conversion devices is graphene,[9] which is a good candidate thanks to its high electronic conduction properties, that makes it similar to a metal,[10] resistant to corrosion and low production costs. Although the catalytic mechanism of Carbon materials for the ORR is not completely understood yet, many authoritative studies indicate that it is made of several elementary steps which include (i) O_2 adsorption, (ii) electron transfers from carbon nanomaterials (CNMs) to O_2 and (iii) the subsequent formation of high-energy intermediates.[6,11,12] Such reaction steps are very difficult to be investigated because the generated intermediates have very short lifetimes and cannot be easily isolated. An important issue in the study of the graphene-based catalytic materials is related to the adsorption phenomena and the presence of doping atoms (substitution of carbon with an heteroatom in the lattice) that extensively boost the catalyst capability.[13–15]

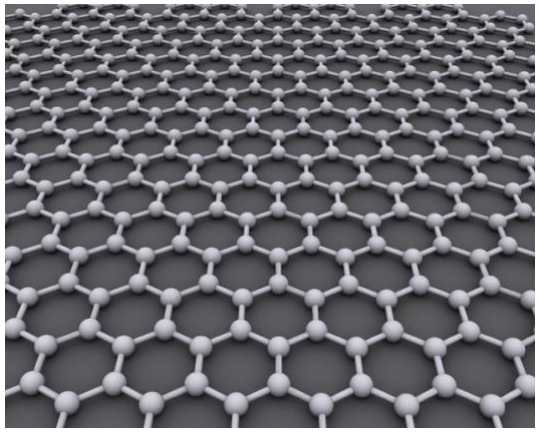

Figure 2 The repeating pattern of carbon atoms in a graphene sheet.

Graphene is a quasi b-dimensional material consisting of a single layer of sp^2 carbon forming an hexagonal lattice of atoms of ideally infinite size in every direction. Each carbon atom is about a = 1.42 Å from its three neighbors, with each of which it shares one σ bond. The fourth bond is a π bond, which is oriented in the z direction (out of the plane). The p-orbital of each atom takes part to the π bonds, which are then hybridized together to form what are referred to as the π and π* bands of a molecule-wide conjugated system spatially located above and below the atoms lattice. These bands are responsible for most of the peculiar electronic properties of graphene. Its chemical, thermal and mechanical properties are so promising that big investments into its research are being devolved all over the world with the potential of huge technological breakthroughs.[16,17]

Thermal and Electronic Properties

Graphene has thermic and electronic properties similar to those of metals as, in fact, its electronic states are metal-like since the gap between valence and conduction band is near to zero. In π conjugated systems, the HOMO-LUMO gap depends on the size of the system itself shrinking asymptotically to zero on the bigger end.[18] When the size of the polyaromatic molecule, and consequently the conjugated system, is fairly big, we can consider it as graphene and we have in almost all cases that the material expresses metallic properties. More precisely, graphene is a zero-gap semiconductor because the conduction and valence bands meet at the Dirac (Figure 3) points with the Fermi level coinciding with the conjunction points in the case of a neutral graphene (or non-doped). Traditional

semiconductors have a finite band gap while graphene has a nominal gap of zero. Note that, the Fermi level in graphene is always within the conduction or valence band while in traditional semiconductors the Fermi level often falls within the band gap when pinned by impurity states.

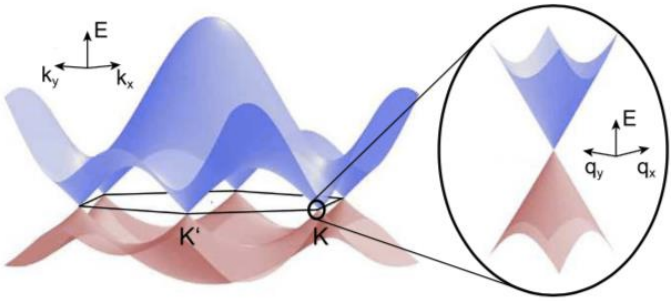

Figure 3 Tight-binding band structure of graphene. The red and blue energy surfaces are functions of momentum in two dimensions (k_x and k_y). The six contact points are divided in two equivalent points K and K^i.

More intuitively π electrons are free to move across the molecule and respond with a net electric current when any potential is applied. Charge mobility is high, of the order of 15000 $cm^2V^{-1}s^{-1}$ since electrons, that travel in the π conjugated system and move over and below the carbon atoms grid, are getting no interference by it.[10] Holes have the same mobility of electron[19] and both are almost not affected by temperature in a range between 10 K and 100 K.[20–22]

From a thermal standpoint the similarities with metals continues since graphene is a good heat conductor as well. Electrons and phonons travel with ease through the carbon grid carrying thermal energy with them with little to no chance to dissipate it outside the plane. This makes graphene both a conductor along the directions it extends through and an insulator through the axis perpendicular to the plane.[23]

Mechanical and Chemical Properties

Graphene is a perfect hexagonal lattice of carbons held together by strong sp^2 covalent bonds that gives to the material a mechanical strength 100 times superior of that of stainless steel. Trying to "break" the material means breaking the internal covalent forces of a molecule ideally as big as the material itself.[24] Chemical properties depends by the

number of layers juxtaposed, the size of the layer, the presence of defects in the grid, by the edges and by the chemical group functionalities it can have.[25]

Synthesis of Graphene

Figure 4 From left to right: Andrej Konstantinovič Gejm and Konstantin Sergeevič Novosëlov. Their work on graphene where the first stable sheet was successfully isolated earned them the Nobel Prize in Physics in 2010.

Numerous are the methods for the synthesis of many graphenic materials, each with different yields, material quality and coherence developed over the years since Gejm and Novoselov first demonstrated the possibility to isolate graphene sheets with the famous "scotch method" in 2004. We should start by dividing them into two major groups: the "top down" and the "bottom up" methods.

Top Down Methods

These are the methods that involve mainly exfoliation from graphite. To date there is no method that can match mechanical exfoliation for producing high-quality, high-mobility graphene flakes. Developed by Geim and Novoselov,[10] the exfoliation process uses HOPG (highly oriented pyrolytic graphite) as a precursor. The HOPG is subjected to an oxygen plasma etching to create 5 μm deep mesas and these mesas are then pressed into a layer of photoresist. The photoresist is baked and the HOPG is cleaved from the resist. Scotch tape is used to repeatedly peel flakes of graphite from the mesas. These thin flakes are then released in acetone and captured on the surface of a Si/SiO_2 wafer. The downside of this technique is the time-consuming process that limits to small scale production.

Chemical and electrochemical exfoliation are faster but sacrifice quality of the end product. Most importantly the final product in these cases is graphene oxide (GO), a material that has lost the exceptional electric properties of regular graphene, but has gained some interesting properties of its own and has to be reduced in an extra step to obtain graphene either by thermal or chemical means.[26] The polar oxy- and OH groups formed during the oxidation process render graphite oxide hydrophilic, and it can be chemically exfoliated in several solvents, including water.[27] GO is useful because its individual layers are hydrophilic, in contrast to graphite, so it can be suspended in water by sonication.[28,29]

The chemical methods to produce GO were all developed before 1960. The most commonly employed is the Hummers procedure.[30] This process treats graphite in an anhydrous mixture of sulfuric acid, sodium nitrate, and potassium permanganate for several hours, followed by the addition of water. The resulting material is graphite oxide hydrate, which contains approximately 23% water. Understandably, the degree of oxidation strongly affects the in-plane electrical and thermal conductivity of graphene oxide. Increased introduction of oxygen groups into the graphene lattice interrupts the sp^2 hybridization of electron orbitals. GO can be reduced to a form referred to as *reduced Graphene Oxide* (rGO) where the most reactive sites of the molecule (mostly epoxide groups) are eliminated, partially recovering the coordinated structure and leading to a middle ground material with improved electrical conductivity and unaffected hydrophilicity. One other method of production of graphene technically considered top down is the longitudinal unzipping of carbon nanotubes (CNT) by first suspending them in sulphuric acid and then treating them with $KMnO_4$. The resulting tapes of graphene are called graphene nanoribbons and were found to be conducting, but electronically inferior to large scale graphene sheets due to the presence of oxygen defect sites.[31] All these methods have the disadvantage of contaminating the product with chemicals from the synthesis itself and a less than ideal defect concentration in comparison to many bottom up methods.

Bottom Up Methods

As an opposite philosophy, bottom up methods involve simple chemical precursors that acts as building blocks providing carbon for a controlled growth of the graphene sheet in presence of specific catalysts.

One of the most popular techniques is Chemical Vapor Deposition (CVD) were carbon is supplied in gas form and a metal surface is used as both catalyst and template to grow the graphene layer. Nickel or copper foil is used as catalyst in a methane atmosphere and temperature as high as 1000 °C. A single layer of high quality graphene is achievable in this way and once the process is finished the metal is removed by etching leaving a single sheet of graphene of macroscopic sizes.[32–34]

Another bottom up technique is the chemical synthesis, were specific precursor molecules (polyphenylenes) transform by intra-molecule reaction in a Polycyclic Aromatic Hydrocarbon (PAH) with sizes of the order of tens of nanometers. These PAH can be called nano-graphene and by inter-molecular reactions more PAH can merge until, in theory, getting regular graphene which can be viewed as an endless PAH. This technique is limited by the solubility of the growing molecule, that inevitably precipitate off solution when becomes too massive. On record there are top sized of 40 nm.[35]

Graphene as ORR Catalyst

ORR requires a rather high activation energy, that in a usable device a catalyst is necessary. Some carbon based materials work as catalysts when used as anode materials as discovered by Dai's group in 2009.[36] To be effective an ORR catalyst must be able to swiftly go through the following steps: O_2 molecules adsorption at the surface, electron transport from anode to adsorbed O_2 molecules, weakening and breaking of O = O bindings and removing the produced OH^- ions back to the solution.[37] A scheme for the mechanism on carbon substrates is theorized as follows:[38]

1. $O_{2(blk)} \rightarrow O_{2(ads)}$
2. $O_{2(ads)} + e^- \rightarrow \left[O_{2(ads)}\right]^-$
3. $\left[O_{2(ads)}\right]^- \rightarrow O^-_{2(ads)}$
4. $O^-_{2(ads)} + H_2O \rightarrow HO_{2(ads)} + OH^-$
5. $HO_{2(ads)} + e^- \rightarrow HO^-_{2(ads)}$
6. $HO^-_{2(ads)} \rightarrow HO^-_{2(blk)}$

There are usually two adsorption types on the surface of carbon materials based on the computational charge density distribution. One is the side-on O_2 molecule adsorption (Yeager model), the other is the end-on O_2 molecule adsorption (Pauling model).[36] Pristine carbon materials including carbon black, CNTs, graphene, carbon nanofibers (CNFs), mesoporous carbon, or activated carbon, are inactive as ORR electrocatalysts. However, carbon materials can be remarkably enhanced in activity by heteroatom doping, such as N or B doping to the point of becoming competitive as electrocatalyst alternatives. Heteroatoms can be introduced into carbon materials experimentally by either in situ doping in the synthesis process of carbon materials or post-treatment of the mixture of pre-synthesized carbon materials and dopant-containing materials. Contents ratios and chemical states of the dopants on the surface of doped carbon materials are usually taken in detail by X-ray photoelectron spectroscopy (XPS).

The most studied dopants are sulphur, boron, phosphorus, fluorine and nitrogen. Boron and nitrogen are neighbor elements of carbon on the periodic table, thus they have similar atomic dimensions and, consequently their inclusion in the lattice change the electrical properties with minimal structural deformation.[13,39–44] It is worth to note that N doping has shown to enhance significantly the ORR activity of carbon nanomaterials in numerous works.[43,45–52] Nitrogen, having higher electronegativity than carbon, inserted inside the carbon matrix alters the electric distribution creating a dipole between the C and the N atoms that interacts with the O_2 adsorbing it thus becoming the active reaction site (Scheme 3).[53] As for the electron transfer to the adsorbed molecule, the introduction of nitrogen atoms as dopants perturbs the homogeneous π-electron density and hence changes the electronic surface state,[54] which often increases its chemical activity and electron conductivity.

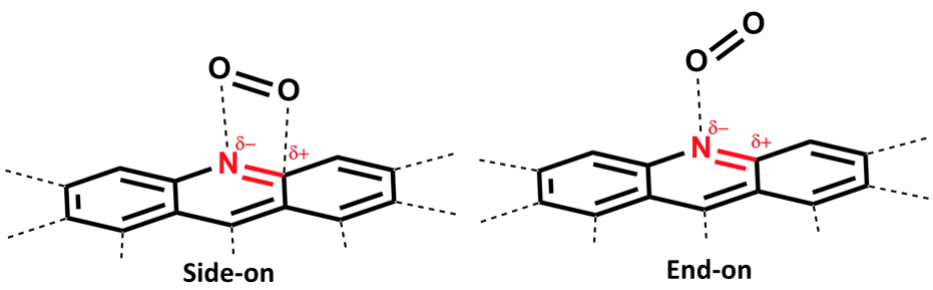

Scheme 3 Two models of interaction of the oxygen molecule with the active site.

Tunneling microscopy and theoretical calculations have shown that N-doping of CNT increases the Fermi energy to facilitate electrons to be promoted on the conduction band, thus exhibiting metallic properties.[55,56] The observed increase in the localized density of states at the Fermi level could cause considerable electron emissions at sufficiently low voltages,[57] thereby increasing catalytic activities of carbon materials for electron-transfer and ORR.

Boron, on the other hand, have lower electronegativity than that of carbon, the positively polarized boron atoms in the graphite lattice attract the nucleophilic oxygen molecules leading to efficient end on chemisorption and first O-O bond cleavage. Than induces a side-on configuration where the second O-O bond is broken, which is the most energetically expensive (rate determining) step, to form a very stable oxidized boron species (C-O-B-O-C).[58] The two O are then reduced independently to H_2O by taking p electrons of the conjugated carbon network and protons from the solution.[59] The protruding lobe of the HOMO-1 of the material will then have maximal overlap with the lowest unoccupied molecular orbital (LUMO) of a triplet O_2 to form an end-on adsorption, thus facilitating the ORR process.[60,61]

The configuration of the doping heteroatom depends on the chemical environment; different functionalities with the same heteroatom interact differently both with the O_2 molecule and the carbon atoms nearby, leading to different catalytic properties. The doped nitrogen atoms near the edge, for instance, provide strong chemical oxygen adsorption hence high catalytic activity towards the ORR.[62,63] However, are still controversial the details of the difference in behavior between the pyridinic or graphitic nitrogen for the ORR. In general, graphitic nitrogen determines the limiting current density, whereas the pyridinic nitrogen improves the onset potential for the ORR.[64]

Methods and Principles

The study of catalytic properties of the sample materials in this work have been carried out using Cyclic Voltammetry (CV), ChronoAmperometry (CA) coupled with Scanning Electrochemical Microscopy (SECM) and X-ray Photoelectron Spectroscopy (XPS) for elemental analysis.

Instrumentation: The Electrochemical Cell

An electrochemical cell is a vessel made of inert material (usually Pyrex glass) hermetically isolated from the external atmosphere if needed were an electrolytic solution connect 3 electrodes: the Work Electrode (WE), Counter Electrode (CE) and Reference Electrode (RE).

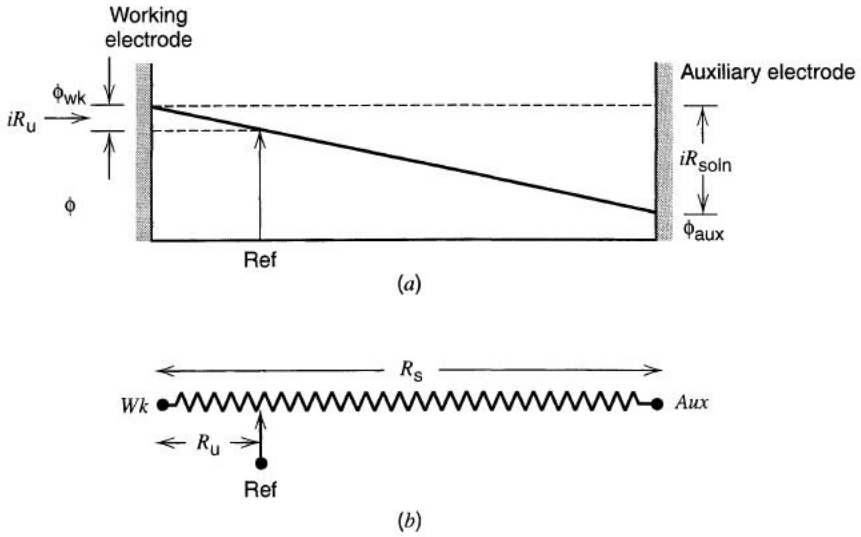

Scheme 4 Ohmic potential drop between WE and RE (a) makes a good practice to not position them to far away. Schematic representation of the electrical components (b).

Electrical current flows between WE and CE during the experiment. WE is different from CE as it is the surface were the potential chosen by the operator is applied. The machine that controls the potential is called "potentiostat" and it does so thanks to the RE. The surface of the RE is at a known and stable potential thanks to the fact that it is in a chemical equilibrium with its own internal solution. The machine reads that potential as zero. Only an infinitesimal amount of current passes between the RE and the other

electrodes during the measure so that the zero in this frame does not change due to ohmic drop. The potentiostat apply the voltage between WE and CE but monitors the precise electric potential values between the RE and the WE keeping the surface of the WE at the intended potential (Scheme 5). The output signal is the current measured flowing between WE and CE.

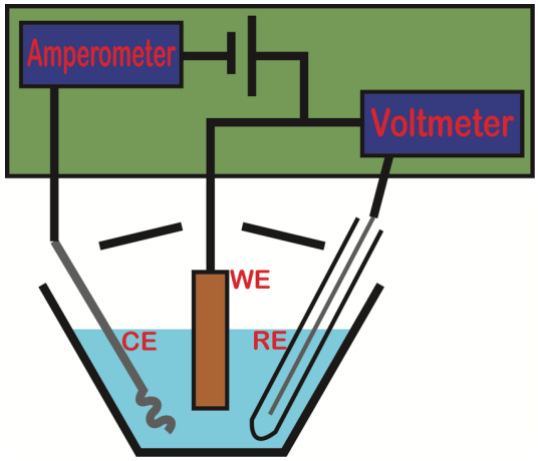

Scheme 5 Functional scheme of an electrochemical setup made of potentiostat and cell.

Cyclic Voltammetry and Chronoamperometry

CV is the most used electrochemical technique both for gaining qualitative and quantitative information of redox processes of species in solution or on the WE surface. Thanks to this technique are obtainable both information about the thermodynamics and kinetics of a redox reaction. During a CV a variable potential is applied having a triangular wave (V vs t) and cycling at will. The scan output is a graph (voltammogram) of current intensity (I) in Ampere versus potential (E) in Volts. During the scan the redox processes are visible as current waves.

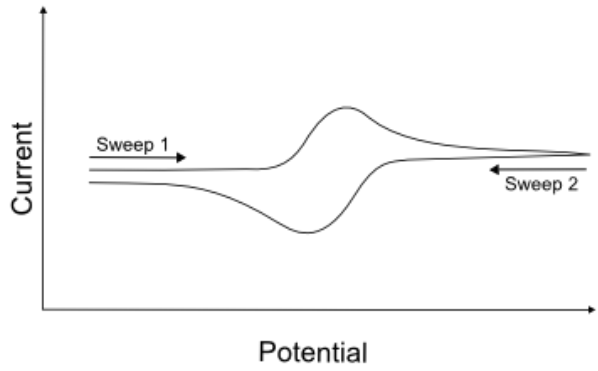

Figure 5 Classic example of a cyclic voltammetry presenting a perfectly reversible redox process were oxidation and reduction total charge (area of the peaks) are equal.

One instance of what can be observed during a CV is what follows: at t = 0 in proximity of the WE the reagent exists only in its oxidized state "O"; when the applied potential is near the standard potential value ($E^{\circ}_{O/R}$), the conversion between the O state and the reduced "R" state is observed as a current increase reading on the computer terminal from the cell, generated by the electron transfer happening from the WE and the reagent. As the potential scan continues past $E^{\circ}_{O/R}$ the current intensity grows as the reaction becomes faster until it reaches a maximus and then starts to diminish; this is not due to a sower reaction rate but to the thickening of the diffusion layer, the region of the solution in contact with the WE were the depletion of the reagent generates a gradient of concentration from the surface to the bulk (Figure 8).

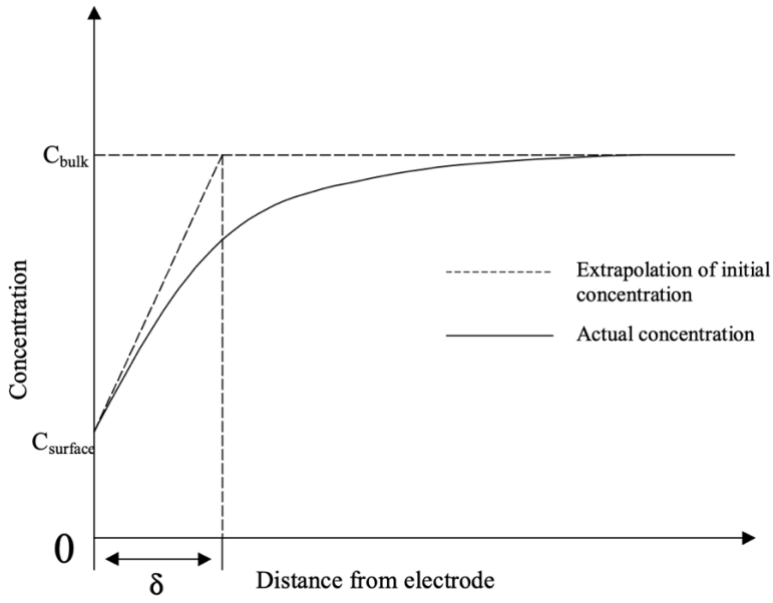

Figure 6 Representation of the gradient of reagent concentration in function of the distance from the electrode and how the diffusion layer is conventionally defined.

At the vertex potential set by the software the scan is inverted returning back to the $E^{\circ}_{O/R}$ were (if the reaction is reversible) the product R will be oxidized back to O producing an opposite current wave. The electrochemical convention assumes cathodic current positive and anodic current as negative. The study of faradic processes (redox reactions at the WE) can give parameters of the kinetics and thermodynamic extremely important. Thermodynamically is the half-wave potential ($E_{1/2}$) defined by the equation:

$$E_{\frac{1}{2}} = \frac{E_1 + E_2}{2}$$

Where E_1 and E_2 are peak potentials of one process and his reverse. This relationship is true if the diffusion coefficient (D) is similar for both the oxidized and reduced state. $E_{1/2}$ is directly proportional to $E^{\circ}_{O/R}$ giving the possibility to associate to every signal a specific redox event. From a kinetics standpoint, CVs can be used to find the electron transfer kinetic constant (k_0) and the symmetry factor (α). There is a deep connection and the peak current of a voltammogram according to the Butler-Volmer equation seen above. As k_0 quantify the rate of heterogenic electron transfer and is responsible of the reversibility or irreversibility of the process. If k_0 has a high value then the process is likely to be totally reversible, otherwise it will be ever less reversible the lower the k_0 value until reaching a situation of total irreversibility.

CA is another technique performable with the same electrochemical setup as for the CV. Two fixed Potential are applied at intervals for a number of repetitions at will (Figure 7). The output is a graph I vs t and it is a useful technique when the redox process in exam is strongly affected by diffusion.

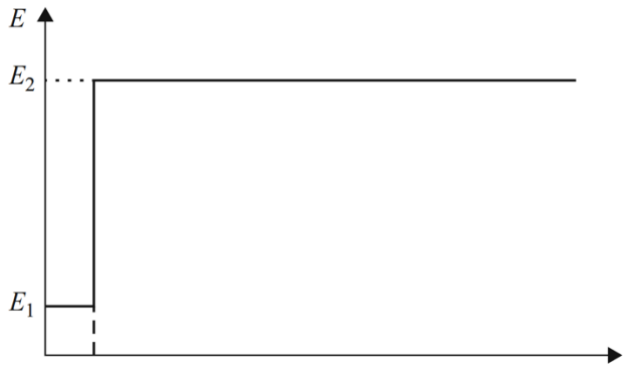

Figure 7 Representation of the "step-like" applied potential of a CA experiment.

If the solution is not being stirred, temperature is constant and cell size is in a greater scale compared to the diffusion layer then the Cottrell equation is valid and can be used:

$$i = \frac{nFAc^0\sqrt{D}}{\sqrt{\pi t}}$$

Where i is the current intensity, n is the number of electrons involved in the redox process, F is the Faraday constant, A is the electrode surface and c^0 is the bulk concentration of the analyte.

Scanning Electrochemical Microscopy

SECM is an imaging technology that needs a similar but more complex setup compared to the previous two techniques: comprising of what are, in fact, two WE (substrate and probe) for a total of four electrodes and the machine controlling the experiment parameters in this case is a *bi*-potentiostat. The probe is a micron wide platinum disk (or less) positioned over the substrate which is the sample to image. The disk scans the surface at a height of few micron thanks to a three motors apparatus (one for each translational degree of freedom) capable of precision positioning (each motor is a combination of an electrical step motor

and a piezo for fine movements). The resulting image gives not only topographic information, but SECM is often used to probe differences in surface reactivity.

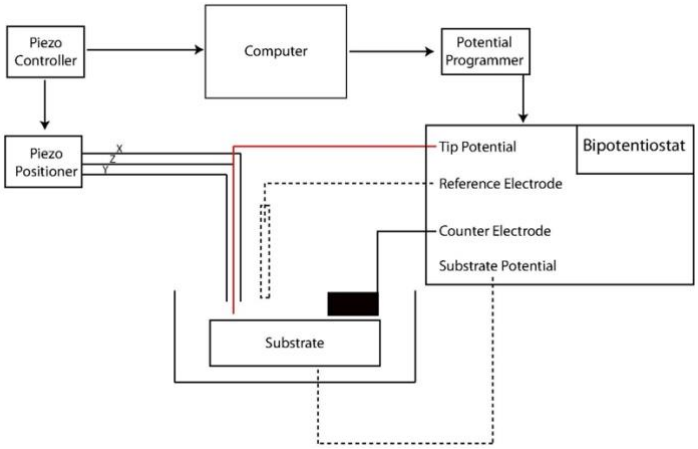

Scheme 6 Components scheme of a SECM setup.

A bi-potenziostat is made necessary as both probe and substrate are, in fact, two independent work electrodes and some experiments require them to have totally different polarizations. During an SECM experiment both substrate and probe are immersed in an electrolytic solution composed of electrolyte and an electroactive species. When the probe is positioned above the substrate at few microns, current readings from it starts to get influenced by two phenomena: (i) the tips surface blocks the migration of the electroactive molecules lowering its local concentration and thus the signal in what is called “negative feedback”, (ii) the good electrical conductivity of the substrate helps regenerate the electroactive species and actually increases the signal in what is called “positive feedback” (Figure 8).

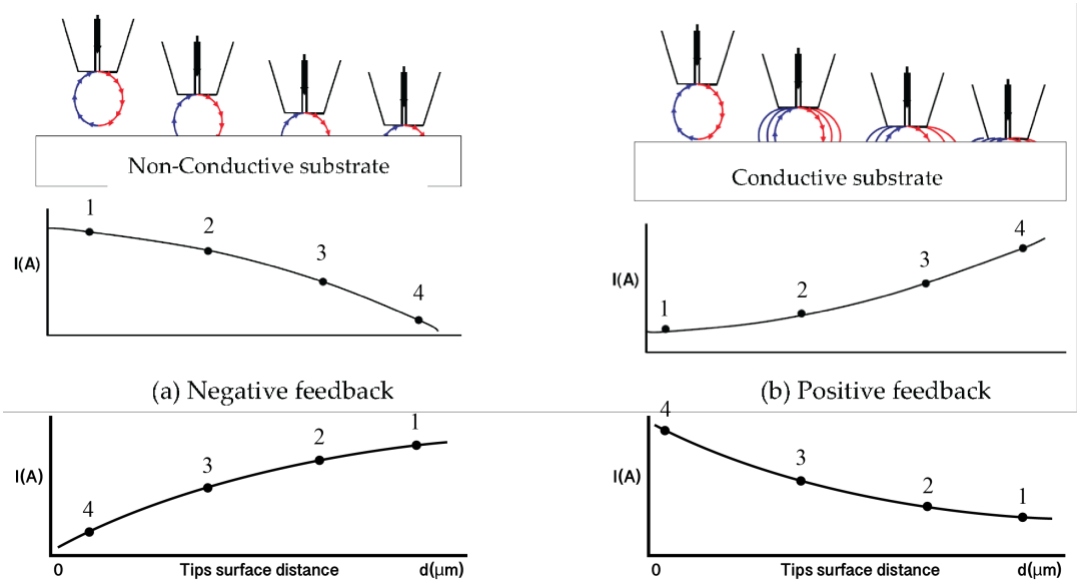

Figure 8 Effects of the conductivity of the substrate over the probe signal strength. A non-conductive substrate lowers the probe signal by affecting the diffusion at the tip (a), the nearer the tip to the surface the more pronounced is the effect. A conductive substrate interacts with the redox product generated at the tip acting as electron sink of reservoir, facilitating the regeneration and increasing the signal while approaching (b).

These two effects generate a "contrast" between regions of different conductivity from which an image can be processed.

Modelling of the two phenomena have been done in a semi-empiric way having as parameters the ratio between electrode disk probe radius and total radius (conductive disk plus isolating layer, R_g) and the ratio between distance probe-substrate and probe radius (L).

Negative feedback:

$$I_{T-}^{disk}(R_g, L) \approx \left[\frac{\frac{2.08}{R_g^{0.358}}\left(L - \frac{0.145}{R_g}\right) + 1.585}{\frac{2.08}{R_g^{0.358}}(L + 0.0023R_g) + 1.57 + \frac{lnR_g}{L} + \frac{2}{\pi R_g} ln\left(1 + \frac{\pi R_g}{2L}\right)} \right]$$

Positive feedback:

$$I_{T+}^{disk}(R_g, L) \approx \alpha(R_g) + \frac{1}{\beta(R_g)} \frac{\pi}{4arctanL} + \left[1 - \alpha(R_g) - \frac{1}{2\beta(R_g)}\right] \frac{2}{\pi} arctanL$$

By steadily lowering the probe on the substrate while recording the current signal you can study the profile of the curve "i vs L" that you so obtain (that is called an "approach curve") and calculate the charge transfer kinetic constant k^0 of a redox reaction taking place at the substrate. The current profile is proportional to analyte concentration and, in a

way this technique "image" the diffusion layer. Electron transfer kinetics can be determined by fitting approach curves to theory via a plot of the normalized tip current (I_T) versus L. The normalized tip current is related to the steady-state current (i_0) at effective infinite distancefrom a substrate ($I_T = i_T/i_0$).

$$k = \frac{k^0 exp[-\alpha f(E - E^0)]}{m_0}$$

Where f is:

$$n\frac{F}{RT}$$

And m_0 is:

$$m_0 = \frac{I_T(L)}{\pi a^2 nFC_0}$$

Where α is the symmetry factor, k^0 is the standard rate constant parameter and C_0 is the bulk concentration of the analyte.

Redox Competition Mode (RCM) and Generation/Collection Mode (G/C)

RCM is a category of experiments executed with an SECM setup where the same redox process is recorded both at the tip and the substrate with the probe inside the diffusion layer generated by the substrate. Reacting with the electroactive species, the substrate locally affects its concentration and by competing for the same reaction, the tip current reflects the difference in the consumption rate between the ultra-micro-electrode and substrate surface and hence provides information about the electrochemical activity of the surface. This method is used when the reagent concentration can be electrochemically measured but not that of the product. Sample reaction efficiency determines the diffusion layer; higher reaction rates lead to bigger depletion zone and vice versa.

When the reaction at the substrate generates electroactive products or intermediates it is possible to analyze their nature with the G/C mode, where the probe and substrate can respectively serve as either a generator or collector of redox active species. In this way, the tip current always reflects a close correlation with the sample's activity (Figure 9).

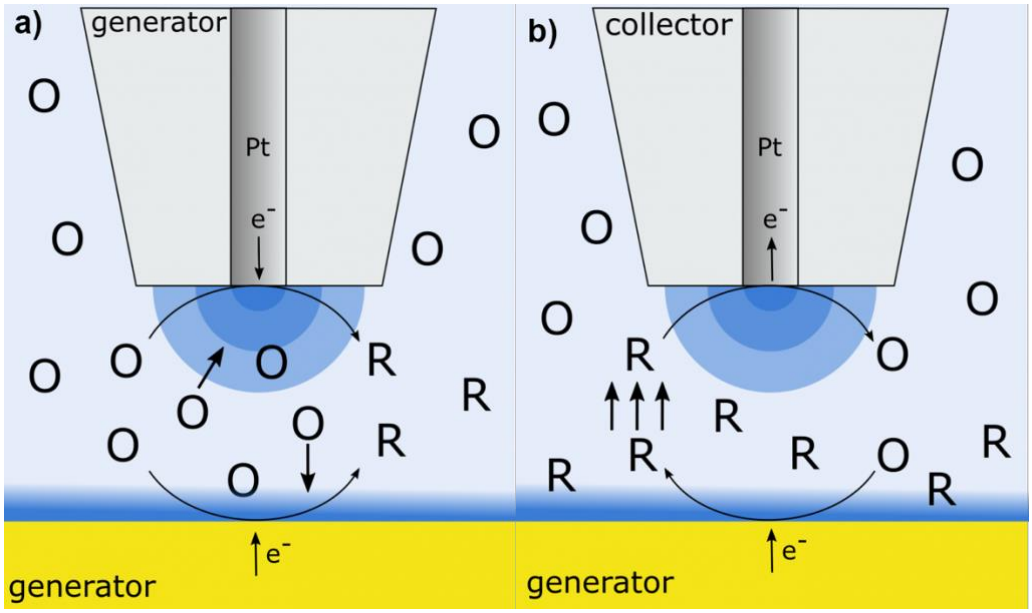

Figure 9 Graphical representation of the two modes. Here for instance is shown (a) an RCM where the electrodes compete on the reduction of the analyte and (b) G/C where the substrate is producing a reduced species collected by the ultramicro-electrode.

X-ray Photoelectron Spectroscopy

X-ray Photoelectron Spectroscopy (XPS) consists in a technique for the analysis of the atomic makeup of the surface level of a solid sample and the chemical bonding those atoms have with each other. An appropriate device irradiates the sample with monochromatic X-rays stimulating Auger electrons emission. The residual kinetic energy of the electrons in then measured and used to understand the atom and bond type is coming from. At the sensor, the electron has the kinetic energy of the impacting X photon minus the energy necessary to rise to vacuum energy from the bond level it comes from. Only surface level atoms can be probed with this technique as the lower atoms emit electrons which lose an unpredictable amount of energy as they make their way out of the sample and so losing the valuable information too.

The source is an X-ray tube consisting in a filament heated up by current to electron emission by *thermionic emission*. The emitted electrons are accelerated against a positively charged aluminum plate. The impact excites core electrons in the aluminum atom expelling them out and emitting X-rays as consequence of the vacancy being filled by the electron of the upper shell. The analyzer is usually a hemispherical deflection analyzer that splits the arriving electrons according to their energy.

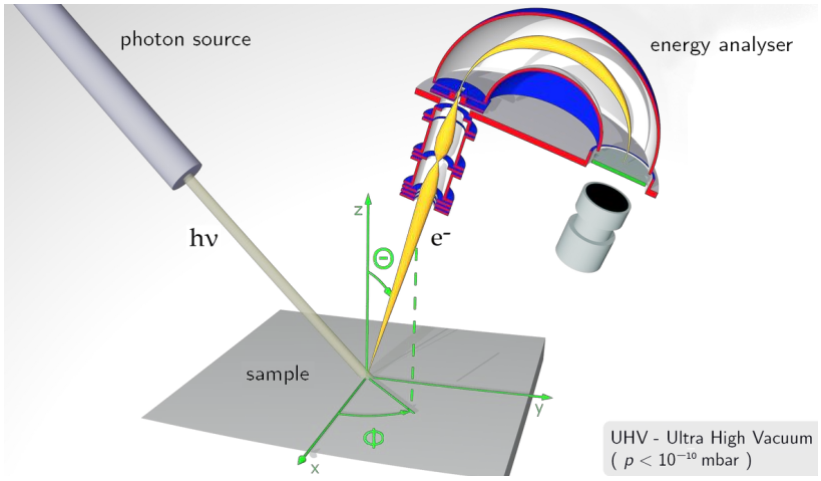

Scheme 7 Components scheme of an XPS setup.

Graphene Based Electrocatalytic Materials

During the PhD experimental activity, we worked on the synthesis and investigation of a variety of graphene-based materials, as sketched below in *Scheme 7*, with different levels of oxidation and type of doping to test them as working electrode materials (by a top-down method) in a saturated oxygen environment by using voltammetry and scanning probe microscopy techniques. In particular, the systems were obtained by doping the GO during their reduction process to lead to rGO and the aim of their investigation has been the understanding of general behavior of such nanostructured carbon materials, their catalytic performances and the effect of the doping for what concerns the oxygen reduction reaction.

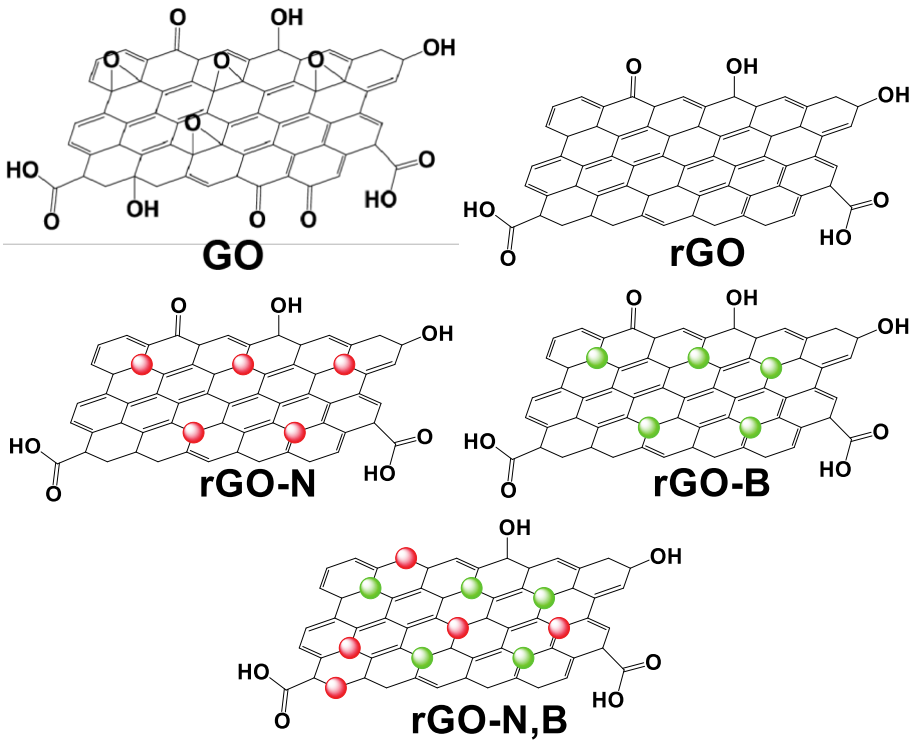

Scheme 8 Molecular structures of the graphenic systems here studied. In red and green are represented the doping nitrogen and boron atoms.

Experimental Section

Materials and General Experiments.

The reduced graphene oxide systems doped with either nitrogen, boron or boron-nitrogen have been synthesized in the lab of Dr. Giambastiani (CNR – Firenze) following a slightly modified literature procedure.[65,66] In brief, 40 mg of GO prepared with a modified

Hummers' method,[67] were suspended in 40 mL of distilled water and sonicated for 30 minutes. After that, $N_2H_4 \cdot H_2O$ (0.015 mL) was added dropwise and the suspension stirred at 80 °C for 20 hours. After cooling to room temperature, the mixture was filtered through a PTFE membrane filter (0.2 μm), the solid recovered, suspended in distilled water and purified by dialysis. Finally, the suspension was filtered again and dried to constant weight.

X-ray Photoelectron Spectroscopy (XPS) measurements were conducted on an (UHV) Thermo-VG scientific spectrometer, operating in ultrahigh vacuum and equipped with a CLAM4 (MCD) hemispherical electron analyzer and compared to the results of an elemental CHNS analysis performed with a Thermo FlashEA 1112 Series CHNS-O elemental analyzer. The Al Kα line (1486.6 eV) of a dual anode X-ray source was used as incident radiation. Samples were kept in ultra-high vacuum for 24 h to remove any traces of water or solvent before measurements. Charge correction of the spectra was performed by taking the sp_2 graphitic component of the C 1s spectrum as internal reference (Binding Energy, BE = 284.6 eV). Survey and high-resolution spectra were recorded in constant pass energy mode (100 and 20 eV, respectively). High resolution spectra of detected elements were acquired for semi-quantitative and detailed BE chemical shift analysis. The high-resolution spectra were fitted with mixed Gaussian–Lorentzian peaks after a Shirley background subtraction.

Electrochemical investigations by cyclic voltammetry (CV) were carried out using a BioLogic SP-300 potentiostat using a custom-made electrochemical cell described elsewhere.[68] Scanning Electrochemical Microscopy (SECM) was performed with a CH Instrument 910B made of a three-step motor system with a resolution of 1 μm in each direction and a Jena piezo system; the XYZ-moving system is coupled to a CHI bipotentiostat unit. The probe was a platinum disk ultramicroelectrode (UME) with 10 μm as diameter , and each probe was polished with a 0.3 μm and 0.05 μm aluminum oxide (Buehler) slurry in distilled water on a felt pad.

The samples were suspended with concentration 1 g/L in a mixture of Ethanol (EtOH, 99.5%, Sigma-Aldrich) and Dimethylformamide (DMF, 99.9%, Uvasol) with a ratio 3:1, by ultrasonicating for 20 minutes and leaving afterward under stirring to prevent that the material aggregates back to macroscopic grains. The suspension was then drop casted onto a disk working electrode for characterization. As stationary working electrode (WE) surface, Glassy Carbon (GC) disks 3 mm in diameter, square crystal HOPG 1.2x1.2 cm^2

were used, as well as Pt/GC Rotating Ring-Disk Electrode (RRDE) was utilized in the experiments. A Pt spiral wire acted as counter electrode (CE); either a saturated calomel electrode (SCE) or an Ag/AgCl (KCl, 3M) as absolute Reference Electrode (RE) were utilized, depending on the experiment type. Both the working and the counter electrodes were polished with aluminum oxide slurry 0,3 μm. Platinum on Carbon (Pt/C) 5% in Pt (Sigma-Aldrich) was chosen for comparison purposes to test the performance of the materials herein studied. The graphene-based materials thus deposited onto the electrode surface were analyzed in an aqueous solution at pH=13 by sodium hydroxide (NaOH, 99.7%, Sigma-Aldrich).

For every material the resulting homogeneous black suspension (ink), occasionally containing some relatively larger grains, barely visible at naked eye. Multiple aliquots of 5 μl each were drop casted on the working electrode disk to a total of 40 μl.

Results and Discussion

XPS Analysis

XPS analysis was performed on the initial graphite used as source of graphene sheets, on the GO obtained from the graphite via modified Hummers' method and on the various reduced variants of rGO. This was done in parallel with a chemical CHNS elemental analysis for comparison. From XPS data it can be appreciated the increment in oxygen content after oxidation with respect to graphite and its subsequent diminution in favor of the nitrogen and boron content confirming both the successful reduction of the GO and the introduction of the doping heteroatoms.

Table 2 Composition percentages obtained from chemical elemental analysis and XPS techniques.

	Elemental Analysis		**XPS**			
	C	**N**	**C**	**N**	**B**	**O**
Graphite	98.0	0.0	97.8	0.0	0.0	2.2
GO	48.0	0.0	69.1	0.0	0.0	30.4

rGO	83.5	0.0	87.6	0.0	0.0	12.4
rGO-N	77.6	1.9	84.1	1.8	0.0	12.9
rGO-B	72.9	0.0	73.9	0.0	1.3	24.8
rGO-B,N	72.6	2.1	85.9	2.5	0.6	11.0

Catalytic Activities.

The electrochemical activity of the various materials and their catalytic efficiency were investigated by cyclic voltammetry (CV) at room temperature both in O_2 saturated solution (at a pressure of 1 bar) to test the catalytic effects, and comparing them with the results obtained for the corresponding experiments performed in Ar saturated environment, for a reagent-free control experiment. Also, all the electrochemical and microscopy characterizations were carried out in alkaline solution in order to reproduce alkaline fuel cells conditions and to avoid proton coupled electron transfer (PCET), which would dramatically slow down the reaction kinetic.[69]

A selection of cyclic voltammetry results for the reduced graphene oxide (rGO), N-doped reduced graphene oxide (rGO-N), B-doped reduced graphene oxide (rGO-B), Boron and Nitrogen doped graphene oxide (rGO-B,N) is shown in Figure 10. Despite capacitive current is high, the faradaic current in presence of O_2 stands out both in terms of onset potential and current densities.

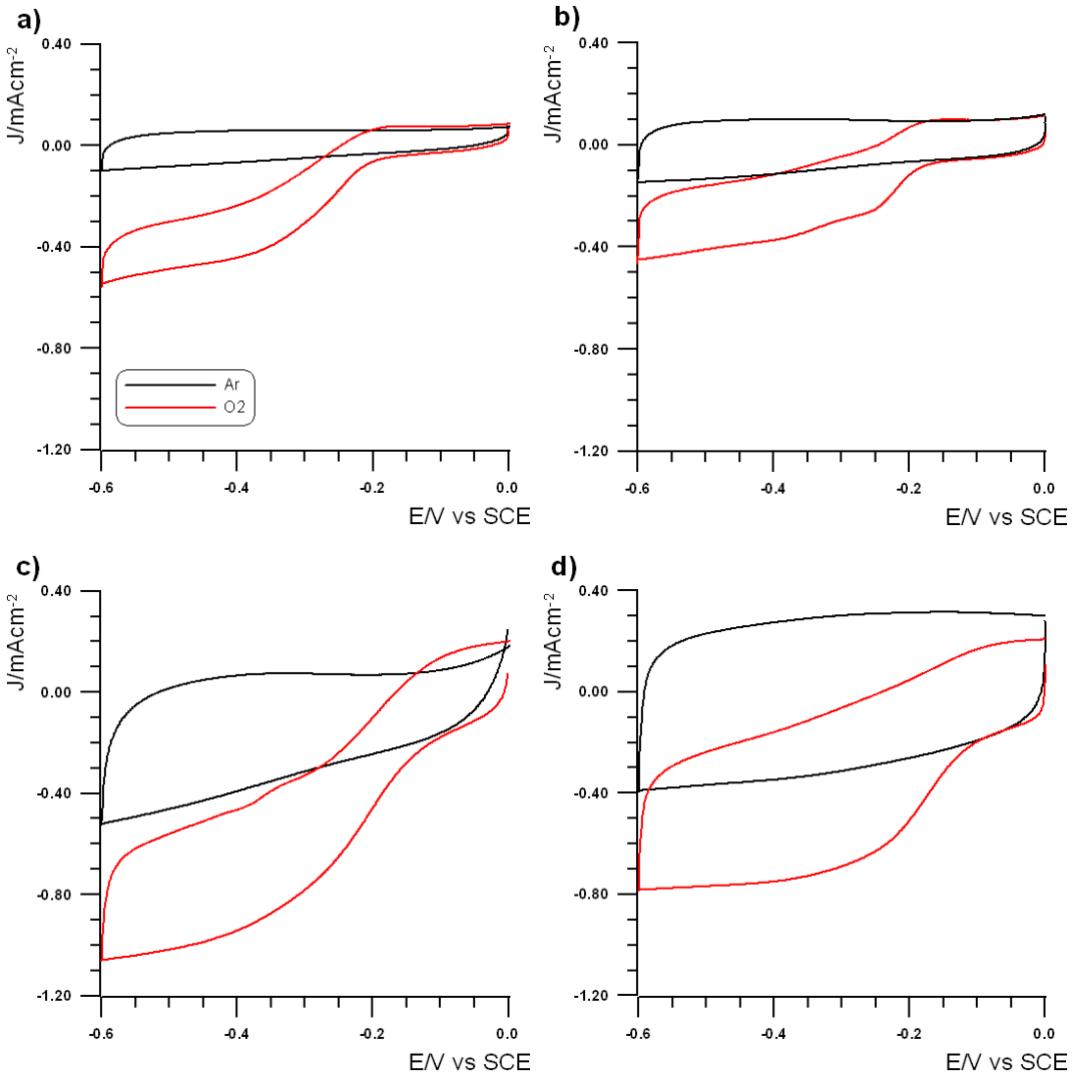

Figure 10 Cyclic voltammetric curves of a) rGO, b) rGO-N, c) rGO-B and d) rGO-B,N materials drop casted onto glassy carbon in KOH 0.1M solution (pH=13), in presence of Argon (grey) and O_2 atmosphere (red); 40 µl of 1 mg/ml EtOH/DMF dispersion drop casted onto 3 mm (0,07 cm^2) GC electrode; scan rate: 5 mV/s; T = 298K

The voltammetric results obtained for all the materials based on reduced graphene-oxide have also been compared with the behavior of other systems both nanostructured carbon materials and amorphous commercial ones (see Figure 11). In particular, a previously characterized carbon nanotubes, functionalized with acridine moieties (CNT@acrid), which gave interesting unprecedented results,[43] as well as a carbon supported platinum (PtC; 5% Pt on amorphous carbon) as an example of catalyst that is currently used in fuel cells.[70] The potential at which the material begins to manifest its own activity, i.e. the onset potential, is a first indicator of its catalytic capabilities. Voltammetric curves recorded in presence of O_2, with a scan rate of 0.005 V/s shown in Figure 11, were used as preliminary criterium to discriminate the catalytic activity of the various materials. It is worth to note

that even at a first glimpse the Boron containing samples shows a higher performance in terms of onset potential.

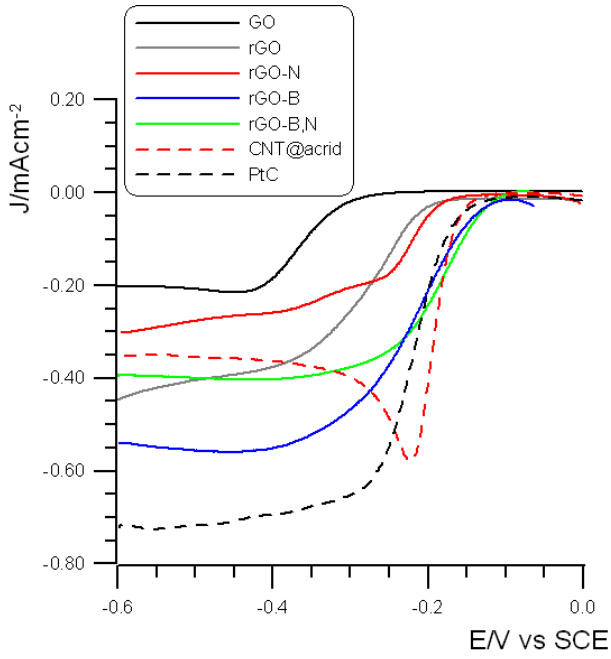

Figure 11 Comparison between linear sweep faradic current-potential curves for the various doped rGO materials, functionalized CNT[43] and Pt/C recorded at 293 K for ORR of O_2 saturated NaOH 0.1 M solution (O_2 pressure= 1 bar). Faradic only curves were obtained by subtracting an equivalent measure done in Ar saturated solution. GC disk (0.07 cm^2) was used as electrode substrate for all the materials. Scan rate: 5 mV/s. T = 298K

To gain further insights on the ORR electrochemical performance along the H_2O_2 production, RRDE voltammograms have been acquired. The results shown in Figure 12 unambiguously represent a clear evidence about the effects of the type of doping atoms on the general catalytic efficiency. Moreover, the comparison of the electrochemical data between the various doped materials indicates that boron is a better doping agent than nitrogen while the best performance is obtained from a mix of the two dopants in agreement with the findings reported in literature for similar works.[59] From the knowledge of the collection efficiency of the ring, which is 24% in our conditions, it is possible to calculate the values for the total production of H_2O_2.

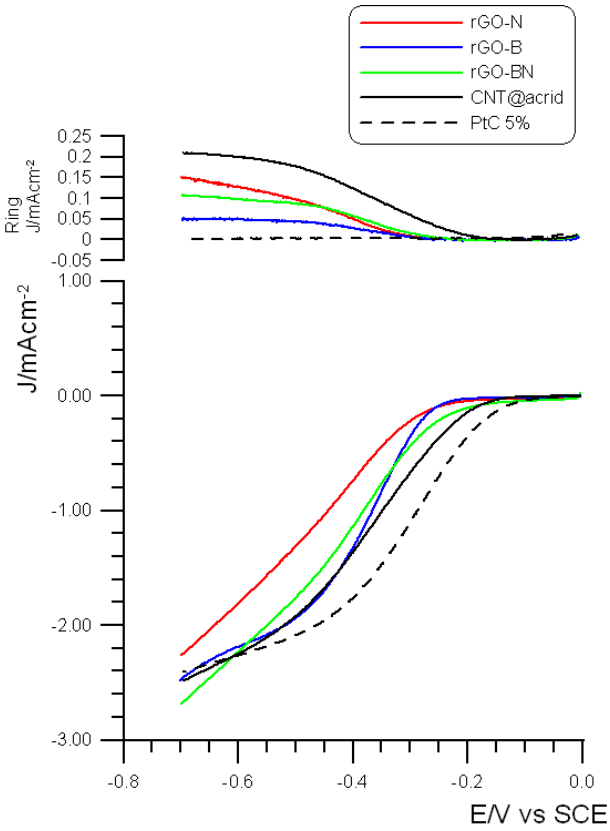

Figure 12 Comparison between linear sweep voltammetries of the doped materials and two reference models: the best performing material from the previous work from Giambastiani et al (CNT@acrid)[43] and an analog to the catalyst actually used in current consumer products (PtC). In the upper graph is shown the oxidation current of the H_2O_2. Measurements carried out in O_2 saturated NaOH 0.1 M solution for the GC disk (0.20 cm^2) Pt ring (0.07 cm^2) RRDE at 1600 rpm. Scan rate 5 mV/s, T = 298 K.

Table 3 Percentages of hydrogen peroxide production in relation with the total molar amount of product from ORR and onset potentials.

Material	H_2O_2 production	η (V) vs SCE
rGO-N	42%	-0.17
rGO-B	14%	-0.14
rGO-B,N	27%	-0.07
CNT@acrid	50%	-0,09
PtC	0%	-0.04

Chemical Annealing

In order to check whether the doped rGO systems are chemically stable at the various potentials explored, the materials were undergone multiple potential cycles at increasing negative and positive potentials in the same electrolyte and under argon. In particular, if the materials undergo a multiple voltammetric scans, with a switching potential in reduction at -1.0 V and in oxidation at +1.0, in an Ar atmosphere, a drastic change in current intensity was observed upon successive cycles, thus suggesting a chemical change occurring on the active surface of the material. As shown in Figure 14, the effect of such an "*electrochemical annealing*" is evidenced both in reduction and oxidation; it is permanent and it was found to have an important and reproducible effect on the ORR activity. We hypothesize that the irreversible electrochemical processes in reduction and oxidation (in both cases the electron transfers are followed up by chemically irreversible reactions) can be attributed to a partially uncomplete reduction of the materials upon chemical synthesis and hence to the possible presence of variously oxidized carbon sites (i.e., epossidic, carbonylic and carboxylic), that can be further reduced or oxidized and eventually restore the graphene structure.

As matter of fact, the comparison of the *electrochemically annealed* GO, in Figure 13, shows that the reduction process has a much larger effect on the onset potential of the ORR reaction of the material than the oxidation, for which the system becomes apparently more resistive than the GO itself.

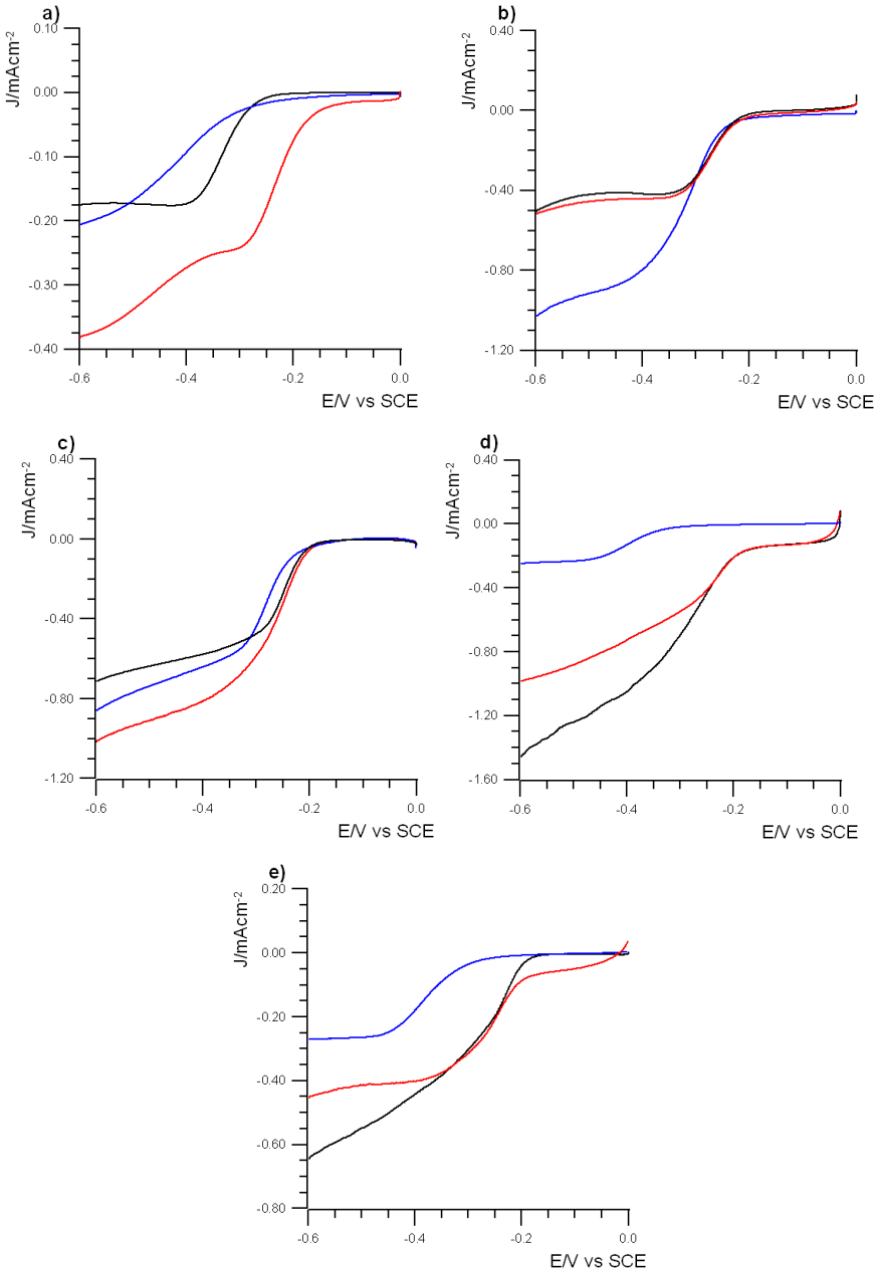

Figure 13 Linear sweep voltammetries showing the behavior of a) GO b) rGO c) rGO-N d) rGO-B e) rGO-B,N pristine (black), after reductive annealing (red) and oxidative annealing (blue) in atmosphere saturated with O_2. Deposit on GC disk (diameter 3 mm) in solution of KOH 0.1 M, Scan rate 0,005 V/s, Reference electrode: SCE.

Tafel Analysis

A further insight on the catalytic activity is given by plotting the data in a Tafel diagram. In Figure 14 it is possible to recognize a different behavior for the group of reference models (Pt/C and CNT@acrid) and the Boron doped rGO with a slope lower than the remaining two doped rGO, namely the rGO-N and rGO-BN, that have a slope of the straight line nearly double of the formers.

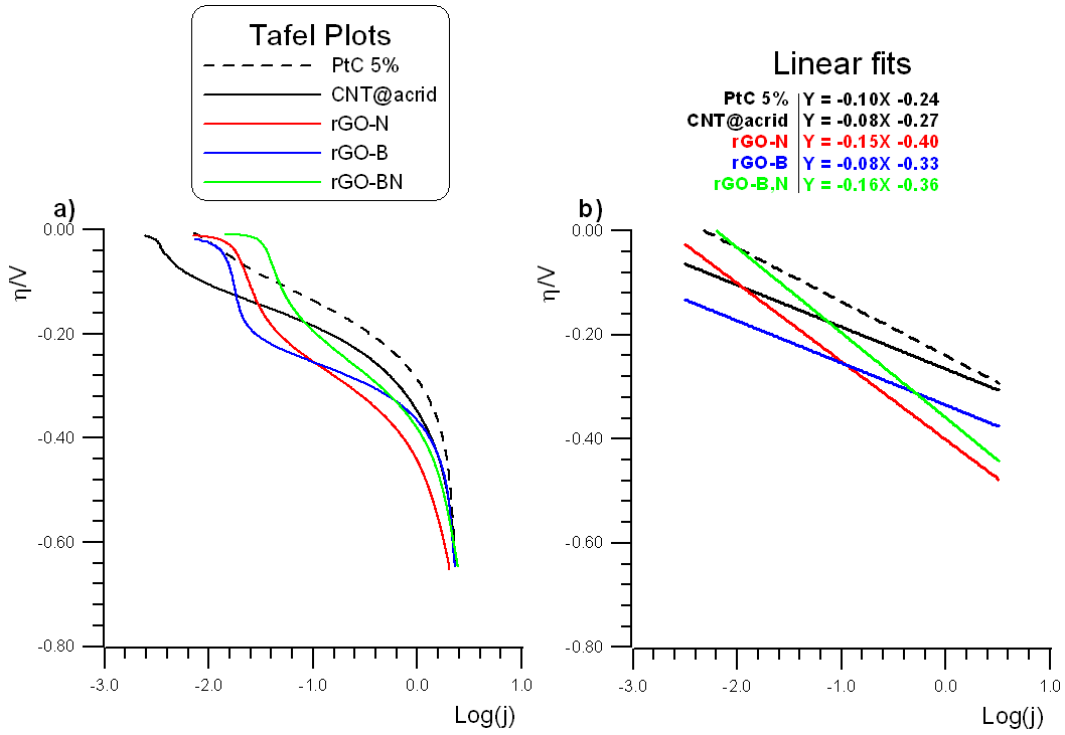

Figure 14 Tafel plots for the 1600 rpm RRDE measurements shown above (a). The linear sections of the curves were used for the fits (b).

Gravimetric Catalytic Efficiency

In order to have a more quantitative characterization of the material activity per mass further experiments were undertaken with different electrode material loading. Even though the ink films deposited so far should be 40 µg of material, it is naïve to assume every molecule present on the WE is active and in contact with the reagent. Deposits should have some degree of porosity and permeability, as graphene typically display,[71,72] nevertheless surface active sites are expected to contribute to the majority of ORR while some "dead volume" of material not electrochemically active should remain unused, underplaying the ORR current per gram. By running measurements with films made by drop casting ever increasing amounts of graphene it should be possible to monitor the variation of ORR activity as depending from the catalyst mass. For this purpose, a GC electrode was used as a stationary surface with various films of rGO-N and rGO-B drop casted over. A 2 mm GC electrode used was chosen for its Teflon casing around the conductive disk that kept the ink droplet well confined from spreading outside. This because the solvents used for the suspensions have extremely low affinity to the plastic and no material is lost outside the area of the active surface. Five deposits of 3, 9, 15, 30 and 36 µg of rGO-N and four deposits of 3, 9, 15 and 30 µg of rGO-B done by drop casting 3 µL

droplets were prepared and tested in Ar and O_2 saturated pH 13 solutions. Faradic current values taken from CVs at E = -0.3 V vs SCE, which is a point were for bare GC displays zero activity while graphene have a notable amount, were plotted I vs µg (Figure 15).

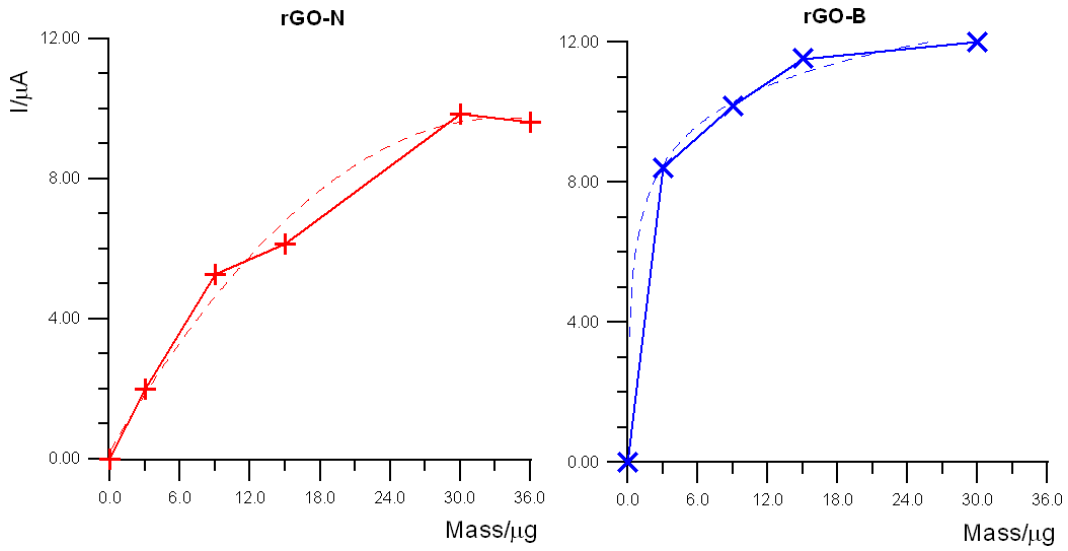

Figure 15 ORR in function of catalyst mass. Data taken from CVs at E = -0.3 V on the first potential ramp segment. Point at Mass = 0 g is from bare GC. O_2 saturated NaOH 0.1 M solution, same solution used Ar saturated to eliminate capacitive contribution. GC disk (3.14 mm^2) as electrode substrate. Scan rate: 5 mV/s, T = 298 K.

It is clear that ORR rapidly plateaus increasing deposit mass suggesting a rapid increase in dead volume. To obtain the real maximized activity/mass ratio a more precise experiment should be devised with ideally no dead volume in the deposit. That couldn't be done in the setting of this work but a preliminary lower-end estimation can be extrapolated with the data shown above. Assuming the 3 micrograms samples to have the highest active volume/dead volume ratio gravimetric catalytic efficiency for rGO-N should be equal or higher than 0.664 A/g and for rGO-B equal of higher than 2.80 A/g.

These findings suggest rGO-B has a greater intrinsic catalytic efficiency than expected. The material seems to be less porous, reaching quickly a current plateau by increasing the mass drop casted on the 3.14 mm^2 electrode surface. On the other hand, rGO-N, seems to be intrinsically less than a fourth as active by mass compared to rGO-B, but the more "laid-back" profile of the intensity vs mass plot suggest less dead volume is created by thickening the 3.14 mm^2 drop cast.

SECM "substrate generation/tip collection" (SG/TC) mode

Finally, to further investigate the reaction modalities of the material rGO-N the *substrate generation/tip collection* (SG/TC) mode was carried out by a scanning electrochemical microscopy (SECM) instrument using a 10 µm Pt tip as probe (Figure 16). HOPG was used as conducting surface on which the sample material was drop casted as described in the experimental section. The rGO-N@HOPG was used as substrate. The production of H_2O_2 due to the $2e^-$ ORR it is expected to be detected as a strong signal due to its re-oxidation in the range of potential between +0.1 V and +0.7 V.[73] Scanning various reductive potentials at the substrate, it is easy to detect the peroxide product at the UME giving an estimation of how much peroxide is produced and at which potential. The tip was set at a distance of 40 µm, by slowly approaching the surface and then stepping back of 40 µm before every measurement.

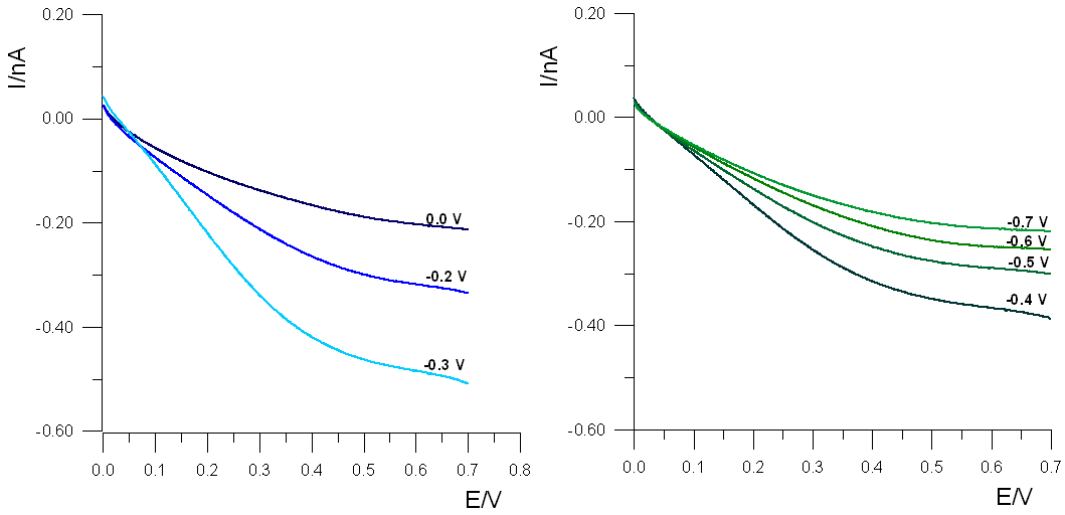

Figure 16 The two graphs highlight the increase in the tip current at low potentials (left) and the subsequent decrease at higher potentials (right). Probe tip: platinum disk (diameter: 10 µm). Substrate rGO-N@HOPG. Scan rate 0,05 V/s in solution of KOH 0,1 M in open air. Reference electrode: Ag/AgCl.

Performing the measurements with substrate potentials of 0, -0.2, -0.3, -0.4, -0.5, -0.6 and -0.7 V H_2O_2 signal was detected at the tip thus allowing to estimate the $2e^-$ process occurring at the substrate at low potentials. It is interesting to highlight that at higher potentials most likely a $4e^-$ process switch occurs as the current intensity rises when the potential changes from 0.0 V to -0.3 V and drops back from -0.4 V to -0.7 V (Figure 17). With the aim of investigating the effect of reductive annealing, the sample was then subjected to 20 cycles of voltammetry from 0.0 V to -1.0 V before repeating the

measurements. After the annealing the sample express the same behavior with the already noticed minor increase in activity.

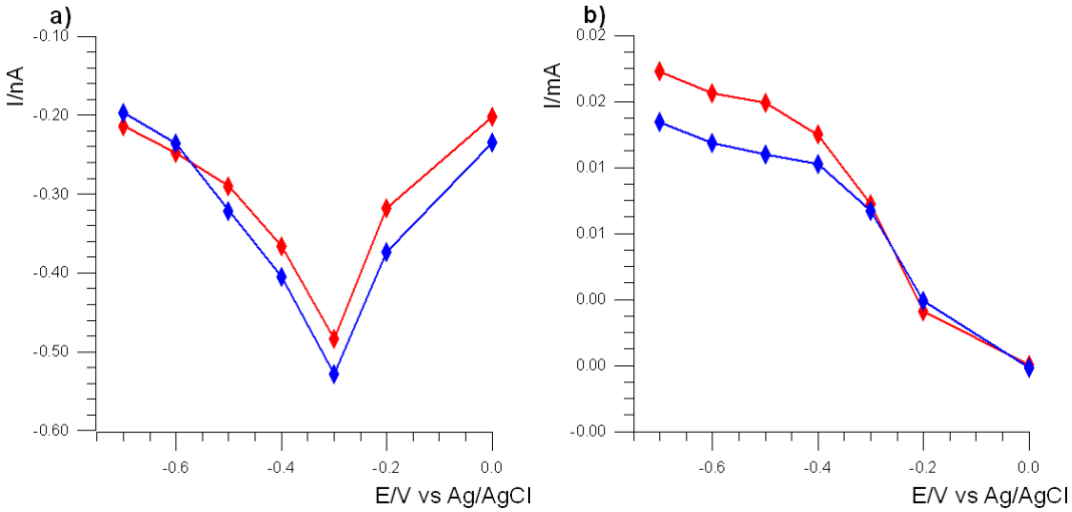

Figure 17 Comparison of the intensities of current at the tip (a) and at the substrate (b). Tips current values have been taken from CVs using as sample point the current of the forward segment at +0.6 V.

SECM "Redox competition" mode (RCM)

It is possible to calculate the dimensionless electron-transfer constant K_{et} of rGO-N with an RCM mode experiments. A 25 µm UME probe was set at a distance of 300 µm from the sample surface and then lowered steadily to near contact obtaining, in fact, an approach curve. In this experiments negative potentials are applied both at the substrate and at the tip, in order to reduce Oxygen at both two working electrodes.[74] HOPG was used again as support and the sample of rGO-N was prepared with the same procedure as for the SG/TC. The fitting of the approach curves using the Cornut-Lefrou equation allows to get the electron transfer kinetic constant that has a value of 0.015 for unconditioned material and 0.031 after annealing by negatively cycling the potential (Figure 18). An effective doubling of the k_{et} suggest that the chemical modifications occurring during annealing have important influence over the ORR mechanism and understanding their nature and role might be useful to obtain a bigger overview of these processes; further study is then needed on this topic, especially on the collections of chemical bonds altered in the annealing process.

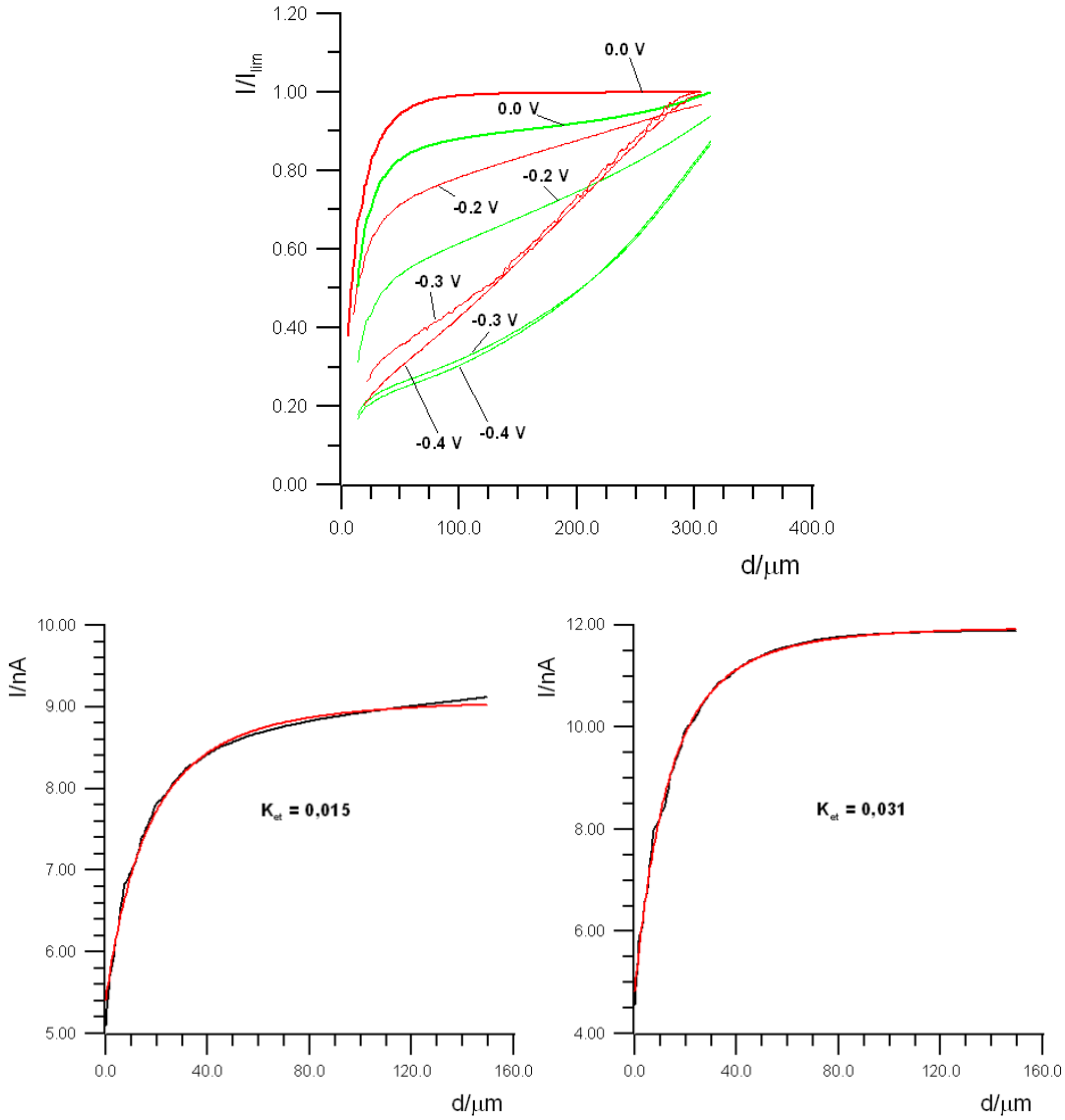

Figure 18 Approach curves on a non-annealed substrate (green) and a annealed one (red) with substrate potentials from 0.0 V (highest curve) to -0.4 V (lowest). And in the lower section is shown the fitting of the approach to the unpolarized substrate for non-annealed (left) and annealed (right).

Conclusions

In this work the electrocatalytic properties of graphene based nano-structured agents for the reduction of O_2 were studied as well as their efficiency in the 2 and 4 electron mechanism. The materials were divided by their doping heteroatoms: rGO-N, rGO-B and rGO-B,N. All the materials showed improved performances compared to the equivalent non-doped system with the lowest overpotential for ORR performed by rGO-B,N suggesting a collaborative effect between adjacent B-N pairs. The most efficient mechanism was performed by rGO-B with a production of H_2O_2 over H_2O as low as 14%. All the materials were studied by CV, showing remarkable catalytic properties with a reaction overvoltage of -0.07 V vs SCE.

Multiple CV cycles with a switching potential in reduction at -1.0 V and in oxidation at +1.0, in an Ar atmosphere, uncovered a drastic change in current intensity when the sample was tested back in presence of O_2, thus suggesting a chemical alteration occurring on the active surface of the material; a phenomenon here referred to as *chemical annealing*. It has been shown, through CV and SG/TC and RCM measurements, that the annealing carried out by subjecting the material to cycles of reduction, systematically brings positive effects on ORR both in terms of reaction current and overvoltage, while the annealing in oxidation leads to opposite results. Then has been demonstrated the reversibility of these processes with annealing in oxidation which resets the effects of a previous process in reduction, with no memory effect evident.

One system (rGO-N) was studied trough SECM in SG/TC and RC mode in a series of experiments aimed to analyze the products of reaction and the electron transfer kinetics of the material. Trough SG/TC a profile of peroxide production vs potential was obtained showing rGO-N peak production of H_2O_2 around -0.3 V. RCM was used to determine the electronic transfer constants and the effects of annealing on the relative values. It was found that reduction chemical annealing doubled the kinetic constant of electron transfer k_{et}.

Measurements of ORR activity performed with different loads of rGO-N and rGO-B drop casted on the GC electrode were set up to obtain a quantitative characterization of the material activity per mass unit.

The targeted materials were stable and efficient, and proved the synthesis technique that provided them to be promising as a way of producing alternative cathodic materials for

ORR. Further study is justified by these results and by the open possibility of using higher or lower doping or even other heteroatoms, possibly designing new systems able to outperform the ones here discussed.

References

1. Winter, M. & Brodd, R. J. What Are Batteries, Fuel Cells, and Supercapacitors? *Chem. Rev.* **104**, 4245–4270 (2004).
2. Sharaf, O. Z. & Orhan, M. F. An overview of fuel cell technology: Fundamentals and applications. *Renew. Sustain. Energy Rev.* **32**, 810–853 (2014).
3. Lee, J.-S. *et al.* Metal-Air Batteries with High Energy Density: Li-Air versus Zn-Air. *Adv. Energy Mater.* **1**, 34–50 (2011).
4. Chorkendorff, I. & Niemantsverdriet, J. W. *Concepts of Modern Catalysis and Kinetics*. (Wiley, 2003). doi:10.1002/3527602658.
5. Tripković, V., Skúlason, E., Siahrostami, S., Nørskov, J. K. & Rossmeisl, J. The oxygen reduction reaction mechanism on Pt(111) from density functional theory calculations. *Electrochim. Acta* **55**, 7975–7981 (2010).
6. Wroblowa, H. S., Yen-Chi-Pan & Razumney, G. Electroreduction of oxygen. *J. Electroanal. Chem. Interfacial Electrochem.* **69**, 195–201 (1976).
7. Meng, H., Zeng, D. & Xie, F. Recent Development of Pd-Based Electrocatalysts for Proton Exchange Membrane Fuel Cells. *Catalysts* **5**, 1221–1274 (2015).
8. Wang, X.-M., Wang, M.-E., Zhou, D.-D. & Xia, Y.-Y. Structural design and facile synthesis of a highly efficient catalyst for formic acid electrooxidation. *Phys. Chem. Chem. Phys.* **13**, 13594 (2011).
9. Wang, H., Maiyalagan, T. & Wang, X. Review on Recent Progress in Nitrogen-Doped Graphene: Synthesis, Characterization, and Its Potential Applications. *ACS Catal.* **2**, 781–794 (2012).
10. Novoselov, K. S. *et al.* Electric field in atomically thin carbon films. *Science (80-.).* **306**, 666–669 (2004).
11. Damjanovic, A., Genshaw, M. A. & Bockris, J. O. The Mechanism of Oxygen Reduction at Platinum in Alkaline Solutions with Special Reference to H[sub 2]O[sub 2]. *J. Electrochem. Soc.* **114**, 1107 (1967).
12. Damjanovic, A., Sepa, D. B. & Vojnovic, M. V. New evidence supports the proposed mechanism for O2 reduction at oxide free platinum electrodes. *Electrochim. Acta* **24**, 887–889 (1979).
13. Zheng, Y., Jiao, Y., Ge, L., Jaroniec, M. & Qiao, S. Z. Two-Step Boron and Nitrogen Doping in Graphene for Enhanced Synergistic Catalysis. *Angew. Chemie Int. Ed.* **52**, 3110–3116 (2013).
14. Choi, C. H., Chung, M. W., Kwon, H. C., Park, S. H. & Woo, S. I. B, N- and P, N-doped graphene as highly active catalysts for oxygen reduction reactions in acidic media. *J. Mater. Chem. A* **1**, 3694 (2013).
15. Xue, Y. *et al.* Three-dimensional B,N-doped graphene foam as a metal-free catalyst for oxygen reduction reaction. *Phys. Chem. Chem. Phys.* **15**, 12220 (2013).
16. Bonaccorso, F. *et al.* Production and processing of graphene and 2d crystals. *Mater. Today* **15**, 564–589 (2012).
17. Ferrari, A. C. *et al.* Science and technology roadmap for graphene, related two-dimensional crystals, and hybrid systems. *Nanoscale* **7**, 4598–4810 (2015).
18. Cooper, D. R. *et al.* Experimental review of graphene. (2011).
19. Charlier, J.-C., Eklund, P. C., Zhu, J. & Ferrari, A. C. Electron and Phonon Properties of Graphene: Their Relationship with Carbon Nanotubes. in 673–709 (2007).

doi:10.1007/978-3-540-72865-8_21.
20. Novoselov, K. S. *et al.* Two-dimensional gas of massless Dirac fermions in graphene. *Nature* **438**, 197–200 (2005).
21. Morozov, S. V. *et al.* Giant Intrinsic Carrier Mobilities in Graphene and Its Bilayer. *Phys. Rev. Lett.* **100**, 016602 (2008).
22. Chen, J.-H., Jang, C., Xiao, S., Ishigami, M. & Fuhrer, M. S. Intrinsic and extrinsic performance limits of graphene devices on SiO2. *Nat. Nanotechnol.* **3**, 206–209 (2008).
23. Balandin, A. A. *et al.* Superior Thermal Conductivity of Single-Layer Graphene. *Nano Lett.* **8**, 902–907 (2008).
24. Lee, C., Wei, X., Kysar, J. W. & Hone, J. Measurement of the Elastic Properties and Intrinsic Strength of Monolayer Graphene. *Science (80-.).* **321**, 385–388 (2008).
25. Denis, P. A. & Iribarne, F. Comparative Study of Defect Reactivity in Graphene. *J. Phys. Chem. C* **117**, 19048–19055 (2013).
26. Marcano, D. C. *et al.* Improved Synthesis of Graphene Oxide. *ACS Nano* **4**, 4806–4814 (2010).
27. Zhu, Y. *et al.* Graphene and Graphene Oxide: Synthesis, Properties, and Applications. *Adv. Mater.* **22**, 3906–3924 (2010).
28. McAllister, M. J. *et al.* Single Sheet Functionalized Graphene by Oxidation and Thermal Expansion of Graphite. *Chem. Mater.* **19**, 4396–4404 (2007).
29. Paredes, J. I., Villar-Rodil, S., Martínez-Alonso, A. & Tascón, J. M. D. Graphene Oxide Dispersions in Organic Solvents. *Langmuir* **24**, 10560–10564 (2008).
30. Hummers, W. S. & Offeman, R. E. Preparation of Graphitic Oxide. *J. Am. Chem. Soc.* **80**, 1339–1339 (1958).
31. Kosynkin, D. V. *et al.* Longitudinal unzipping of carbon nanotubes to form graphene nanoribbons. *Nature* **458**, 872–876 (2009).
32. Wu, Y. H., Yu, T. & Shen, Z. X. Two-dimensional carbon nanostructures: Fundamental properties, synthesis, characterization, and potential applications. *J. Appl. Phys.* **108**, 071301 (2010).
33. Li, X. *et al.* Large-Area Synthesis of High-Quality and Uniform Graphene Films on Copper Foils. *Science (80-.).* **324**, 1312–1314 (2009).
34. Bae, S. *et al.* Roll-to-roll production of 30-inch graphene films for transparent electrodes. *Nat. Nanotechnol.* **5**, 574–578 (2010).
35. Wang, Y., Chen, S. & Hu, A. Chemical Synthesis of Carbon Nanomaterials Through Bergman Cyclization. in 147–171 (2017). doi:10.1007/12_2017_5.
36. Gong, K., Du, F., Xia, Z., Durstock, M. & Dai, L. Nitrogen-Doped Carbon Nanotube Arrays with High Electrocatalytic Activity for Oxygen Reduction. *Science (80-.).* **323**, 760–764 (2009).
37. Liu, X. & Dai, L. Carbon-based metal-free catalysts. *Nat. Rev. Mater.* **1**, 16064 (2016).
38. Jiujun Zhang. *PEM Fuel Cell Electrocatalysts and Catalyst Layers*. (2008).
39. Wang, S. *et al.* BCN Graphene as Efficient Metal-Free Electrocatalyst for the Oxygen Reduction Reaction. *Angew. Chemie Int. Ed.* **51**, 4209–4212 (2012).
40. Dai, L., Xue, Y., Qu, L., Choi, H. J. & Baek, J. B. Metal-Free Catalysts for Oxygen Reduction Reaction. *Chem. Rev.* **115**, 4823–4892 (2015).
41. Yang, Z. *et al.* Sulfur-doped graphene as an efficient metal-free cathode catalyst for oxygen reduction. *ACS Nano* **6**, 205–211 (2012).
42. Sun, X. *et al.* Fluorine-Doped Carbon Blacks: Highly Efficient Metal-Free

Electrocatalysts for Oxygen Reduction Reaction. *ACS Catal.* **3**, 1726–1729 (2013).
43. Tuci, G. *et al.* Tailoring carbon nanotube N-dopants while designing metal-free electrocatalysts for the oxygen reduction reaction in alkaline medium. *ACS Catal.* **3**, 2108–2111 (2013).
44. Kumar, S., Gonen, S., Friedman, A., Elbaz, L. & Nessim, G. D. Doping and reduction of graphene oxide using chitosan-derived volatile N-heterocyclic compounds for metal-free oxygen reduction reaction. *Carbon N. Y.* **120**, 419–426 (2017).
45. Maldonado, S., Morin, S. & Stevenson, K. J. Structure, composition, and chemical reactivity of carbon nanotubes by selective nitrogen doping. *Carbon N. Y.* **44**, 1429–1437 (2006).
46. Liu, Y. & Wu, P. Graphene Quantum Dot Hybrids as Efficient Metal-Free Electrocatalyst for the Oxygen Reduction Reaction. *ACS Appl. Mater. Interfaces* **5**, 3362–3369 (2013).
47. Li, Y. *et al.* Nitrogen-Doped Graphene Quantum Dots with Oxygen-Rich Functional Groups. *J. Am. Chem. Soc.* **134**, 15–18 (2012).
48. Sharifi, T., Hu, G., Jia, X. & Wågberg, T. Formation of Active Sites for Oxygen Reduction Reactions by Transformation of Nitrogen Functionalities in Nitrogen-Doped Carbon Nanotubes. *ACS Nano* **6**, 8904–8912 (2012).
49. Wu, G. & Zelenay, P. Nanostructured Nonprecious Metal Catalysts for Oxygen Reduction Reaction. *Acc. Chem. Res.* **46**, 1878–1889 (2013).
50. Zhang, Z., Zhang, J., Chen, N. & Qu, L. Graphene quantum dots: an emerging material for energy-related applications and beyond. *Energy Environ. Sci.* **5**, 8869 (2012).
51. Jeon, I.-Y. *et al.* Large-Scale Production of Edge-Selectively Functionalized Graphene Nanoplatelets via Ball Milling and Their Use as Metal-Free Electrocatalysts for Oxygen Reduction Reaction. *J. Am. Chem. Soc.* **135**, 1386–1393 (2013).
52. Li, Q., Zhang, S., Dai, L. & Li, L. Nitrogen-Doped Colloidal Graphene Quantum Dots and Their Size-Dependent Electrocatalytic Activity for the Oxygen Reduction Reaction. *J. Am. Chem. Soc.* **134**, 18932–18935 (2012).
53. Jing, Y. & Zhou, Z. Computational Insights into Oxygen Reduction Reaction and Initial Li 2 O 2 Nucleation on Pristine and N-Doped Graphene in Li–O 2 Batteries. *ACS Catal.* **5**, 4309–4317 (2015).
54. Chizari, K. *et al.* Tuning of nitrogen-doped carbon nanotubes as catalyst support for liquid-phase reaction. *Appl. Catal. A Gen.* **380**, 72–80 (2010).
55. Terrones, M. *et al.* N-doping and coalescence of carbon nanotubes: synthesis and electronic properties. *Appl. Phys. A Mater. Sci. Process.* **74**, 355–361 (2002).
56. An, W. & Turner, C. H. Chemisorption of Transition-Metal Atoms on Boron- and Nitrogen-Doped Carbon Nanotubes: Energetics and Geometric and Electronic Structures. *J. Phys. Chem. C* **113**, 7069–7078 (2009).
57. Zhang, G., Duan, W. & Gu, B. Effect of substitutional atoms in the tip on field-emission properties of capped carbon nanotubes. *Appl. Phys. Lett.* **80**, 2589–2591 (2002).
58. Fazio, G., Ferrighi, L. & Di Valentin, C. Boron-doped graphene as active electrocatalyst for oxygen reduction reaction at a fuel-cell cathode. *J. Catal.* **318**, 203–210 (2014).
59. Favaro, M. *et al.* Single and Multiple Doping in Graphene Quantum Dots: Unraveling the Origin of Selectivity in the Oxygen Reduction Reaction. *ACS Catal.* **5**,

129–144 (2015).
60. Yang, L. *et al.* Boron-doped carbon nanotubes as metal-free electrocatalysts for the oxygen reduction reaction. *Angew. Chemie - Int. Ed.* **50**, 7132–7135 (2011).
61. Ferrighi, L., Datteo, M. & Di Valentin, C. Boosting Graphene Reactivity with Oxygen by Boron Doping: Density Functional Theory Modeling of the Reaction Path. *J. Phys. Chem. C* **118**, 223–230 (2014).
62. Shen, A. *et al.* Oxygen Reduction Reaction in a Droplet on Graphite: Direct Evidence that the Edge Is More Active than the Basal Plane. *Angew. Chemie Int. Ed.* **53**, 10804–10808 (2014).
63. Su, D. S. *et al.* Metal-Free Heterogeneous Catalysis for Sustainable Chemistry. *ChemSusChem* **3**, 169–180 (2010).
64. Lai, L. *et al.* Exploration of the active center structure of nitrogen-doped graphene-based catalysts for oxygen reduction reaction. *Energy Environ. Sci.* **5**, 7936 (2012).
65. Chua, C. K. & Pumera, M. The reduction of graphene oxide with hydrazine: elucidating its reductive capability based on a reaction-model approach. *Chem. Commun.* **52**, 72–75 (2016).
66. Park, S. *et al.* Chemical structures of hydrazine-treated graphene oxide and generation of aromatic nitrogen doping. *Nat. Commun.* **3**, 638 (2012).
67. Kim, F. *et al.* Self-Propagating Domino-like Reactions in Oxidized Graphite. *Adv. Funct. Mater.* **20**, 2867–2873 (2010).
68. Zamolo, V. A. *et al.* Highly Sensitive Electrochemiluminescent Nanobiosensor for the Detection of Palytoxin. *ACS Nano* **6**, 7989–7997 (2012).
69. Bard J. Allen, F. R. L. *ELECTROCHEMICAL METHODS*. (2001).
70. Yu, X. & Ye, S. Recent advances in activity and durability enhancement of Pt/C catalytic cathode in PEMFC. *J. Power Sources* **172**, 145–154 (2007).
71. Raidongia, K. & Huang, J. Nanofluidic Ion Transport through Reconstructed Layered Materials. *J. Am. Chem. Soc.* **134**, 16528–16531 (2012).
72. Nair, R. R., Wu, H. A., Jayaram, P. N., Grigorieva, I. V. & Geim, A. K. Unimpeded Permeation of Water Through Helium-Leak-Tight Graphene-Based Membranes. *Science (80-.).* **335**, 442–444 (2012).
73. Zhang, Y. *et al.* Nano-assemblies consisting of Pd/Pt nanodendrites and poly (diallyldimethylammonium chloride)-coated reduced graphene oxide on glassy carbon electrode for hydrogen peroxide sensors. *Mater. Sci. Eng. C* **58**, 1246–1254 (2016).
74. Eckhard, K., Chen, X., Turcu, F. & Schuhmann, W. Redox competition mode of scanning electrochemical microscopy (RC-SECM) for visualisation of local catalytic activity. *Phys. Chem. Chem. Phys.* **8**, 5359 (2006).

Chapter II

Electro-synthesis of Non-precious Metal Nanoparticles for Electrocatalysis of Hydrogen Evolution Reaction.

Hydrogen as Energy Vector

As it has been recognized that our fossil fuel-based society is on a non-sustainable track, a multitude of new technologies, required for the development of renewable and clean energy carriers, have been researched and developed as crucial key points for a smooth transition towards a complete sustainability. Technologies like new metal-air batteries, high-efficiency fuel cells, and more efficient production methods of energy carriers, especially hydrogen (H_2), as a substitute for traditional fossil fuels.[1] H_2 has always been on the highlights for its ubiquitous presence, clean reaction product and high gravimetric energy density. H_2 extracted from hydrocarbon, in a process called steam reforming, is already widely used to produce ammonia for fertilizes and other chemicals; is also used by oil refineries to react with heavy oils to produce transport fuels. Many are the examples were massive amounts of H_2 are used for chemical processes, consequently H_2 is not a newcomer in our industrial technology, but all the mass production done by conventional industry directly produce CO_2, this is why H_2 has never been regarded as a big contributor to the energy transition. Nonetheless that industry legacy of nearly a hundred years left us a know-how on how to handle what actually is a very explosive and corrosive element. Today H_2 is transported safely through pipelines and special road hauling and it has great potential both as direct fuel and energy vector for long term storage. Carbon fibers canisters can hold up to 700 atms of H_2 and even expended salt mines have been suggested as a storing solution for dealing with the extreme amounts that would be needed for power grid stabilization during winter, when solar and wind might not be sufficient. This grid stabilization potential is particularly important as solar and wind power generation is obviously subject to wide fluctuation during the day and seasonal cycles. H_2 stored during high power production times can be used as buffer to increase reliability of green energy solutions. Europe alone consumes 2200 TW/h every year for heat and refrigeration, at these scales buffering the grid during the year would require hundreds of trillions of dollars spent in batteries or a huge ecological impact using pumped water uphill in the numerous

artificial lakes needed, while H_2 underground storage would be orders of magnitudes less expensive and environmentally friendly. Another way H_2 can increase green energy reliability is by being produced where geographic contingencies make solar and wind energy abundant and stable and then efficiently distributed were power is needed, a philosophy known as “put the panels where is sunny”. At European latitudes summer solar irradiation can be from 2 to 5 times higher than during winter. Installing enough solar panels and wind farms to meet the winter requirements would lead to useless excess during summer. H_2 can link regions of the world far apart with transfer losses far lower compared to electrical wire transport. The Sahara Desert could provide energy for Europe and Australia is already planning to produce H_2 in the northern areas of the continent for then transport to Japan for consumption.[2] Already existing pipelines used for natural gas can be used by mixing it with 10% H_2 in weight without any upgrade to the infrastructure and up to 100% H_2 for more modern pipelines with minimal technical intervention.[3] It has also been proposed to be used combined with fuel cell technology and electric motors as energy source in big vehicles as trucks, trains, ships and even airplanes. The feasibility of using H_2 as energy vector on large scale prompt us to think on how to obtain industrial amounts without CO_2 emission. Water splitting by electricity generated from renewable sources has been proposed as mechanism to obtain carbon free H_2 since the early ’70, but this ties the production cost of H_2 to the green energy cost in the first place, production cost that was historically prohibitive.[4]

More recently, the ever-expanding renewable infrastructure around the world is generating a paradigm shift, with green energy becoming cheaper surprisingly fast.[5] H_2 from water splitting is becoming an economically competitive solution for lowering the carbon footprint of our society. Between 2010 and 2018, solar capacity cost has dropped of 75% and recent projections for the next 10 years esteem another 50% reduction in cost compared to 2020. As the green energy infrastructure becomes ever more prominent another chokehold of H_2 production becomes evident: water splitting requires highly purified water and expensive rare materials as catalyst.

Hydrogen Evolution Reaction (HER)

Hydrogen production by splitting water using sustainable electrocatalysts and powered by renewable energy from solar or wind is one of the promising alternatives to generate a carbon-free energy vector. As Fuel cells require an efficient electrocatalyst for the ORR,

electrolytic water splitting requires catalysts for the Oxygen Evolution Reaction (OER) at the anode and the HER at the cathode. Photocatalytic and electrocatalytic HER have been advocated as promising electricity driven strategies for H_2 generation.[6] Although precious metals (Pt, Pd, Rh, etc.) are highly efficient HER catalysts, their high cost and scarcity greatly hinder their practical/sustainable applications.[7] Hence, exploring alternative catalysts with good efficiency, resistance to corrosion, low cost and earth abundance is highly important for these technologies to become truly sustainable. Recently, transition metals with high intrinsic activities and their related compounds, including oxides, nitrides, phosphides, carbides and sulphides, have been widely investigated and demonstrated to provide potential catalysts for HER.[8,9] A nickel based anode has recently performed well in seawater resisting for thousands of hours to chloride corrosion[10] opening the possibility to operate without the need of fresh water.

Hydrogen evolution electrocatalytic mechanism has been extensively studied in the past decades and today it is known that proceeds via either a Volmer-Tafel or Volmer-Heyrovsky mechanism depending on the catalytic surface.[11,12] The Volmer step is the reduction of an adsorbed water molecule on the catalyst surface into a hydrogen atom and negatively charged hydroxide anion. Subsequently, the adsorbed hydrogen atom can either be combined with another adsorbed hydrogen atom (also formed by the Volmer step) to generate a hydrogen molecule that is than desorbed returning to the solution (the Tafel step), or meet another water molecule to produce a hydrogen molecule and a hydroxide anion (the Heyrovsky step).

$$H_2O + e^- \rightarrow H_{ads} + OH^- \text{ Volmer}$$

$$H_{ads} + H_{ads} \rightarrow H_2$$

$$H_{ads} + H_2O + e^- \rightarrow H_2 + OH^- \text{ Heyrovsky}$$

The Volmer step not only depends on the adsorption energy of the hydrogen atom but is also related to the adsorption energy of water and the desorption energy of the hydroxide anion. This complexity is the reason we cannot generalize the behavior into a classic "volcano plot" were the activity of the electrocatalyst is directly related to the affinity of the reactant with the surface. Low water adsorption energy can lead to insufficient reactants, while high hydroxide anion adsorption energy causes a poisoning effect owing to a loss of catalytically active site.[13]

Since metallic nickel was discovered to catalyze H_2 evolution more than a century ago,[14] the HER mechanism on metallic Ni has been widely studied as early as in the '60s. To

date, there is still no common consensus on the alkaline HER mechanism on Ni surfaces. The first studies suggested that the rate-determining step is likely the slow discharge of the H_2O molecule or the Volmer step.[15] A few follow-up studies have proposed the Volmer step as the rate-determining step and the more favorable Volmer-Tafel route for hydrogen evolution, but there have also been reports disputing these early proposals based on data obtained by modern techniques.[16,17] Meanwhile, another study concluded that within a specific potential region, the reaction mechanism follows the Volmer-Tafel route but undergoes the Volmer-Heyrovsky step above a certain potential value; and the rate is possibly controlled by the Heyrovsky step.[18]

To reach the efficiency of expensive high-performance noble metal-based materials with nickel, researchers have focused their efforts on electrode design. For electrocatalysis, the significantly higher surface area afforded by the nanostructures can dramatically improve the current density at the same overpotential. Ni nanostructures with high surface area can be synthesized using various methods, including bottom-up synthesis via the reduction of nickel salts as well as top-down template-based synthesis.[19–21] An interesting bottom-up technique is the "electrodeposition". By reducing the metal salts in the right environment and on the right cathode surface it is possible to generate metallic nanostructures directly on the component where are needed.[22–24] Such technique inspired the work done for this thesis, where a novel procedure was tested with a notable degree of success.

Introduction to the Electrosynthesis of Nanomaterials

Electrosynthesis of nanomaterials means to form a metallic deposit on a conductive substrate with intrinsic nano-scale morphology by electrochemical deposition (ED) using baths containing metal salts. The baths could be either acidic or alkaline and a three terminal potentiostat is used for potential control. In this technique the cathode is the substrate where the metal nanoparticles are deposited. The opportune voltage for the controlled reduction is applied for suitable time in an electrolytic bath containing metal salt. This setup can be paired with electroanalytical techniques such as cyclic voltammetry, double pulse and potential step deposition.

Since 1951, thanks to the academic work of Turkevich *et al.*, it is possible to generate gold nanoparticles (AuNP)s in a highly reproducible way by treating hydrogen tetrachloroaurate ($HAuCl_4$) with citric acid in boiling water, where the citrate acts as both reducing and

stabilizing agent.[25] Since then, other species were isolated as good reducing agents for the production of both gold and silver NPs, in particular L-ascorbic acid.[26,27]

Combining the electrochemical deposition of metal from solution to a flat substrate with the use of species such as L-ascorbic acid as stabilizer and template, there is no more need for features in the nano-scale on the substrate for iron and nickel nanoparticles (FeNP, NiNP)s formation. We have chosen both a flat glassy carbon (GC) surface with no nano-scale pattern as well as a nitrogen-doped reduced nano graphene oxide (rGO-N) since it is established in literature that metal and metal oxides nanoparticles interface exceptionally well with nitrogen present in carbon materials.[28–31]

In addition to exploring new catalyst materials, it is also possible to explore new catalyst environments. That is, coatings of microporous materials onto electrocatalyst can beneficially affect the catalytic reaction. The surface of a hydrogen evolution catalyst requires "triphasic" conditions[32,33] in which gas | liquid | solid phase systems coexist and interact. The formation of gas bubbles close to the electrocatalytic interface can be an important aspect of catalyst performance and materials such as polymers of intrinsic microporosity (PIMs) have been proposed to beneficially affect triphasic interfacial reactions by suppressing bubble nucleation and adhesion to surfaces.[34] The electrogenerated gas can permeate through nano-channels in the PIM to then nucleate outside of the polymer film to not block access to the catalyst. PIMs have been introduced to electrochemistry over the last ten years[35] and shown to provide highly molecular structure-dependent effects. PIMs have highly rigid and contorted molecular backbones to allow dissolution in solvents such as chloroform and poor packing/weak interaction in the solid state. As a result, highly microporous structures are formed with typically 1-3 nm diameter channels.[36] PIMs with tertiary amines in the backbone show pH dependent protonation and ionic conductivity.[37] They have been employed in ionic current rectifying nano-membranes[38] and have been used to immobilize catalysts at electrode surfaces.[39] PIMs without ionic functionality have been employed in photoelectrochemistry,[40] as a precursor for porous carbon,[41] in lithium ion batteries[42] and in membranes for redox flow systems.[43,44] In this study the microporous polymer PIM-1 is employed (Scheme 1). PIM-1 has been used previously for the absorption[45] and permeation/separation of gases.[46]

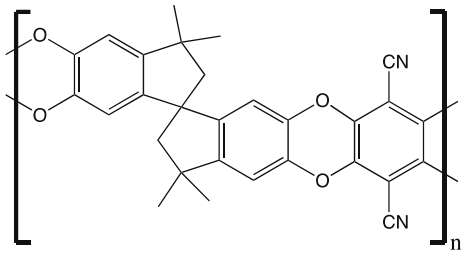

Scheme 1 Chemical *structure* of the p*olymer of intrinsic microporosity PIM-1*.

Methods and Principles

To have a comprehensive understanding of the morphological characteristics of materials produced by techniques that put a big emphasis on the word “nano” is indeed of prime interest. For this objective Atomic Force Microscopy (AFM) and Scanning Electron Microscopy (SEM) were used as imaging technologies powerful enough to resolve any structure of the order of the nanometer.

Atomic Force Microscopy

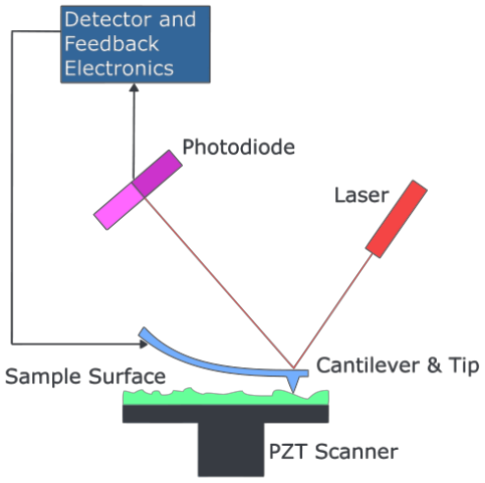

Scheme 2 Real basic scheme of an AFM setup.

The diffraction-limit of visible light photons make it impossible to resolve features of a material worthy of the suffix “nano” with a conventional microscope for as big and expensive it can be. AFM gets around such problem using a completely different approach: an extremely sharp tip at the end of a metal cantilever grazes the surface of the sample interacting with the atomic forces present at nanometric heights. The cantilever is moved by a piezo system for a high precision of movement and, during imaging, the tip scans the surface registering the force coming from its interaction with the sample. The cantilever, in fact, act as a spring, bending a linear amount with the applied force. A visible light laser is reflected on the upper face of the cantilever to a square shaped detector divided in four sectors. At rest each sector should receive the same amount of laser light; every interaction

of the tip with the sample will bend the cantilever which in turn will change the reflecting angle and the signal will be registered as a difference in the received light by each sector.

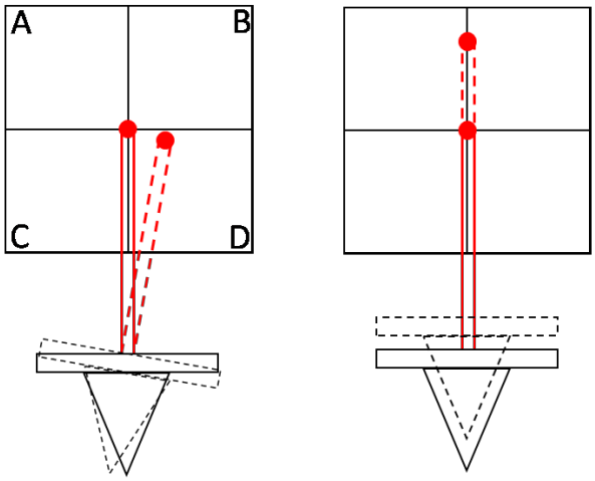

Figure 1 Diagrams showing how the cantilever movement affects the laser trajectory at rest (solid line) and interacting (dashed line). A, B, C and D are the four sectors of the detector.

The raster scan of the tip is slow, measured in few lines per second consuming multiple minutes to obtain a single complete image. The end result is an image (usually a square) of the three-dimensional shape (topography) of the samples surface with a resolution that can go down to the single nanometer. The surface topography is commonly displayed as a pseudo color plot and it can be complemented with information on stiffness or adhesion strength and electrical properties such as conductivity or surface potential that can also be visualized in parallel images of similar definition. The scans can be performed in normal atmosphere or on wet surfaces.

The AFM setup can be also used for atomic manipulation where the forces between tip and sample can be used to change the properties of the sample in a controlled way. Examples of this are nano-lithography and, in biological systems, stimulation of single cells. The most popular mode used during imaging is the *tapping mode*: every cantilever, being a spring-like object, have a resonance frequency (50 to 500 kHz) used to make the tip to consistently oscillate with an amplitude greater than 20 nm and gently contacting the surface at the oscillation vertex. Since conventional contact mode can easily be plagued by problems with friction and adhesion, by having the tip interacting with the surface briefly, tip-sample adhesion forces are greatly reduced. Tapping mode inherently prevents the tip from sticking to the surface, causing damage during scanning and pulling sample sideways

(since the force is always vertical). The laser is indeed oscillating with the same frequencies on the detector, this means the interaction is registered as an average of its position.

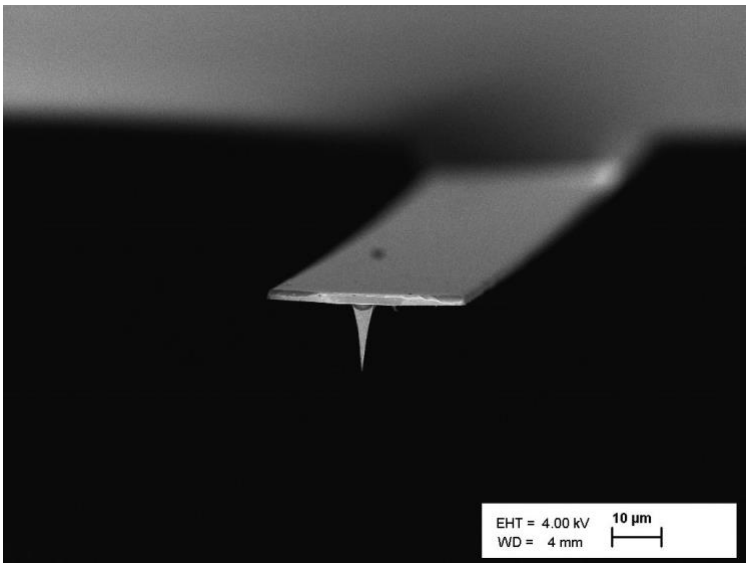

Figure 2 The tip of an AFM cantilever is so small is impossible to resolve in detail using visible light and is a perfect example of an object easily observable trough a scanning electron microscope. Here is possible to visualize its extreme sharpness.

Scanning Electron Microscopy

A Scanning Electron Microscope (SEM) is one of the two main types of electron microscopes (the other one being the transmission electron microscope). SEM devices produce images of a sample by scanning the surface with a focused beam of electrons. Similarly to the AFM, the electron beam is deflected in a raster scan pattern over the area selected for imaging but a complete scan happens multiple times per second allowing a real time response perceived by the operator. The processed signal comes from (i) the returning secondary electrons extracted from the sample by the focused beam of primaries, (ii) the primaries themselves elastically deflected back by the sample and (iii) X-rays emitted when the electron beam removes an inner shell electron from the sample causing the upper shell electron to fill the vacancy emitting the surplus energy as X photon. Secondary electrons energies are small, on the order of 50 eV, which limits their mean free path in solid matter. Consequently, they can only escape from the top few nanometers of the surface of a sample allowing to “peak trough” only those few nanometers. This technique reaches resolutions down to the single nm or below. Back-scattered electrons

have much higher energy than secondary electrons, they emerge from deeper locations within the specimen and, consequently, the technique trades resolution for the ability to probe deeper levels. the intensity of the back scattered electrons signal is strongly related to the atomic number of the specimen, generating a contrast between lightweight and heavyweight elements and making possible to provide crude information about the distribution of different elements in the sample. The energy or wavelength of the X-rays can be measured by spectroscopy and used to precisely identify heavy elements and mapping their distribution. The primary electron beam is produced by a Schottky-emitter, a metallic filament heated over the emission temperature. The free electrons are then accelerated by an electric field measured in kV and focused by magnetic coils. The resulting electron beam is very narrow, this is why SEM micrographs have a large depth of field yielding a characteristic three-dimensional appearance useful for understanding the surface structure of a sample. Magnifications range from x10 to x500k, about 250 times the theoretical limit of the best visible light microscope.

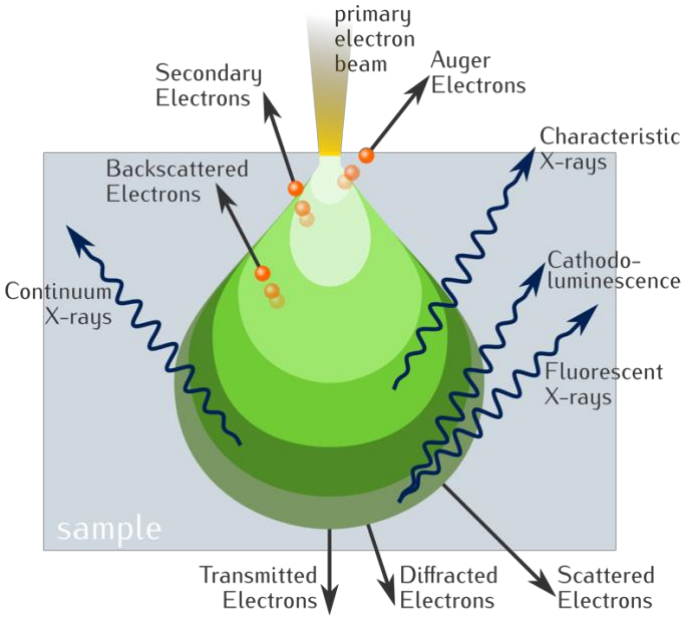

Figure 3 Electron–matter interaction volume and types of signal generated

To prevent accumulation of static charge from the electron beam the sample must be grounded and conductive. Charge accumulation can create image artifacts up to render completely unrecognizable the object of analysis. Some non-conductive specimens are coated with an ultrathin coating of electrically conducting material (it can be gold, platinum, iridium, tungsten, chromium, osmium and even graphite), deposited on the

sample either by low-vacuum sputter coating or by high-vacuum evaporation. The coating is measured in tens of nm.

Electrosynthesis of Metal Nanoparticles and HER Characterization

Experimental section

Materials and General Experiments

L-ascorbic acid ($C_6H_8O_6$, ≥ 99%), Na_2SO_4 (≥ 99%), Na_2HPO_4 (≥ 99.5%), $CuSO_4 \cdot 5H_2O$ (≥ 98%), $CuCl_2$ (99%), Cl_2Zn (≥ 98%), NaCl, (≥ 99%), $NiCl_2$ (98%), acetone (99.5%), isopropyl alcohol (≥ 98%), dichloromethane (≥ 99.8%), dimethylformamide or DMF (≥ 99.9%), were obtained from Sigma-Aldrich and used without further purification, $FeSO_4 \cdot 7H_2O$ (≥ 99%) was obtained from Carlo Erba directly from bottle. Argon (Pureshield, BOC) was employed to de-aerate electrolyte solutions. Aqueous solutions were prepared with ultra-pure water of resistivity not less than 18.2 MΩ cm (at 20 °C) from a Thermo Scientific water purification system. The reduced graphene oxide systems doped with nitrogen have been synthesized following a slightly modified literature procedure.[47,48] PIM-1 was synthesized following a literature recipe.[49] Electrochemical experiments conducted in H_2O were performed in a glass cell (custom-made), with a platinum wire as counter electrode (CE), a KCl-saturated calomel electrode (SCE) as reference electrode (RE), experiments conducted in DMF in an air tight glass cell (custom-made) with a platinum wire as CE and a silver wire as RE. The working electrode (WE) was prepared from glassy carbon (Tokaicarbon, fine carbon SA-1). Experiments in acidic conditions run on a Biologic SP-300 potentiostat situated in Bologna, Italy, while experiments in sea water like solution run with an Ivium Compactstat potentiostat (Ivium, Netherlands) situated in Bath, UK. Atomic Force Microscopy (AFM) images taken were performed in air with a Digital NanoScope 3D Multimode microscope (Veeco, USA) using phosphorus n-doped Silicon probes (spring constant, 20–80 N/m; resonance frequency 290–330 kHz; nominal tip radius <10 nm) and operating in tapping mode. Scanning Electron Microscopy (SEM) images were obtained using a field-emission scanning electron microscope (FESEM, JEOL JSM-6301F) after keeping samples in vacuum for 24 hours and with an applied 10 nm chromium coating.

Sample Preparation

Metal nanoparticles were deposited via electrodeposition on a flat glassy carbon electrode (GC, Tokai Carbon). The electrode was approx. 20 mm × 8 mm cut with a diamond blade. Eight GC slabs were cut for use in this work with reuse after cleaning and polishing. Before every experiment the GC slab is polished manually on a polishing cloth (Buehler micro-cloth) imbued with a suspension of alumina 0.3 micron (Buehler, UK). After flushing with distilled water, the polished electrode is sonicated for 5 min in acetone and 15 min in isopropyl alcohol. Finally, immersion in dichloromethane completed the last washing step. Both faces of the slab were conductive with only one being flat and useful. The rough side was consequently isolated with Kapton polymer tape.

Technique development using iron sulphate salt

The first validation of the effectiveness of the technique was done using L-ascorbic acid and iron sulfate 30 mM each. The substrate of choice was a slab of GC cut approximately 1 cm x 2 cm. The potential was applied with a CV from 0 mV to -1700 mV, 50 mV/s scan rate. CV was preferred to a chronoamperometry to have a better understanding of the processes involved by clearly visualizing them as they occur. A feature exclusive of CVs very important here since the novelty of the explored deposition method.

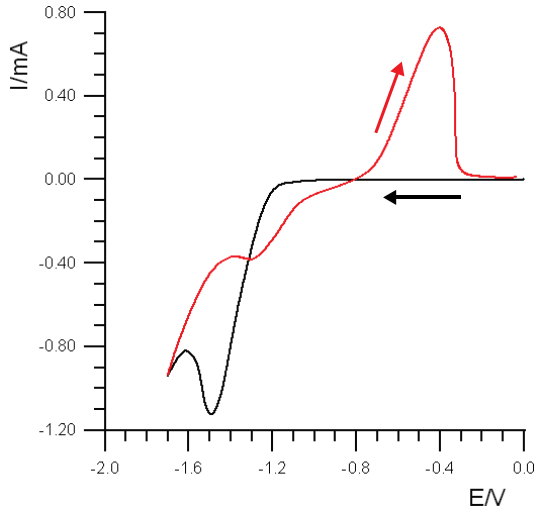

Figure 4 CV from one of the first synthesis of iron NPs. l-ascorbic acid 30 mM, $FeSO_4$ 30 mM, Na_2SO_4 40 mM, scan rate 50 mV/s. WE: GC slab, RE: SCE, CE: Pt. Ag atmosphere, T = 298 K.

The results shown in Figure 4 are what you would expect from a successful synthesis of a metal layer with subsequent stripping visualized as the positive current wave near the end of the cycle. The first wave peaking at -1.5 V corresponds at the metal being reduced, the second wave present on the return segment (red) is the H_2 now evolved by the newly formed metal layer. The stripping lead to a total loss of the deposit. To successfully retain the metal deposit CVs must never reach potentials higher than -0.8 V. By repeating the cycles multiple times from -0.8 V to -1.5 V (example of this synthesis in Figure 5), the submersed part of the GC slab developed a metallic look and bubbles of hydrogen being generated by the catalytic properties of the new surface, were visible to the naked eye evolving from the sample.

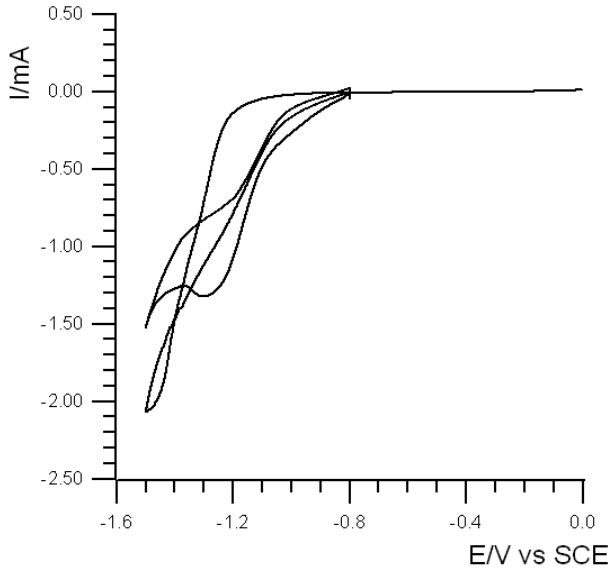

Figure 5 Iron deposit synthesis CV. 30 mM l-ascorbic acid, 30 mM $FeSO_4$, 40 mM Na_2SO_4. Scan rate 0.05 V/s. WE: GC, RE: SCE, CE: Pt. Ag atmosphere, T = 298 K.

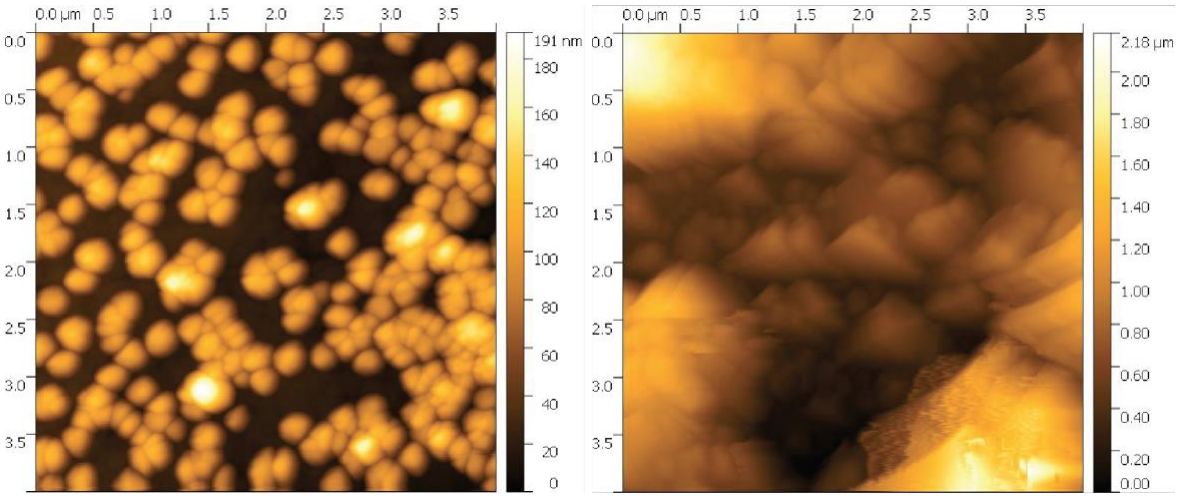

Figure 6 AFM image of iron NPs grown on GC from a solution 30 mM L-ascorbic acid, 30 mM $FeSO_4$, 40 Na_2SO_4 (left) and AFM image of iron grown from a solution 30 mM $FeSO_4$ 70 mM Na_2SO_4 (right).

AFM setup was used to confirm the formation of a nano-morphology of the metal layer. Meso-scale iron particles of around 250 nm were indeed present on the active surface. A control experiment was devised by running the CVs without the stabilizer. No nano-structure was visible in the control sample. The comparison between the two morphologies can be seen in Figure 7.

To better understand the influence of the various components many samples were synthetized exploring the effects upon changing each one of them. In table 1 are shown some of the combinations of metal concentration, stabilizing agent, solvent, CV cycles of synthesis and substrate nature that were explored to compare the effects on particle formation.

Table 1 Each row represents a different experiment. The seven listed here are a limited sample of the many combinations that were explored. Stabilizing agent concentration was always kept at 30 mM. CNT@ and rGO-N@ refers to nitrogen-doped carbon nanotubes and graphene casted on top of the GC slab as additional surface modification.

Metal concentration (mM)	stabilizing agent	solvent	N° cycles	substrate
30	ascorbic acid	H_2O	6	GC
10	cistamine	H_2O	6	GC
10	ascorbic acid	DMF	6	GC
10	ascorbic acid	H_2O	6	GC

10	ascorbic acid	H_2O	6	CNT@GC
30	ascorbic acid	DMF	6	rGO-N@GC
3	ascorbic acid	DMF	12	GC

In addition to ascorbic acid other substances were investigated such as cistamine, lipoic acid and diazonium salt, but none of them lead to a better-defined nanostructure (Figure 7) nor clear improvement on HER performance. On the other hand, iron salt concentration was overall the biggest factor to influence particle size with CV cycles number only influencing the total final area coverage. By lowering the salt concentration, it was possible to shrink particle diameters of one order of magnitude. DMF was used as an organic alternative to the solvent, chosen as it is able of dissolve both metal salt and L-ascorbic acid, resulting in stable deposits with no visible stripping down to 0 V.

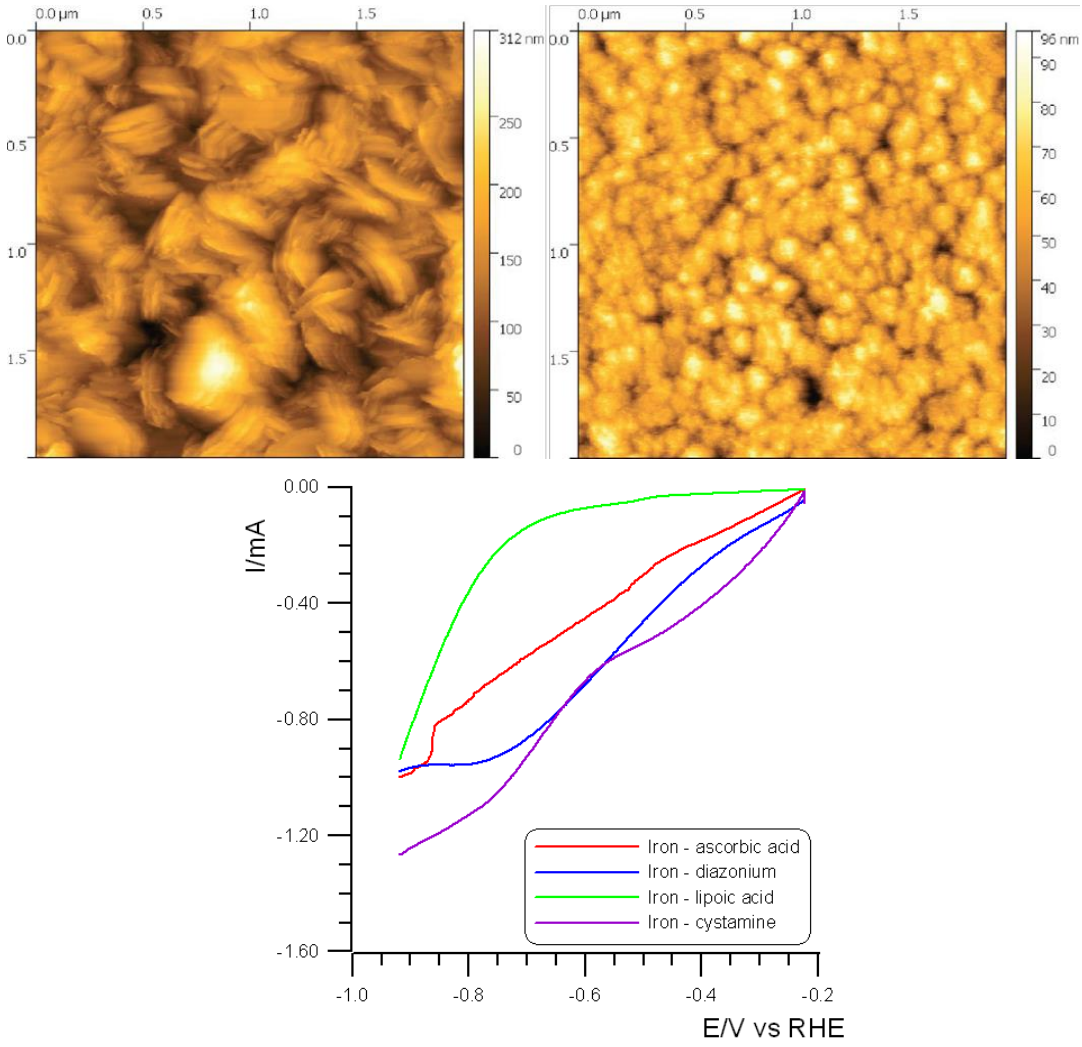

Figure 7 AFM images of deposits resulting from synthesis in presence of cistamine (left) and diazonium salt (right). HER performance characterization in 0.1 M pH 4 buffer solution of iron deposits (bottom). Scan rate 0.05 V/s. WE: GC, RE: SCE, CE: Pt. Ar atmosphere, T = 298 K. E corrected vs RHE.

Effect of cycles number and scan rate.

The higher the number of cycles during the synthesis CV and thus longer the procedure the better performance the sample gives as shown in Figure 8a, suggesting a progressive increase in active surface available for H_2 production. In a similar way, increasing the scan rate lead to a very clear lower activity (Figure 8b).

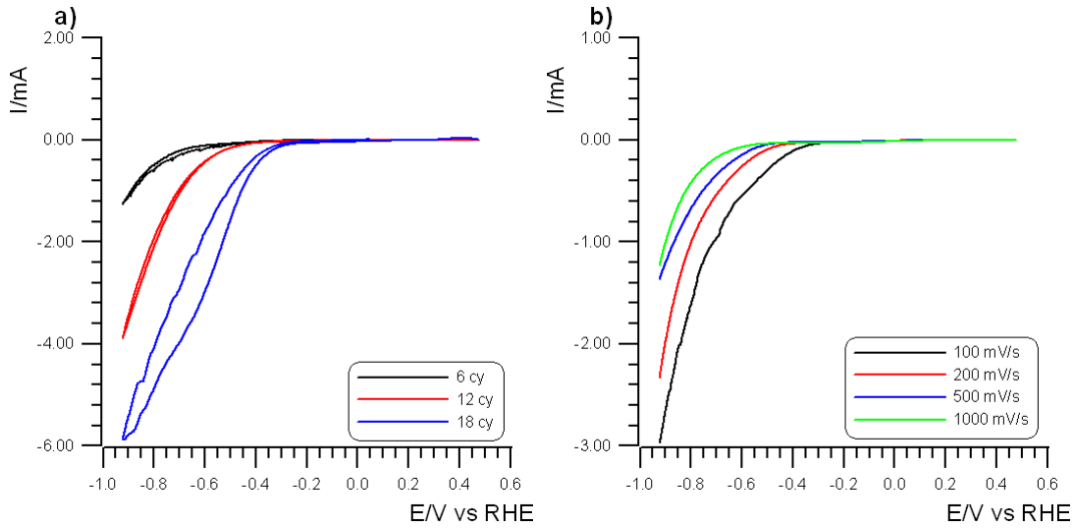

Figure 8 Activity comparison of samples distinguished by number of cycles at scan rate 100 mV/s (a) and by scan rate with fixed 18 cycles (b).

Technique development using nickel chloride salt

AFM and SAM analysis confirmed the technique to be effective with a nickel salt as well with a platinum salt (Figure 9). Using $NiCl_2$, l-ascorbic acid as capping agent and KCl as electrolyte the result was a high coverage of fairly monodisperse nickel nano-particles (Ni-NPs) and the same was true (Pt-NPs) using K_2PtCl_6 as precursor.

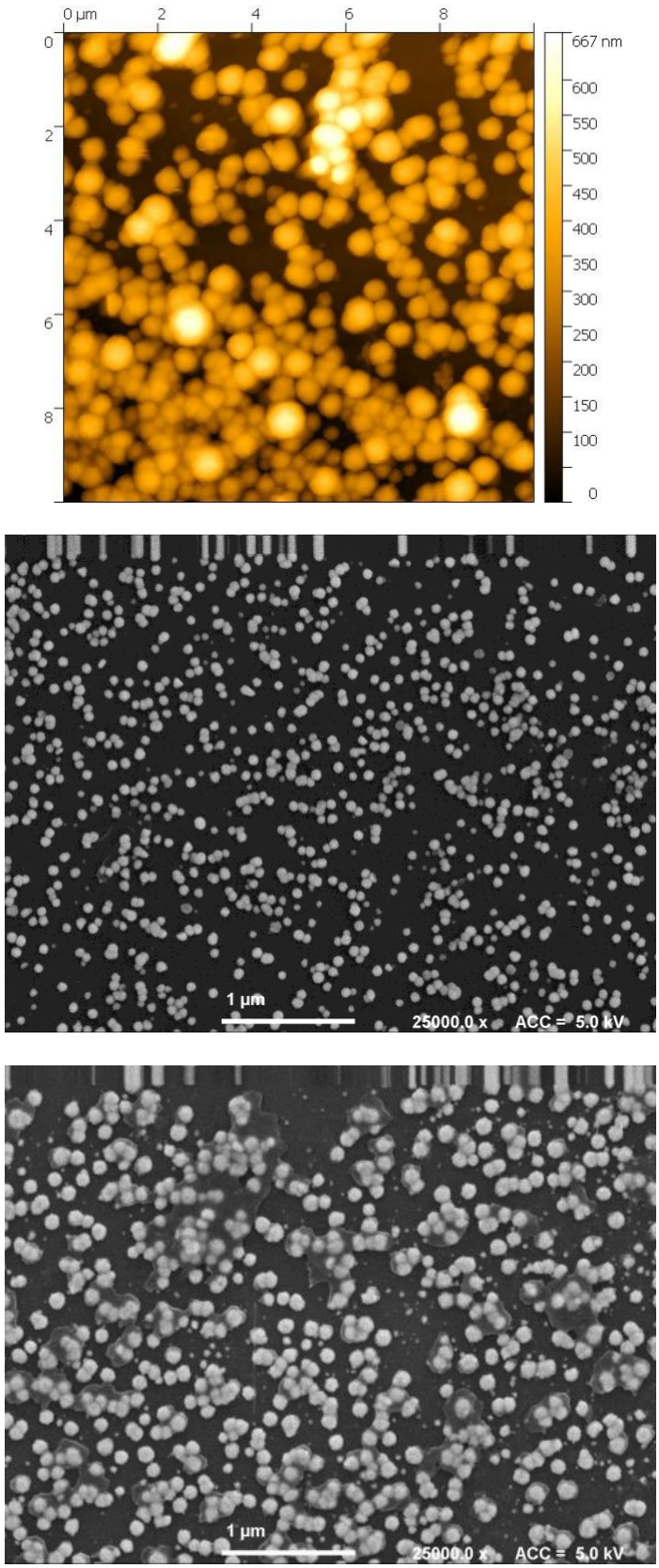

Figure 9 AFM image of Ni metal nanoparticles (Ni-NPs) on GC synthetized using $NiCl_2$ 30 mM l-ascorbic acid 30 mM, KCl 40 mM and the same setup as for iron samples (top). SEM image of nickel nanoparticles grown on flat glassy carbon (middle) from H_2O solution of 70 mM KCl, 30 mM L-ascorbic acid, 1 mM NiCl. Magnification 25k. SEM image of Pt nanoparticles grown on GC (bottom) from H_2O solution of 70 mM KCl, 30 mM L-ascorbic acid, 3 mM K_2PtCl_6. Magnification 25k.

As a routine, Ni-NPs and Pt-NPs were prepared using 18 potential cycles were employed under conditions as reported for Figure 10.

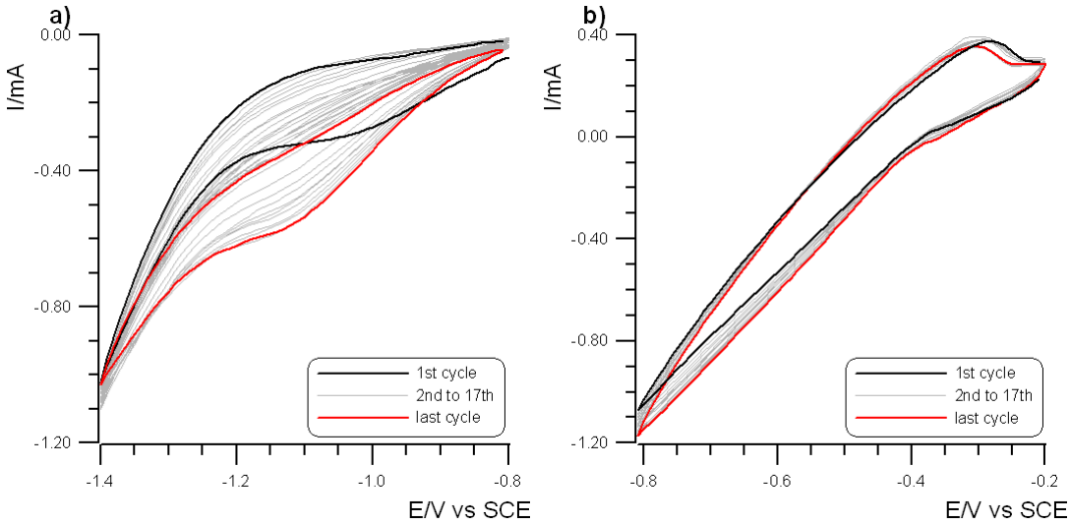

Figure 10 Cyclic voltammetry data (scan rate 50 mV/s, T = 298 K) for metal nanoparticle growth. Electrode surface progressive modification followed by current magnitude changes over time/cycles. (a) Ni-NPs growth in 70 mM KCl, 30 mM L-ascorbic acid, 1 mM $NiCl_2$ on bare GC. (b) Pt-NPs growth in 70 mM KCl, 30 mM L-ascorbic acid, 1 mM K_2PtCl_6 on bare GC.

In DMF synthesis gives a more stable Ni-NPs deposit which electrochemically can be appreciated as an absence of the stripping peak during the entire potential scan down to E = 0.0 V (compare with Figure 4).

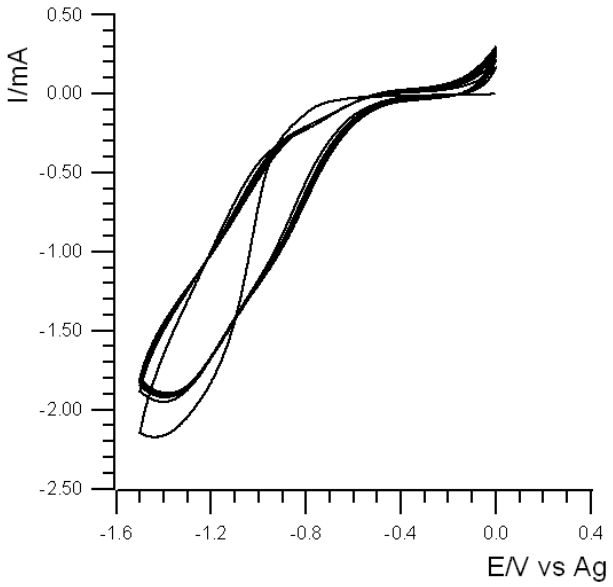

Figure 11 Nickel deposit synthesis CV in DMF. 30 mM l-ascorbic acid, 30 mM $NiCl_2$, 40 mM TBAH. Scan rate 0.05 V/s. WE: GC slab, RE: Ag wire, CE: Pt wire. Ar atmosphere, T = 298 K.

Just like Fe-NPs, particle diameter is affected mainly by the metal ion concentration in solution. Experiments with concentrations of 30, 10, 3 and 1 mM of $NiCl_2$ strongly show evidence of this correlation in AFM (Figure 12).

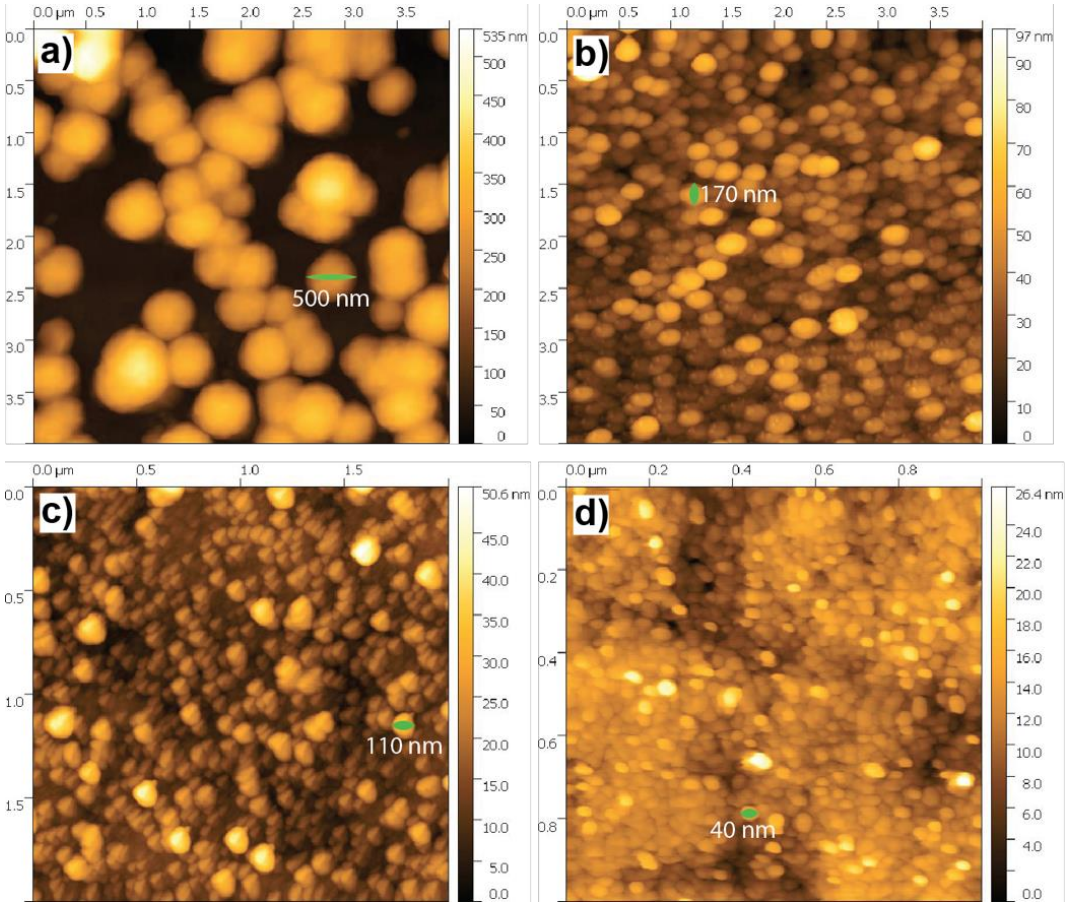

Figure 12 AFM images of NiNPs synthetized from solutions respectively 30 mM (a), 10 mM (b), 3 mM (c) and 1 mM (d) of $NiCl_2$.

After synthesis the catalytic properties of the samples were tested in a pH 4 buffer solution of formic acid 0.1 M and the results are displayed in Figure 13.

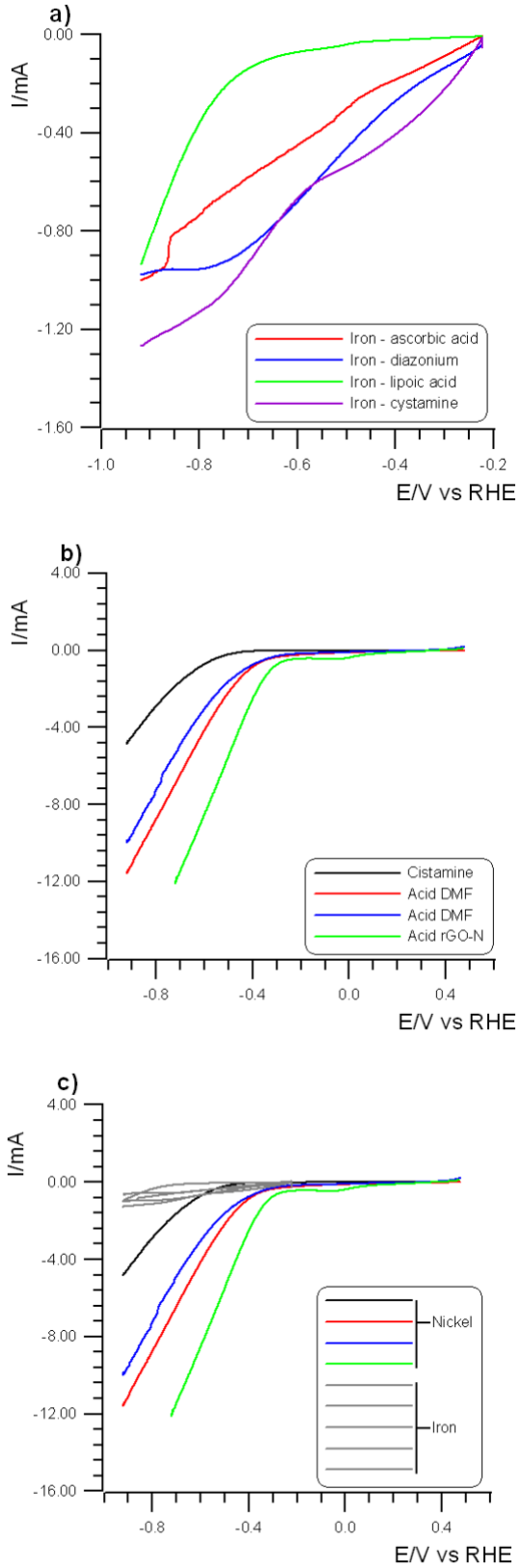

Figure 13 Sample characterization in 0.1 M pH 4 buffer solution of Fe-NPs (a) and Ni-NPs (b). Negative current wave is associated with hydrogen evolution. To show the remarkable difference in performance between Iron and nickel, Iron curves have been juxtaposed in the nickel graph colored in grey (c). Scan rate 0.05 V/s. WE: GC, RE: SCE, CE: Pt. Ar atmosphere, T = 298 K. E corrected vs RHE.

Metal NP tend to have strong interaction with nitrogen in N-doped carbon materials[28–31]. Having readily available N-doped reduced graphene oxide (rGO-N) from the parallel research line discussed earlier a 40 µg drop-cast was performed on top of the GC slab to test the possibility to form a combined graphene-NPs material with this synthesis method. The drop-cast consisted in eight 5µL aliquots were taken from a 1 g/L rGO-N suspension of EtOH/DMF 3/1. A rubber O-ring was positioned on top of the GC slab where the deposit was intended to be grown. The first aliquot was then dropped inside the O-ring and surface tension forces drove the most of the droplet around and under the ring. Once dried the solvent out and removed the O-ring, rGO-N was mostly arranged in a ring shape matching the previous position of the rubber. This distribution of the first material deposited is needed to obtain a fine disk-shaped film as end result. The rGO-N ring act as *wall* to contain in place the successive seven 5 µL aliquots that otherwise would disperse irregularly on the surface and even drop down of the edges of the GC. The resulting deposit is exceptionally uniform and reproducible. In this case DMF was not an option as rGO-N deposits are not stable in organic solvents. This is why a H_2O solution of 10 mM $NiCl_2$ and 30 mM l-ascorbic acid was prepared. SEM imaging proved a successful synthesis and the electrochemical characterization showed a net positive effect on HER performance as it is displayed in Figure 14.

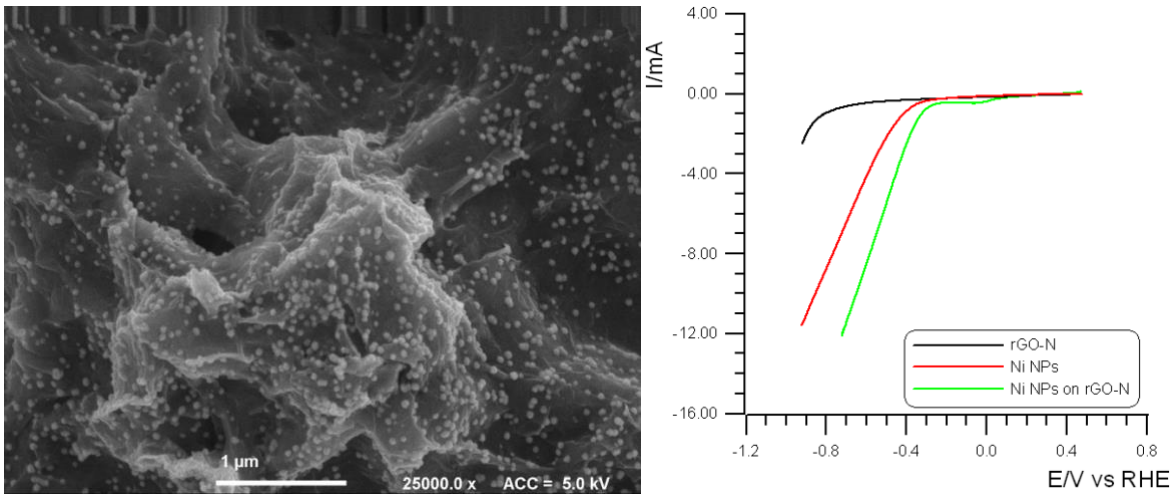

Figure 14 SEM image of nickel nanoparticles grown on rGO-N. magnification 25k. On the side, the electrochemical characterization of rGO-N with no nickel (black), nickel NPs on GC (red) and nickel NPs on rGO-N deposited from the same solution (green).

The introduction a rGO-N delivered improved catalysis even in comparison to DMF based synthesis; in Figure 15 are shown some examples obtained in the improvement process for HER by optimizing the experimental conditions as discussed above.

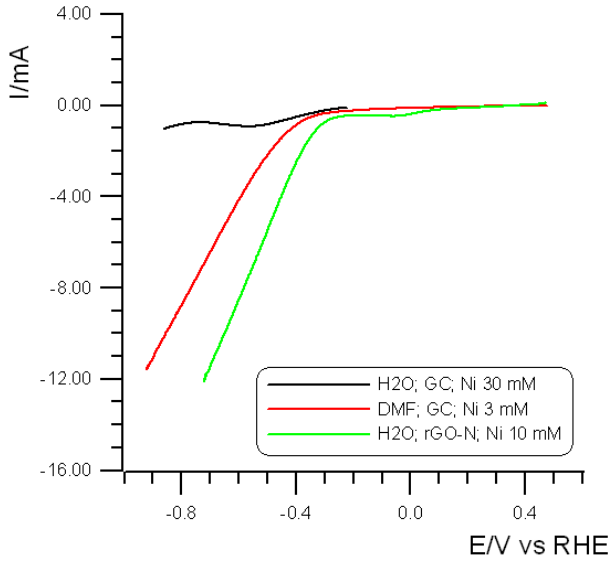

Figure 15 Here is shown the progress achieved from the meso-scale nickel particles synthetized in H_2O (black), to the DMF synthetized NPs (red) and finally to the rGO-N containing sample (green).

H_2 Production from Sea Water

Hydrogen production by splitting seawater using sustainable electrocatalysts and powered by renewable energy from solar or wind is one of the promising alternatives to generate a carbon-free energy vector. The now tested and robust synthesis technique for HER catalyst materials was interesting to use for this application . A solution of 0.5 M NaCl was used for simulating a marine environment during the characterization CVs. In addition, a thin coating of PIM-1 was deposited over the electrode surfaces or it was applied before Ni-NP electro-deposition as a microporous host matrix for metal nanoparticles (Scheme 3).

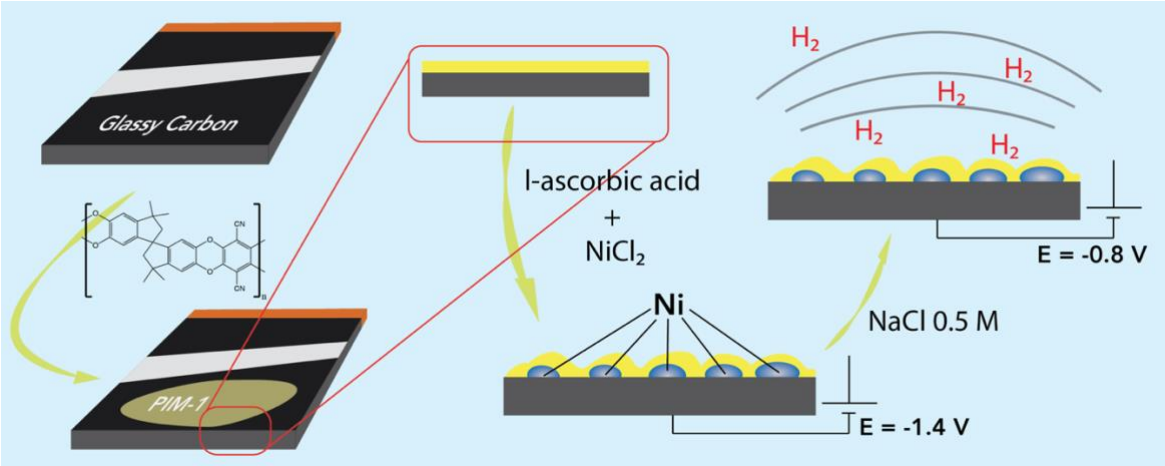

Scheme 3 Graphical representation of the combination of the novel Ni-NPs synthesis technique with the deposition of a polymer of intrinsic micro-porosity membrane.

As a first experiment, a volume of 2 μL of PIM-1 (1 mg/mL in chloroform) was drop-casted on Ni-GC and Ni-rGO-N electrocatalysts. The coated area is approximately 5 mm × 5 mm to give an average film thickness of 80 nm (assuming a density of about 1 g cm^{-3}) .[50] The PIM-1 coating led to a net increase of HER activity, as shown in Figure 16. In addition, Figure 16d clearly shows the presence of a "noisy" current in the absence of PIM-1 coating on Ni-rGO-N, that is completely suppressed in the case of presence of a PIM-1 coating Ni-rGO-N. This behavior can be explained as the consequence of interfacial generation of hydrogen bubbles that interfere with the catalytic process and hence reduce the catalyst efficiency by blocking access to the surface. Experimental evidence suggests that for a triphasic process involving hydrogen bubble formation, the PIM-1 coating can maintain an active catalyst. Here, Ni-NPs remain in contact with the aqueous solution phase (via microporous PIM-1) and HER is maintained. This result prompted us to evaluate the opportunity to grow Ni-NPs directly into PIM-1 coated electrodes.

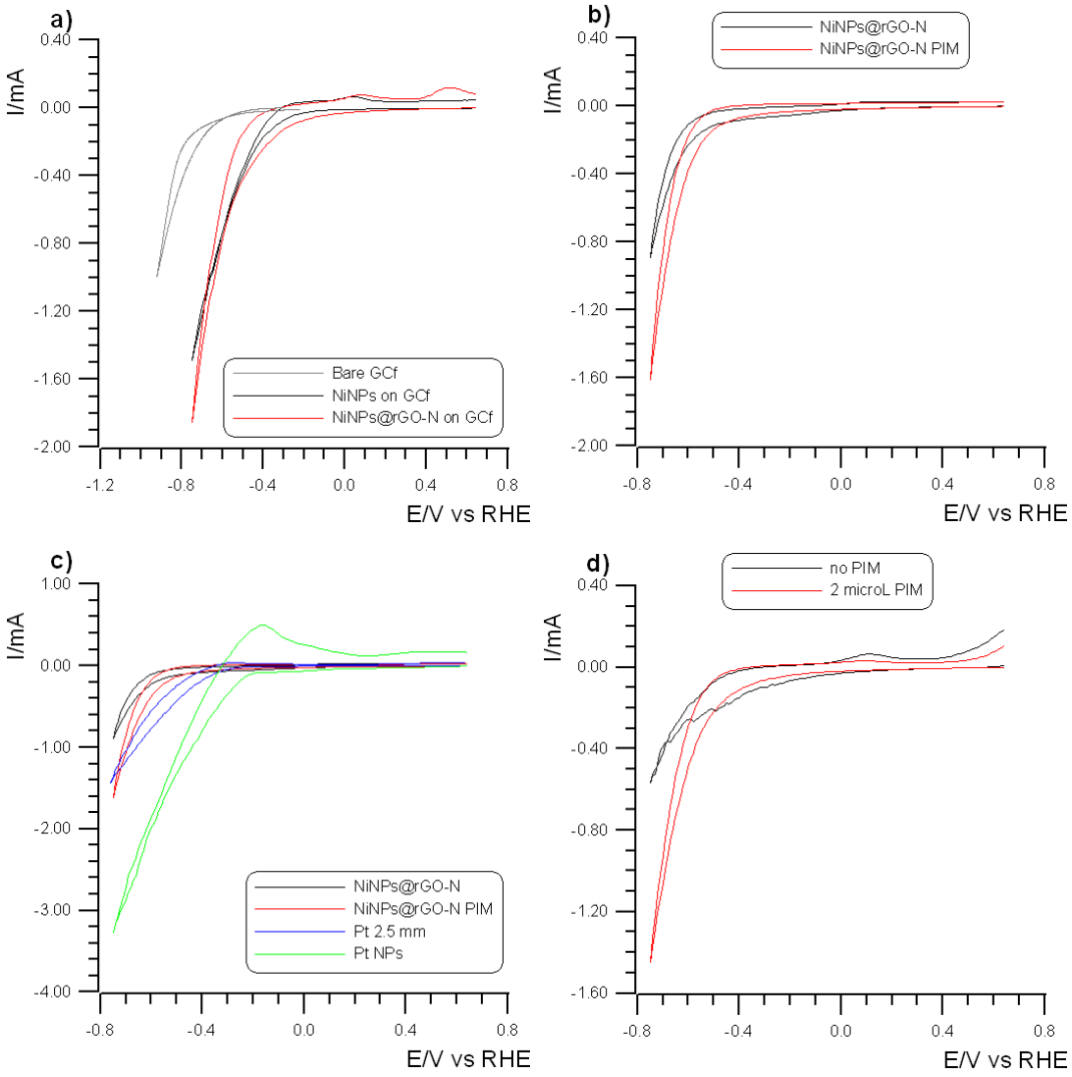

Figure 16 Cyclic voltammetry data (a) in 0.5 M NaCl aqueous solution (scan rate 50 mV/s, T = 298 K) for two Ni-based electrocatalysts (Ni-GC and Ni-rGO-N) and for the bare GC electrode. Comparison (b,c) of catalytic efficiency for nickel nanoparticles on rGO-N without PIM-1 (black) and with PIM-1 (red). Scan rate 50 mV/s, T = 298 K in 0.5 M NaCl. For comparison data are shown for a Pt disk electrode of 2.5 mm in diameter (blue) and for platinum nanoparticles on GC (green). (d) Data showing the effect of the PIM-1 film on nickel nanoparticles on rGO-N when hydrogen bubble formation occurs.

Polymer of Intrinsic Microporosity Effects on Electrolytic Nanoparticle Synthesis

In this section we investigate the nickel ion transport inside PIM-1 micropores. PIM-1 was directly drop-casted on GC or on rGO-N before starting metal electrodeposition. PIM-1 drop-cast followed by solvent evaporation gave rise to non-uniform disk-shaped films with a thicker PIM-1 deposit in the center and thinner PIM-1 films at the edges. This film was then employed in the electrolytic Ni-NP growth. SEM images in Figure 17 show an interesting preferential area for nanoparticle growth preferentially located in the thinner film regions, hence close to the PIM-1 edges. Indeed, only few Ni-NPs were observed outside of the PIM-1 film region and almost none were detected in the central area. This

evidence suggests that a thin deposit of PIM-1 fosters the Ni-NPs electrosynthesis, favoring nucleation/growth processes, and preventing H_2 bubbles from blocking or dislodging the growing nanoparticles. In the case of PIM-1 coated rGO-N, the electrosynthesis of Ni-NPs failed (Figure 17d) likely due to a less controlled thicker PIM-1 deposit obtained on the rougher rGO-N surface. In an additional trial, a more dilute solution of PIM-1 (0.2 mg/mL in chloroform) was prepared and drop-cast to ensure thinner PIM-1 deposits on either GC and rGO-N coated GC.

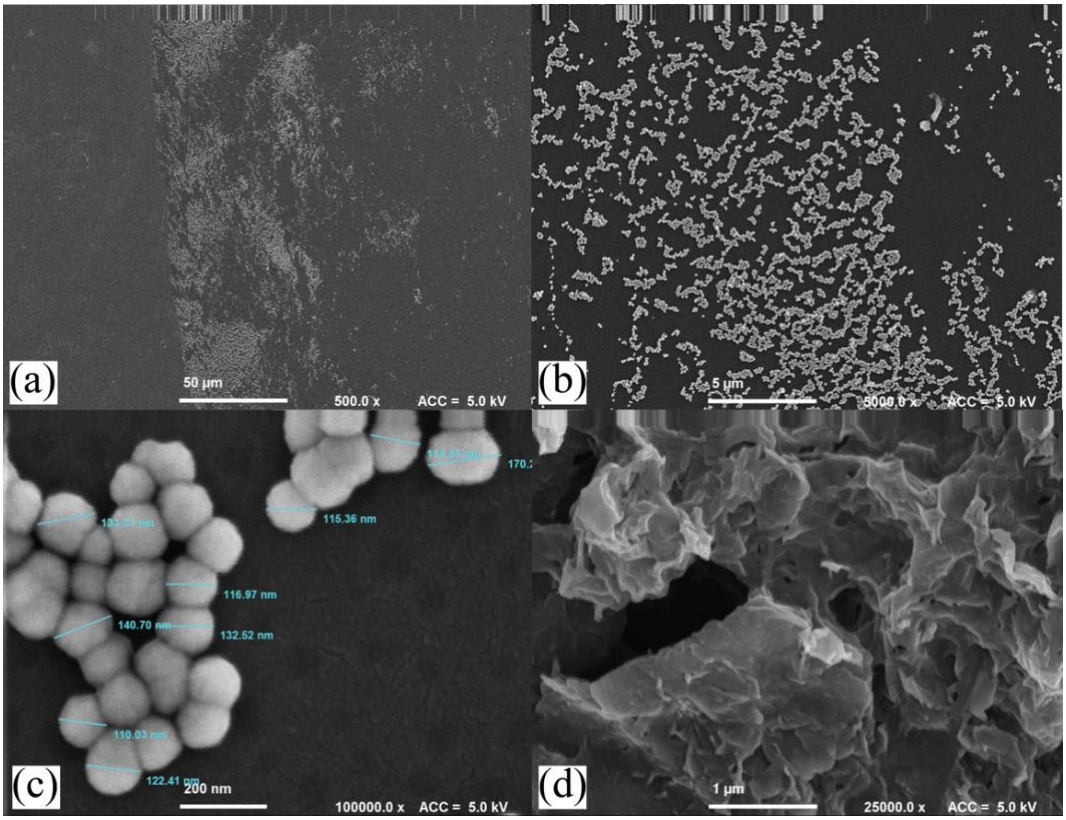

Figure 17 (a,b,c) SEM images of Ni nanoparticles grown under the PIM-1 film. The area with highest nanoparticle density is near the edge of the PIM-1 film in a thinner region. Magnification 500 (a), 5k (b), 100k (c). (d) No visible nanoparticles growth on rGO-N under PIM-1.

Under these diluted conditions (the average PIM-1 thickness is 16 nm nominally) we observed the formation of a much higher particle density along with their more homogeneous distribution all over the thin PIM-1 coating whatever the nature of the support used. Figure 18 a,b shows SEM images for different magnifications of Ni-NPs grown into a PIM-1 thin coated GC electrode. Similarly, c, d show Ni-NPs grown into a thin PIM-1 film deposited on the rGO-N coated GC electrode.

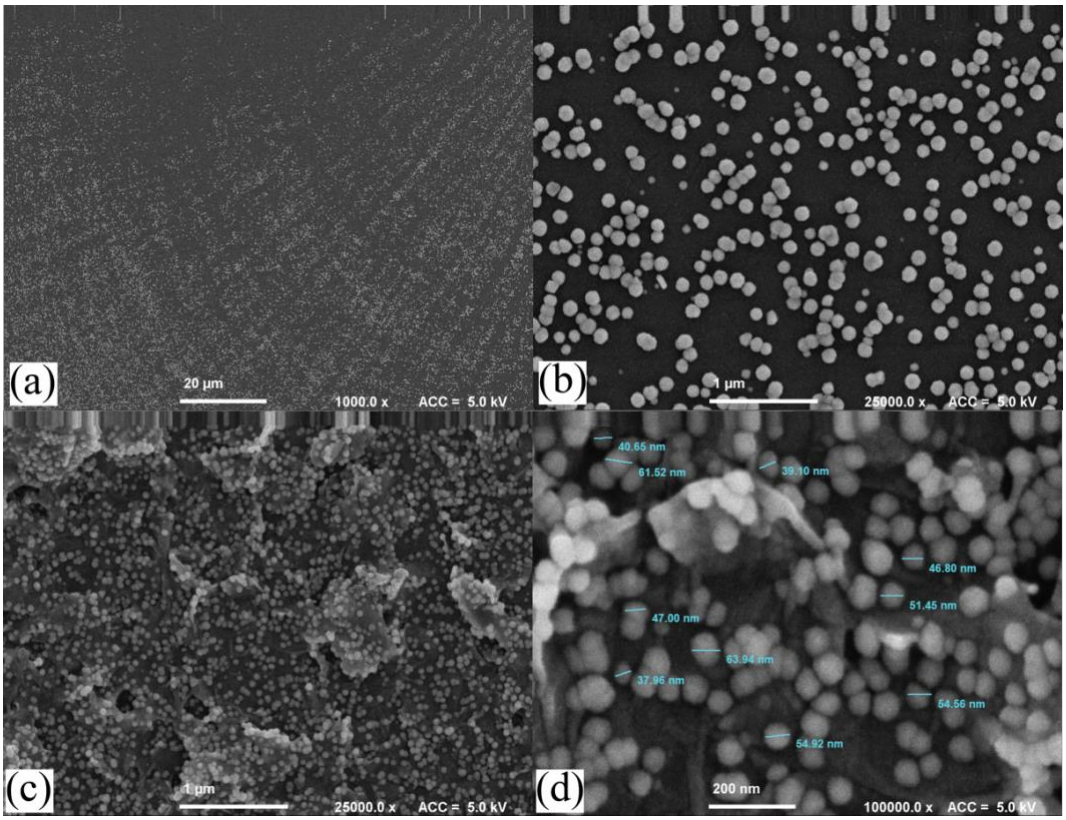

Figure 18 SEM images for PIM-1 coated Ni-GC for electrolytic Ni growth into a thin PIM-1 film. By reducing the PIM film thickness NPs spawn on the whole area. Magnification 1K (a), 25k (b). SEM images for PIM-1 coated Ni-rGO-N for electrolytic Ni growth into a thin PIM-1 film. With a thinner film NPs spawned successfully on rGO-N. Magnification 25k (c), 100k (d).

Remarkably, both composites prepared by Ni-NP electrodeposition into a thin PIM-1 film deposit gave highly performing hydrogen evolution electrocatalysts. Voltammetry data for hydrogen evolution in 0.5 M NaCl are shown in Figure 19. For rGO-N coated GC electrodes (Figure 19a), Ni-NPs grown into a thin PIM-1 film outperformed electrodes prepared directly on the bare GC and followed by a PIM-1 coating treatment. For Ni-NPs prepared by electrodeposition into the thin PIM-1 film coated GC electrode (Figure 19b), the comparison with Pt-NPs on GC shows highly competitive performance for the former electrode with only a slight negative overpotential for hydrogen evolution. The current onset for the Ni-NPs is still more negative compared to data on Pt-NPs, but with currents approaching 2 mA to 3 mA the performance becomes comparable. Figure 19c demonstrates the effect of the PIM-1 coating on enhancing hydrogen evolution.

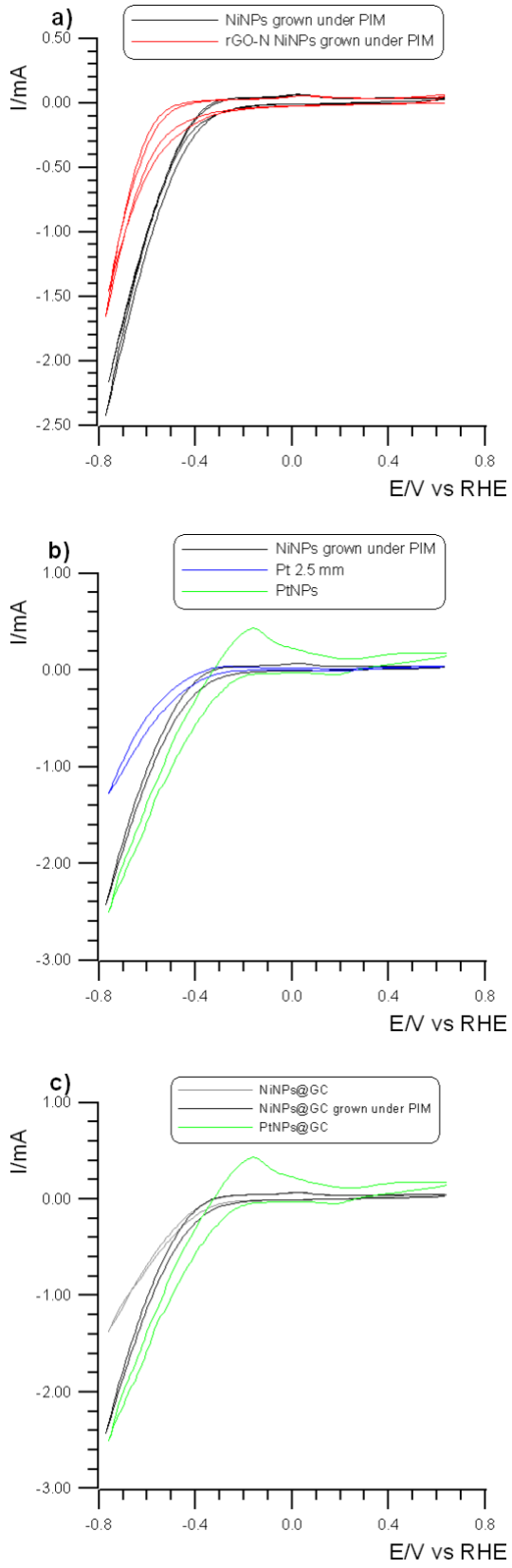

Figure 19 (a) Cyclic voltammetry data (scan rate 50 mV/s, T = 298 K) in 0.5 M NaCl showing the catalytic hydrogen evolution efficiency for Ni nanoparticles grown into a PIM-1 film on GC or on rGO-N. (b) As before, but comparing Ni nanoparticles on GC (black), a Pt disk (blue), and Pt nanoparticles (green). (c) As before, but comparison between Ni nanoparticles on GC (grey), nickel nanoparticles on GC coated with PIM-1 (black), and Pt nanoparticles on GC (green).

All these preliminary data taken together suggest that Ni-NPs grown into a thin PIM-1 film coated GC electrode generate a highly competitive HER electrocatalyst for application such as seawater electrolysis. The formation of Ni-NPs directly electrodeposited into a PIM-1 film appears beneficial. A combination of nickel nanoparticles with PIM-1 coating could be useful also to improve nanoparticle adhesion to the support, thus making the system more robust throughout hydrogen evolution. However, more work will be required on the durability and performance of these types of catalyst films under more realistic conditions. Also, the adhesion of PIM-1 films under the harsh conditions of electrolytic gas evolution will need to be studied more carefully and on a wider range of substrates and over prolonged time. Finally, much better polymers of intrinsic micro-porosity could be developed in the future to provide not only triphasic gas permeation properties, but also good adhesion and long-term stable catalytic performance.

Potential Effect on Synthesis

Relationship between applied potential and particle growth behaviour is hard to study using CVs since, by design, the electrode experiences a window of a linear ramp were voltage is in function of time. To relate morphological properties to potential applied at synthesis Chronoamperometry (CA) is far more useful (Scheme 4). Ni-NPs were synthetized and characterized by AFM, multiple times acting on three variables: reduction potential, step time length and step number (see Table 2). Deposition occurred on the GC slabs from a solution of 30 mM l-ascorbic acid, 70 mM KCl and 1 mM $NiCl_2$ without any changes of the original setup.

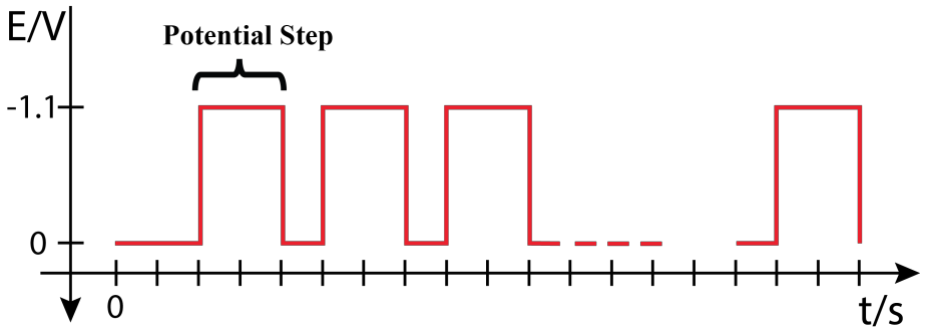

Scheme 4 Schematic representation of the potential relation with time in the CAs used during synthesis. One potential pulse is here referred as "potential step". Every potential step was alternated by a "resting step" at 0 V lasting 2 s. The sample obtained is defined by the voltage of the potential step, its length and the total number of steps occurred during the procedure.

Nickel ions deposition process have an onset potential at -0.8 V vs SCE and slowly reach the wave maximum at -1.15 V (Figure 10a), pH 4 and scan rate 0.05 V/s. Knowing this, a "medium deposition potential" at -1.1 V and a "high polarization deposition potential" at -1.4 V were chosen as potential steps. Samples were divided by 4 s and 12 s Δt and by 6, 12, 18, 36 and 54 deposition steps.

Table 2 Summary of different synthesis parameters for the 9 samples prepared to obtain information on the growth mechanism.

Potential step (V)	Step number	Step time length (s)	Total reduction time (s)
1.1	6	12	72
1.1	12	12	144
1.1	18	12	216
1.4	6	12	72
1.4	12	12	144
1.4	18	12	216
1.1	36	4	144
1.1	54	4	216
1.4	18	4	72

Two of the nine samples presented no metal deposition on the surface (Figure 20). These two cases had some of the mildest synthesis condition (low potential and short time) reason why it could be expected a less complete deposition. Nonetheless the complete absence of particles would suggest no nucleation of the metal crystals, which should not be the case since reduction conditions are met. One explanation could be that small enough particles do not attach to the substrate and are immediately lost to the solution. This would mean a possible size limit for this technique.

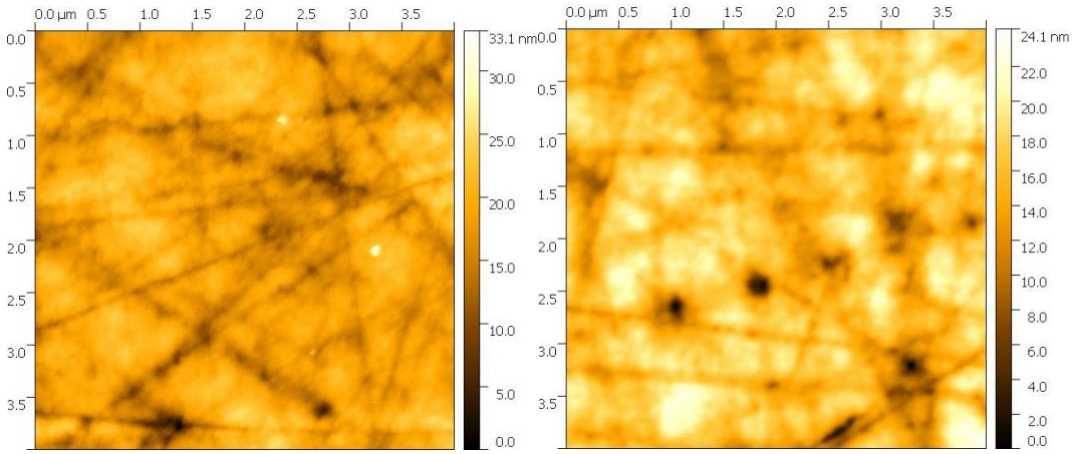

Figure 20 AFM image of the sample synthetized at -1.1 V, 6 steps 12 s long, for a total of 72 s (left). AFM image of the sample synthetized at -1.1 V, 36 steps 4 s long, for a total of 144 s (right). In both cases no particle was present on the surface and the two images present only bare GC.

In Figure 21 two samples prepared in identical conditions are a perfect example of the difference made by the applied potential. The sample here synthetized at -1.1 V, 12 potential steps 12 s long, for a total of 144 s of synthesis time shows the smallest NPs ever recorded in this work with a diameter around 20 nm. Other samples synthetized at -1.1 V do not grow much beyond 30 nm while -1.4 V samples all present what seems at least two rows of NPs: a saturated lower row of small particles 30 nm in diameter and a sporadic upper row of particles with a wide range of size from 60 nm to 150 nm. While the lower potential seams to lead to a homogeneous coverage of a thin layer of metal, higher potentials appear to trigger a second type of deposition on top of the first.

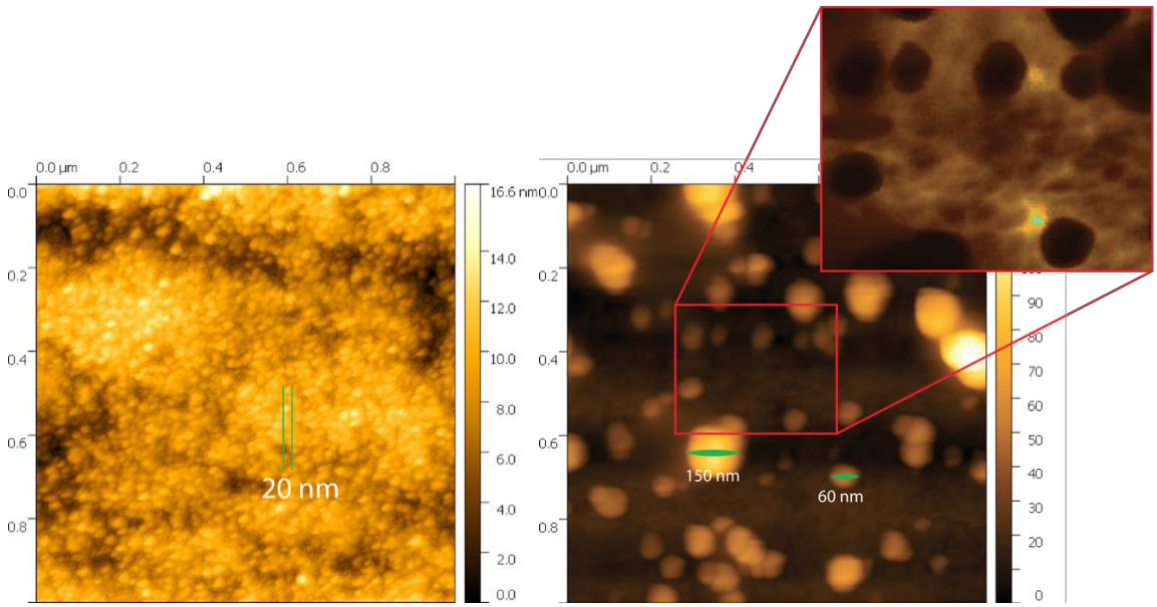

Figure 21 AFM image of the sample synthetized at -1.1 V, 12 steps 12 s long, for a total of 144 s (left). AFM image of the sample synthetized at -1.4 V, 12 steps 12 s long, for a total of 144 s (right). Identical conditions except for applied potential. Left image shows the smaller NPs ever recorded in this work with a diameter of 20 nm. In the right image NPs are organized in two rows. In the upper row particles have sizes that range from 60 to 150 nm.

In Figure 22 is shown a possible connection between number of steps and second-row particle size as the two samples presented were prepared with the same total deposition time of 72 s but divided in different step numbers. A sequence of 18 steps of 4 s seams to give particles double the diameter compared to those grown from a sequence of 6 steps 12 s long.

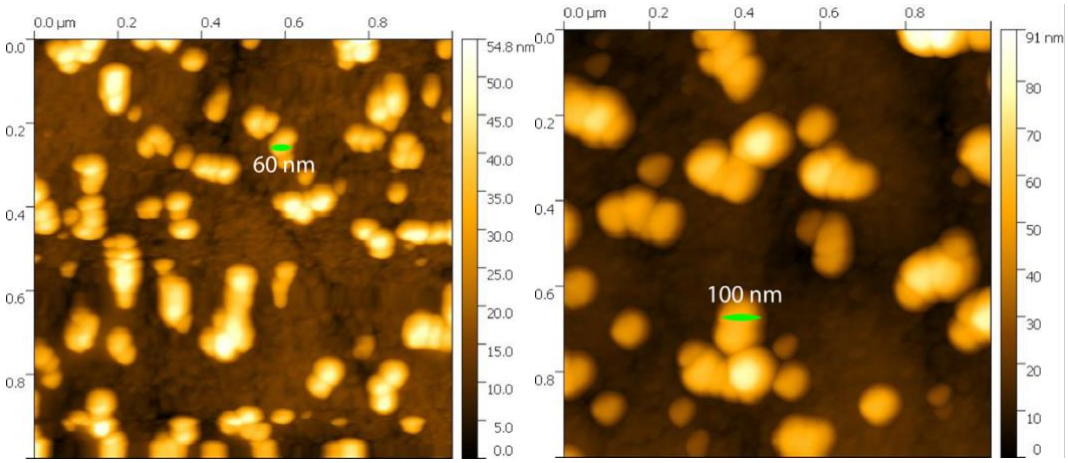

Figure 22 AFM image of the sample synthetized at -1.4 V, 6 steps 12 s long, for a total of 72 s (left). AFM image of the sample synthetized at -1.4 V, 18 steps 4 s long, for a total of 72 s (right). Identical conditions except for step length, the results are similar: in both cases NPs staked in at least two rows. The upper row is made of big NPs that seams bigger at higher step numbers.

Lastly in Figure 23 are shown the three samples with the longer total deposition time of 216 s and as previously stated the biggest difference is made by the applied potential. Samples prepared at -1.1 V have similar appearance while the -1.4 V sample present an uncoherent merging of big particles probably a consequence of the second-row particles seen before growing enough to merge.

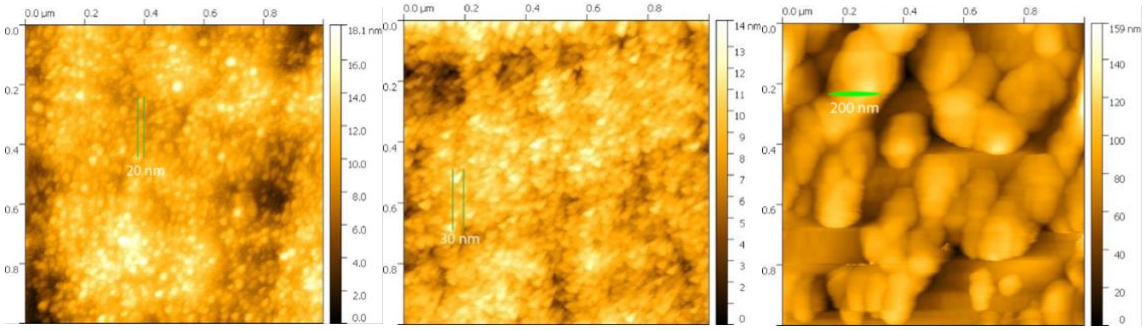

Figure 23 AFM image of the sample synthetized at -1.1 V, 18 steps 12 s long, for a total of 216 s (left). AFM image of the sample synthetized at -1.1 V, 54 steps 4 s long, for a total of 216 s (center). AFM image of the sample synthetized at -1.4 V, 18 steps 12 s long, for a total of 216 s (right). Identical conditions except for total reduction time.

Carbon Dioxide Reduction and Metal Nanoparticles

CO_2 reduction reaction (CO_2RR) is starting to attract a great deal of attention among the techniques of carbon capture and it is suggested as an aid to reach net zero carbon emission alongside the reduction of CO_2 production in the first place. CO_2 reduced to CO or methanol could then be treated as a resource for the chemical industry as those are very versatile organic building blocks or carbon-neutral fuels.[51] High hydrogen overvoltage electrodes with negligible CO adsorption (such as Hg, Cd, Pb, Tl, In and Sn) can reduce CO_2 with a high current efficiency. However, these metals promote reactions were the primary product is formate (only one oxygen bond broken). At the low hydrogen overvoltage metals with a high CO adsorption strength (such as Pt, Ni, Fe and Ti) CO_2 is reduced to form tightly adsorbed CO leading to low turnover frequencies. This low turnover for CO means H_2 becomes the principal product. Research over the past decades has shown the ability of copper to convert CO_2 into hydrocarbons methane and ethylene to be unique among catalysts, with high current efficiencies but still hampered by a relatively high overpotential.[52–54] Research on copper alloys and their morphology for an improved

catalytic efficiency and higher product selectivity has grown into its own field.[55–62] The primary reactions that occur at the copper electrode during the reduction of CO_2 are:[63]

$$2H + 2e^- \rightarrow H_2 \qquad E^0 = 0.0\ V\ vs\ SHE$$

$$CO_2 + 8H^+ + 8e^- \rightarrow CH_4 + 2H_2O \qquad E^0 = 0.169\ V\ vs\ SHE$$

$$CO_2 + 2H^+ + 2e^- \rightarrow CO + H_2O \qquad E^0 = -0.103\ V\ vs\ SHE$$

$$CO_2 + H^+ + 2e^- \rightarrow HCOO^- \qquad E^0 = -0.225\ V\ vs\ SHE$$

To explore the possible production of copper nano-particles (Cu-NPs) and some alloys to add to the capabilities of the new technique here discussed is an obviously intriguing advancement, expanding again its versatility. Starting from a synthesis using only a copper precursor we moved towards mixes of different metal salts for the direct deposition of alloys.

As copper precursor, $CuSO_4$ was initially chosen. A solution of 30 mM l-ascorbic acid 70 mM Na_2SO_4 and 3 mM $CuSO_4$ was prepared and used for synthesis on a GC slab via CV. The voltammogram shows two cathodic peaks and an anodic one respectively at E = -1.1 V, -0.2 V, +0.2 V. The -0.2 V reduction peak relates to the deposition of the metal during the experiment. The oxidation peak is linked to the stripping process as gain intensity with the reduction of Cu^{II} to metallic Cu;[64] in Figure 24b the black line shows a big wave of stripping that quickly disappears in the second cycle due to the depletion of the deposit. After synthesis the slab under the waterline was found covered in a copper-red film almost completely transparent. Figure 24c shows no CO_2RR activity in Na_2HPO_4.

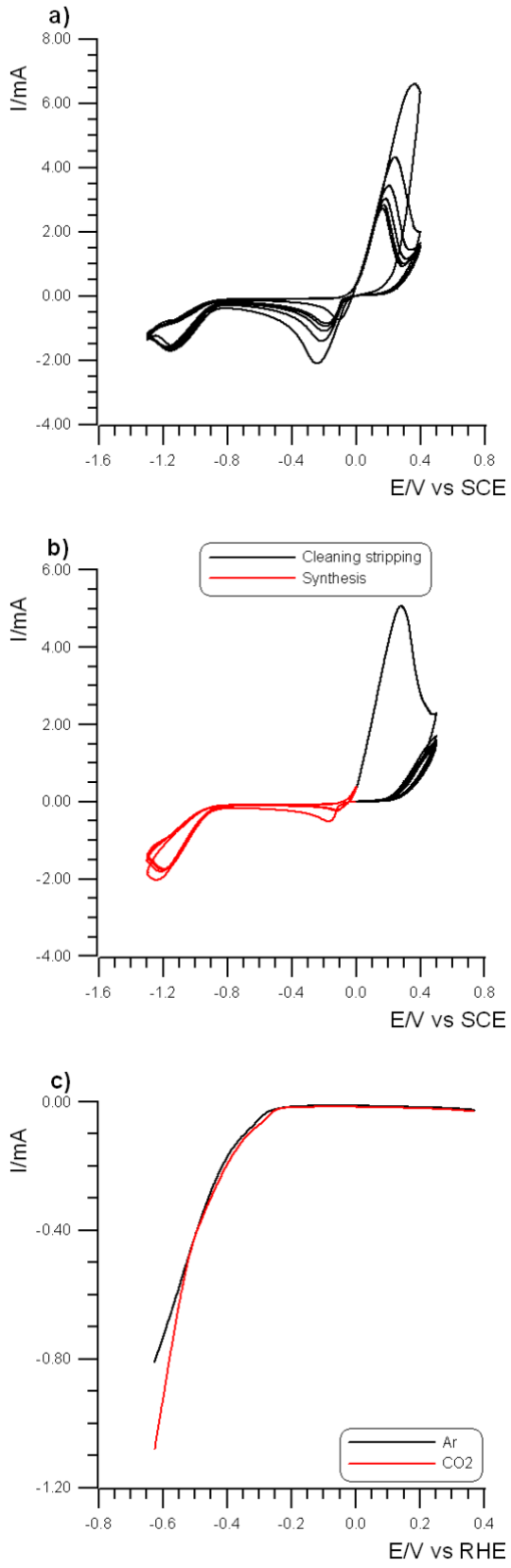

Figure 24 Electrochemical general characterization (a), Cu-NPs synthesis (b) from a solution of $CuSO_4$ 3 mM, l-ascorbic acid 30 mM and $NaSO_4$ 70 mM, Ar atmosphere and CO_2RR characterization (c) in Na_2HPO_4 0.1 M CO_2 saturated. In the voltammogram are visible both the copper reductions at - 1.1 V and - 0.2 V and the stripping starting from 0.0 V. The synthesis (red) was carried out after some stripping cycles (black) to clean the surface of the metal deposited during the characterization. During the 6 cycles of synthesis -0.2 V peak continued to shrink as the deposit grow thicker. Scan rate (a) (c) 0.05 V/s (b) 0.10 V/s, WE: GC, RE: SCE, Ar atmosphere, T = 298 K.

AFM characterization showed particles not very monodisperse around the diameter of 80 nm (Figure 25), not impressive considered previous results using nickel, but the successful generation of a nanostructure was nonetheless promising for the possible formation of copper alloys NPs.

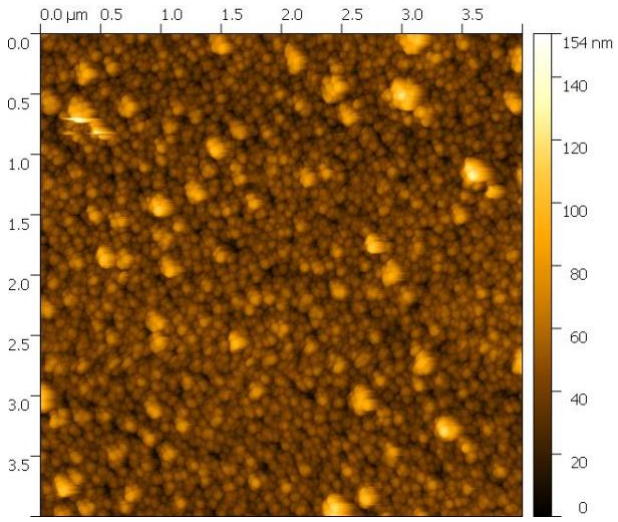

Figure 25 From the AFM image is visible the successful deposition of CuNPs. The deposit was produced from the CV showed in Figure 24b.

The utilization of bimetallic catalysts has been considered a promising approach to obtain improved catalytic performance for CO_2RR.[62,65] Catalytic efficiency could benefit significantly by combining the Cu affinity for CO_2 molecules and the Ni favorable interaction with protons and famous use as a catalyst for hydrogenations in the chemical industry, to possibly speed up the protonation process CO_2 adsorbed on Cu could be protonated from an adjacent Ni atom in a Cu-Ni alloy. A solution of 0.5 mM $NiCl_2$, 0.5 mM $CuCl_2$, 30 mM l-ascorbic acid and 70 mM KCl was prepared and during synthesis potential was kept at -1.8 V vs SCE for 50 s, well above deposition potentials of Cu and Ni to ensure the simultaneous reduction of both metals from the solutions. Aiming to a 1:1 ratio alloy, equal concentrations of Cu and Ni were chosen assuming the metals have similar diffusion coefficient ($\approx 10^{-9}$ cm^2s^{-1})[66,67] and thus the same contribution on the deposition current, as described by the Cottrell equation:

$$i = \frac{nFAc^0\sqrt{D}}{\sqrt{\pi t}}$$

The 1:1 ratio was chosen arbitrarily to ensure a good degree of adjacency between Cu and Ni. In this case, n is the number of electrons exchanged per ion, which is 2 for both, F is the Faraday constant, A is the area of the GC slab in cm^2, c^0 initial concentration of the reducible analyte in mol/cm^3 and D is the diffusion coefficient of the same reducible analyte in cm^2/s.

In Figure 26 the response of the sample to an inert atmosphere and to a CO_2 saturated one is shown. In alkaline buffer of 0.1 M Na_2HPO_4 is evident a considerable faradic contribution (Figure 26b).

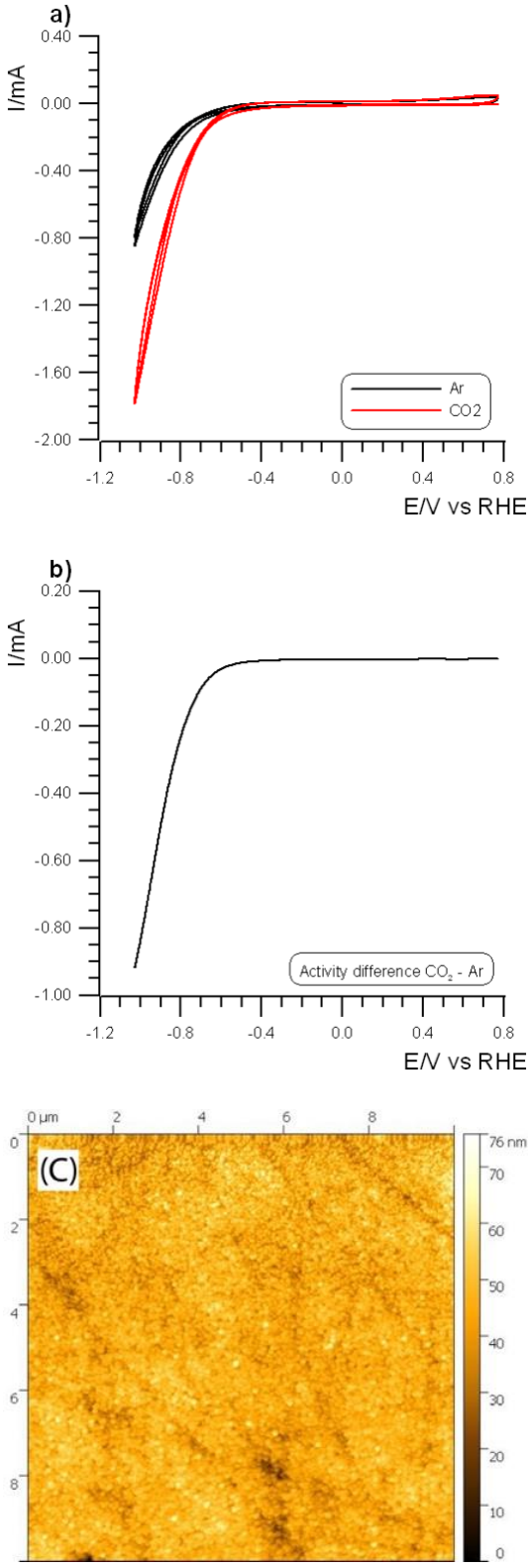

Figure 26 Electrochemical and AFM characterization of NiCu-NPs. Activity comparison in Na_2HPO_4 0.1 M in both inert atmosphere and upon introduction of CO_2 (a). The difference between the two curves isolating the faradic contribution of CO_2RR (b). Scan rate 0.05 mV/s, WE: GC, RE: SCE, T = 298 K. And (c) AFM image showing the successful formation of particle nanostructure.

Recent studies have demonstrated enhanced reactivity of CuZn catalysts for CO_2RR.[55,68–73] CuZn is of particular interest due to its low cost, lack of toxicity and CuZn based catalysts were found to be favorable toward the formation of C_2 products like C_2H_4 and C_2H_5OH with the possibility to tune the ratio of these products by varying the Cu/Zn ratio.[72] This C_2 selectivity is reasonably due to the lateral spillover of CO from multiple Zn to Cu sites, which would facilitate the production of C_2 products at the Cu site. Such CO migration effects were found to be facilitated when a homogeneous distribution of Cu and Zn atoms was formed in the CuZn catalysts maximizing the occasions for Zn-Cu adjacency.[73]

From a solution of 0.5 mM $ZnCl_2$, 0.5 mM $CuCl_2$, 30 mM l-ascorbic acid and 70 mM KCl a dark yellowish film was deposited on a GC slab trough 18 Cv cycles (Figure 27a), suggesting the successful formation of a brass-like alloy, but no elemental analysis was performed to define the metal ratios. The sample was then tested in Na_2HPO_4 in both an inert atmosphere and in a CO_2 saturated one. With an onset potential around -0.8 V vs SCE there was a high current intensity in presence of CO_2 while in Ar little activity was measured. This characterization in showed an excellent CO_2RR activity (Figure 27b) and AFM imaging (Figure 28) confirmed the nanostructure of round, fairly monodisperse, ZnCu-NPs.

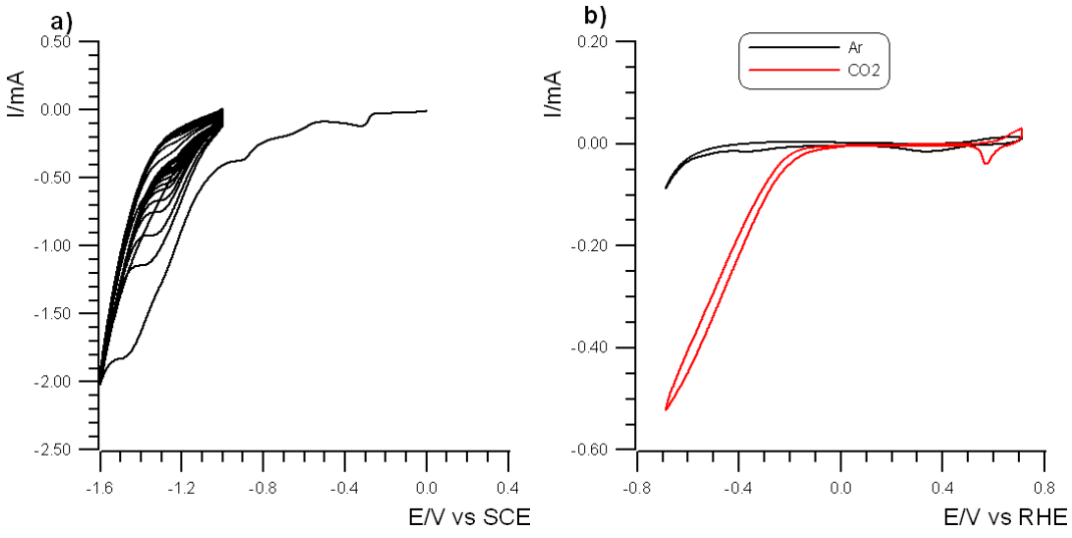

Figure 27 Synthesis (a) and electrochemical characterization (b) of ZnCu-NPs from a solution of 30 mM l-ascorbic acid, 70 mM H_2O/KCl. The CO_2RR performance was tested in Na_2HPO_4 0.1 M. Scan rate 0.10 (a) and 0.05 V/s (b), WE: GC, RE: SCE, T = 298 K.

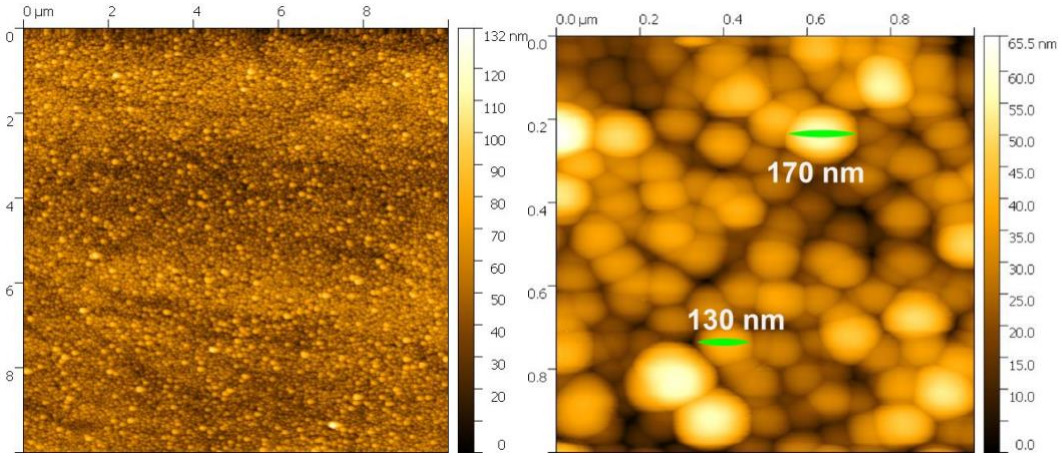

Figure 28 AFM images of a 50/50 Cu-Zn deposition. The film has a yellowish brass-like color and the microscopy reveals CuZn-NPs formation with a diameter between 100 nm and 170 nm.

Conclusions

In this chapter we developed and improved a novel technique to produce on site monodisperse around 30 nm metal nanoparticles from non-noble metal salts. The materials provided demonstrated good electrocatalytic capabilities for HER in both acidic and neutral conditions. By reducing the metal ions in solution in presence of a capping agent as l-ascorbic acid, the resulting metal deposit on the WE presented nanostructure otherwise absent if the capping agent was not introduced. Cistamine, diazonium salts and lipoic acid were also tested as alternative capping agents but ascorbate ensured the synthesis of far better-defined metallic spheres and better overall catalytic performances. The synthetic process was initially developed using $FeSO_4$ but was found to work as well using $NiCl_2$ with far better HER performances. Particle diameter was initially too big to be discussed as nanotechnology, but by reducing the initial concentration of the metal salt down to 1 mM and keeping the electrode polarization down to -1.1 V diameters down to 20 nm were recorded for Ni containing samples with no obvious impediment to reduce the size even more if salt density was to be lowered to 0.5 and beyond. Cu and Cu-Zn alloys were also successfully synthetized in the same way. The Cu-Zn/NPs were especially good catalysts for CO_2RR in good accordance to what has been reported in literature as brass seems to be a far better catalyst than Cu or Zn taken alone. Energy Dispersive X-ray spectroscopy could be used in future research to characterize metal ratios and alloy phase and finetune them to further improve synthesis results and catalytic efficiency. There is room for improvement for this technique and the range of applicability is still far to be completely explored. Its simplicity and versatility justifies further studies.

After the technique was developed and tested and our understanding considered mature enough, it has been shown that well-defined nickel nanoparticle electrodeposits can be formed directly underneath a thin coating of PIM-1. The resulting nickel nanoparticles catalyst in hydrogen evolution was shown to be improved by the PIM-1 coating (mainly due to suppression of interfacial gas bubble formation and the resulting catalyst blocking). This type of electrode was shown to be competitive (at least at higher current densities) when compared to highly active platinum nanoparticle hydrogen evolution electrocatalysts. The thickness of the PIM-1 film coating proved to be critical as thicker deposits suppressed nickel electrodeposition. A thin PIM-1 coating, however, enhanced nickel nanoparticle electrodeposition compared to the case of a bare glassy carbon electrode. The

effect of PIM-1 coatings on suppressing interfacial gas bubble nucleation close to the electrode/catalyst surface could be beneficial also in other areas of electrochemical technology such as carbon dioxide reduction or in fuel cell systems. A wider range of molecular PIM materials could be tested and developed for specific applications.

References

1. Fonseca, J. D., Camargo, M., Commenge, J. M., Falk, L. & Gil, I. D. Trends in design of distributed energy systems using hydrogen as energy vector: A systematic literature review. *Int. J. Hydrogen Energy* 9486–9504 (2019) doi:10.1016/j.ijhydene.2018.09.177.
2. Austrlian Government Chief Scientist. *Hydrogen for Australia's future*. (2018).
3. Alverà, M. *Rivoluzione idrogeno. La piccola molecola che può salvare il mondo*. (Mondadori Electa, 2020).
4. IRENA. *Hydrogen From Renewable Power: Technology outlook for the energy transition*. (2018).
5. BNEF. *Economics of Hydrogen Production from Renewables*. (2019).
6. Ismail, A. A. & Bahnemann, D. W. Photochemical splitting of water for hydrogen production by photocatalysis: A review. *Sol. Energy Mater. Sol. Cells* **128**, 85–101 (2014).
7. Acar, C., Dincer, I. & Naterer, G. F. Review of photocatalytic water-splitting methods for sustainable hydrogen production. *Int. J. Energy Res.* **40**, 1449–1473 (2016).
8. Yu, P. *et al.* Earth abundant materials beyond transition metal dichalcogenides: A focus on electrocatalyzing hydrogen evolution reaction. *Nano Energy* **58**, 244–276 (2019).
9. Wei, J. *et al.* Heterostructured Electrocatalysts for Hydrogen Evolution Reaction Under Alkaline Conditions. *Nano-Micro Lett.* **10**, (2018).
10. Kuang, Y. *et al.* Solar-driven, highly sustained splitting of seawater into hydrogen and oxygen fuels. *Proc. Natl. Acad. Sci.* **116**, 6624–6629 (2019).
11. Sheng, W., Gasteiger, H. A. & Shao-Horn, Y. Hydrogen Oxidation and Evolution Reaction Kinetics on Platinum: Acid vs Alkaline Electrolytes. *J. Electrochem. Soc.* **157**, B1529 (2010).
12. Danilovic, N., Subbaraman, R., Strmcnik, D., Stamenkovic, V. & Markovic, N. Electrocatalysis of the HER in acid and alkaline media. *J. Serbian Chem. Soc.* **78**, 2007–2015 (2013).
13. Greeley, J., Jaramillo, T. F., Bonde, J., Chorkendorff, I. & Nørskov, J. K. Computational high-throughput screening of electrocatalytic materials for hydrogen evolution. *Nat. Mater.* **5**, 909–913 (2006).
14. The tension of metallic films deposited by electrolysis. *Proc. R. Soc. London. Ser. A* **82**, 172–175 (1909).
15. Devanathan, M. A. V. & Selvaratnam, M. Mechanism of the hydrogen-evolution reaction on nickel in alkaline solutions by the determination of the degree of coverage. *Trans. Faraday Soc.* **56**, 1820 (1960).
16. Kreysa, G., Hakansson, B. & Ekdunge, P. Kinetic and thermodynamic analysis of

hydrogen evolution at nickel electrodes. *Electrochim. Acta* **33**, 1351–1357 (1988).

17. Diard, J.-P., LeGorrec, B. & Maximovitch, S. Etude de l'activation du degagement d'hydrogene sur electrode d'oxyde de nickel par spectroscopie d'impedance. *Electrochim. Acta* **35**, 1099–1108 (1990).

18. Krstajić, N., Popović, M., Grgur, B., Vojnović, M. & Šepa, D. On the kinetics of the hydrogen evolution reaction on nickel in alkaline solution. *J. Electroanal. Chem.* **512**, 16–26 (2001).

19. Sahiner, N., Ozay, H., Ozay, O. & Aktas, N. New catalytic route: Hydrogels as templates and reactors for in situ Ni nanoparticle synthesis and usage in the reduction of 2- and 4-nitrophenols. *Appl. Catal. A Gen.* **385**, 201–207 (2010).

20. Wu, S.-H. & Chen, D.-H. Synthesis and characterization of nickel nanoparticles by hydrazine reduction in ethylene glycol. *J. Colloid Interface Sci.* **259**, 282–286 (2003).

21. Chen, D.-H. & Wu, S.-H. Synthesis of Nickel Nanoparticles in Water-in-Oil Microemulsions. *Chem. Mater.* **12**, 1354–1360 (2000).

22. Dikusar, A. I., Globa, P. G., Belevskii, S. S. & Sidel'nikova, S. P. On limiting rate of dimensional electrodeposition at meso- and nanomaterial manufacturing by template synthesis. *Surf. Eng. Appl. Electrochem.* **45**, 171–179 (2009).

23. Furneaux, R. C., Rigby, W. R. & Davidson, A. P. The formation of controlled-porosity membranes from anodically oxidized aluminium. *Nature* **337**, 147–149 (1989).

24. Islam, A. & Islam, S. Electro-deposition Method for Platinum Nanoparticles Synthesis. *Eng. Int.* **1**, 9–17 (2013).

25. Turkevich, J., Stevenson, P. C. & Hillier, J. A study of the nucleation and growth processes in the synthesis of colloidal gold. *Discuss. Faraday Soc.* **11**, 55–75 (1951).

26. Malassis, L. *et al.* One-step green synthesis of gold and silver nanoparticles with ascorbic acid and their versatile surface post-functionalization. *RSC Adv.* **6**, 33092–33100 (2016).

27. Rambukwella, M. *et al.* Ligand structure determines nanoparticles' atomic structure, metal-ligand interface and properties. *Front. Chem.* **6**, (2018).

28. Zhuang, Z. *et al.* Nickel supported on nitrogen-doped carbon nanotubes as hydrogen oxidation reaction catalyst in alkaline electrolyte. *Nat. Commun.* **7**, 10141 (2016).

29. Ju, J. & Chen, W. In Situ Growth of Surfactant-Free Gold Nanoparticles on Nitrogen-Doped Graphene Quantum Dots for Electrochemical Detection of Hydrogen Peroxide in Biological Environments. *Anal. Chem.* **87**, 1903–1910 (2015).

30. Pendashteh, A., Palma, J., Anderson, M. & Marcilla, R. NiCoMnO4 nanoparticles on N-doped graphene: Highly efficient bifunctional electrocatalyst for oxygen reduction/evolution reactions. *Appl. Catal. B Environ.* **201**, 241–252 (2017).

31. Zhang, H. *et al.* NiCo2O4/N-doped graphene as an advanced electrocatalyst for oxygen reduction reaction. *J. Power Sources* **280**, 640–648 (2015).

32. Madrid, E. *et al.* Triphasic Nature of Polymers of Intrinsic Microporosity Induces Storage and Catalysis Effects in Hydrogen and Oxygen Reactivity at Electrode Surfaces. *ChemElectroChem* **6**, 252–259 (2019).

33. Mahajan, A. *et al.* Polymer of Intrinsic Microporosity (PIM-7) Coating Affects Triphasic Palladium Electrocatalysis. *ChemElectroChem* **6**, 4307–4317 (2019).

34. Marken, F., Madrid, E., Zhao, Y., Carta, M. & McKeown, N. B. Polymers of Intrinsic Microporosity in Triphasic Electrochemistry: Perspectives. *ChemElectroChem* **6**, 4332–4342 (2019).

35. Madrid, E. & McKeown, N. B. Innovative methods in electrochemistry based on polymers of intrinsic microporosity. *Curr. Opin. Electrochem.* **10**, 61–66 (2018).

36. Budd, P. M. *et al.* Polymers of intrinsic microporosity (PIMs): robust, solution-processable, organic nanoporous materials. *Chem. Commun.* 230 (2004) doi:10.1039/b311764b.

37. Madrid, E. *et al.* Metastable Ionic Diodes Derived from an Amine-Based Polymer of Intrinsic Microporosity. *Angew. Chemie Int. Ed.* **53**, 10751–10754 (2014).

38. Rong, Y. *et al.* pH-induced reversal of ionic diode polarity in 300nm thin membranes based on a polymer of intrinsic microporosity. *Electrochem. commun.* **69**, 41–45 (2016).

39. Ahn, S. D. *et al.* Polymer of Intrinsic Microporosity Induces Host-Guest Substrate Selectivity in Heterogeneous 4-Benzoyloxy-TEMPO-Catalysed Alcohol Oxidations. *Electrocatalysis* **7**, 70–78 (2016).

40. Zhao, Y. *et al.* Photoelectrochemistry of immobilised Pt@g-C3N4 mediated by hydrogen and enhanced by a polymer of intrinsic microporosity PIM-1. *Electrochem. commun.* **103**, 1–6 (2019).

41. Bonso, J. S., Kalaw, G. D. & Ferraris, J. P. High surface area carbon nanofibers derived from electrospun PIM-1 for energy storage applications. *J. Mater. Chem. A* **2**, 418–424 (2014).

42. Yang, Q. *et al.* PIM-1 as an artificial solid electrolyte interphase for stable lithium metal anode in high-performance batteries. *J. Energy Chem.* **42**, 83–90 (2020).

43. Li, C. *et al.* Polysulfide-Blocking Microporous Polymer Membrane Tailored for Hybrid Li-Sulfur Flow Batteries. *Nano Lett.* **15**, 5724–5729 (2015).

44. Gigli, M. *et al.* Investigating the factors that influence resistance rise of PIM-1 membranes in nonaqueous electrolytes. *Electrochem. commun.* **107**, 106530 (2019).

45. Ramimoghadam, D., Boyd, S. E., Brown, C. L., Mac A. Gray, E. & Webb, C. J. The Effect of Thermal Treatment on the Hydrogen-Storage Properties of PIM-1. *ChemPhysChem* **20**, 1613–1623 (2019).

46. Low, Z.-X., Budd, P. M., McKeown, N. B. & Patterson, D. A. Gas Permeation Properties, Physical Aging, and Its Mitigation in High Free Volume Glassy Polymers. *Chem. Rev.* **118**, 5871–5911 (2018).

47. Chua, C. K. & Pumera, M. The reduction of graphene oxide with hydrazine: elucidating its reductive capability based on a reaction-model approach. *Chem. Commun.* **52**, 72–75 (2016).

48. Park, S. *et al.* Chemical structures of hydrazine-treated graphene oxide and generation of aromatic nitrogen doping. *Nat. Commun.* **3**, 638 (2012).

49. Budd, P. M. *et al.* Solution-Processed, Organophilic Membrane Derived from a Polymer of Intrinsic Microporosity. *Adv. Mater.* **16**, 456–459 (2004).

50. Heuchel, M., Fritsch, D., Budd, P. M., McKeown, N. B. & Hofmann, D. Atomistic packing model and free volume distribution of a polymer with intrinsic microporosity (PIM-1). *J. Memb. Sci.* **318**, 84–99 (2008).

51. Olah, G. A. Beyond Oil and Gas: The Methanol Economy. *Angew. Chemie Int. Ed.* **44**, 2636–2639 (2005).

52. LeSuer, R. J. & Geiger, W. E. Approaches to analytical and synthetic electrochemistry in fluorous solvent-containing media. *J. Electroanal. Chem.* **594**, 20–26 (2006).

53. Whipple, D. T. & Kenis, P. J. A. Prospects of CO 2 Utilization via Direct Heterogeneous Electrochemical Reduction. *J. Phys. Chem. Lett.* **1**, 3451–3458 (2010).

54. Hori, Y., Murata, A. & Takahashi, R. Formation of hydrocarbons in the electrochemical reduction of carbon dioxide at a copper electrode in aqueous solution. *J. Chem. Soc. Faraday Trans. 1 Phys. Chem. Condens. Phases* **85**, 2309 (1989).

55. Jeon, H. S. *et al.* Operando insight into the correlation between the structure and composition of CuZn nanoparticles and their selectivity for the electrochemical CO2 reduction. *J. Am. Chem. Soc.* **141**, 19879–19887 (2020).

56. Mistry, H. *et al.* Highly selective plasma-activated copper catalysts for carbon dioxide reduction to ethylene. *Nat. Commun.* **7**, 12945 (2016).

57. Loiudice, A. *et al.* Tailoring Copper Nanocrystals towards C 2 Products in Electrochemical CO 2 Reduction. *Angew. Chemie Int. Ed.* **55**, 5789–5792 (2016).

58. Jeon, H. S., Kunze, S., Scholten, F. & Roldan Cuenya, B. Prism-Shaped Cu Nanocatalysts for Electrochemical CO 2 Reduction to Ethylene. *ACS Catal.* **8**, 531–535 (2018).

59. Li, Y. *et al.* Structure-Sensitive CO 2 Electroreduction to Hydrocarbons on Ultrathin 5-fold Twinned Copper Nanowires. *Nano Lett.* **17**, 1312–1317 (2017).

60. Raciti, D., Livi, K. J. & Wang, C. Highly Dense Cu Nanowires for Low-Overpotential CO 2 Reduction. *Nano Lett.* **15**, 6829–6835 (2015).

61. Saberi Safaei, T. *et al.* High-Density Nanosharp Microstructures Enable Efficient CO 2 Electroreduction. *Nano Lett.* **16**, 7224–7228 (2016).

62. Gao, D., Arán-Ais, R. M., Jeon, H. S. & Roldan Cuenya, B. Rational catalyst and electrolyte design for CO2 electroreduction towards multicarbon products. *Nat. Catal.* **2**, 198–210 (2019).

63. Gattrell, M., Gupta, N. & Co, A. A review of the aqueous electrochemical reduction of CO2 to hydrocarbons at copper. *J. Electroanal. Chem.* **594**, 1–19 (2006).

64. Jaikumar, A., Santhanam, K. S. V., Kandlikar, S. G., Raya, I. B. P. & Raghupathi, P. Electrochemical Deposition of Copper on Graphene with High Heat Transfer Coefficient. *ECS Trans.* **66**, 55–64 (2015).

65. Mistry, H., Varela, A. S., Kühl, S., Strasser, P. & Cuenya, B. R. Nanostructured

electrocatalysts with tunable activity and selectivity. *Nat. Rev. Mater.* **1**, 16009 (2016).

66. Ribeiro, A. C. F. *et al.* Diffusion Coefficients of Copper Chloride in Aqueous Solutions at 298.15 K and 310.15 K. *J. Chem. Eng. Data* **50**, 1986–1990 (2005).

67. SATO, H., YUI, M. & YOSHIKAWA, H. Ionic Diffusion Coefficients of Cs + , Pb 2+ , Sm 3+ , Ni 2+ , SeO 2- 4 and TcO − 4 in Free Water Determined from Conductivity Measurements. *J. Nucl. Sci. Technol.* **33**, 950–955 (1996).

68. Yin, G. *et al.* Selective electro- or photo-reduction of carbon dioxide to formic acid using a Cu–Zn alloy catalyst. *J. Mater. Chem. A* **5**, 12113–12119 (2017).

69. Yin, G. *et al.* A Cu–Zn nanoparticle promoter for selective carbon dioxide reduction and its application in visible-light-active Z-scheme systems using water as an electron donor. *Chem. Commun.* **54**, 3947–3950 (2018).

70. Hu, H. *et al.* In-situ grown nanoporous Zn-Cu catalysts on brass foils for enhanced electrochemical reduction of carbon dioxide. *Appl. Surf. Sci.* **445**, 281–286 (2018).

71. Keerthiga, G. & Chetty, R. Electrochemical Reduction of Carbon Dioxide on Zinc-Modified Copper Electrodes. *J. Electrochem. Soc.* **164**, H164–H169 (2017).

72. Ren, D., Ang, B. S.-H. & Yeo, B. S. Tuning the Selectivity of Carbon Dioxide Electroreduction toward Ethanol on Oxide-Derived Cu x Zn Catalysts. *ACS Catal.* **6**, 8239–8247 (2016).

73. Feng, Y. *et al.* Laser-Prepared CuZn Alloy Catalyst for Selective Electrochemical Reduction of CO 2 to Ethylene. *Langmuir* **34**, 13544–13549 (2018).

Chapter III

Molecular Catalysts for Electrochemical CO_2 Reduction in Alkaline Media

Introduction to CO_2 Reduction Reaction

The CO_2 reduction reaction (CO_2RR) is being considered a two-way strategy for both environmental remediation and a carbon-zero circular economy. The potential for CO_2 reduction is in front of us every day: nature builds complex molecules from atmosphere CO_2 and it is actually the main way energy is introduced in the biosphere. Scientists have always been teased by the idea of using CO_2 from the atmosphere as carbon feedstock for the industries of transport fuels and complex molecules. By using renewable energy for driving the reaction, fuel produced this way would have a net zero impact on the CO_2 concentration in the atmosphere once burned and chemical reagents would have a subtractive effect by locking carbon in whatever product those will be used in. Chemists have tried for decades to reproduce with artificial systems what nature does in obtaining valuable fuel or a chemical building block. Over the past two decades CO_2RR has evolved into its own major research field. If an efficient, resilient and selective CO_2RR system will be developed, conversion of CO_2 will not be a way of mitigate the effects of greenhouse gases, but an integral part in the development of a sustainable society.

Direct outer sphere reaction of CO_2 on a non-catalytic electrode surface involve the initial formation of the highly energetic CO_2 anion radical. The standard potential of the $CO_2/CO_2^{\bullet-}$ couple is as negative as −1.97 V vs. SHE in an aprotic solvent like N,N′-dimethylformamide (DMF),[1] and −1.90 V in water.[2] Catalytic strategies have thus been developed to avoid the intermediacy of the CO_2 anion radical for obtaining the various products one may expect from the electrochemical reduction of CO_2 at lesser energetic costs. Mercury and lead are the best approximation of electrode materials that do not interfere in the chemistry of CO_2 reduction leading to a complete outer shell reaction. In DMF at very negative potentials CO_2 reduction produces three species: carbon monoxide, oxalate and formate, with a quantitative global faradaic yield.[1] They are the results of the homogeneous chemistry of $CO_2^{\bullet-}$ and the mechanism that lead to their formation are shown in Scheme 1. Dimerization, leading to oxalate, is a reaction of one-electron

stoichiometry derived by the radical character of $CO_2^{\bullet-}$. CO and carbonate result from $CO_2^{\bullet-}$ acting like a Lewis base and formate result by it acting like a Brønsted base, leading to a two-electron stoichiometry.

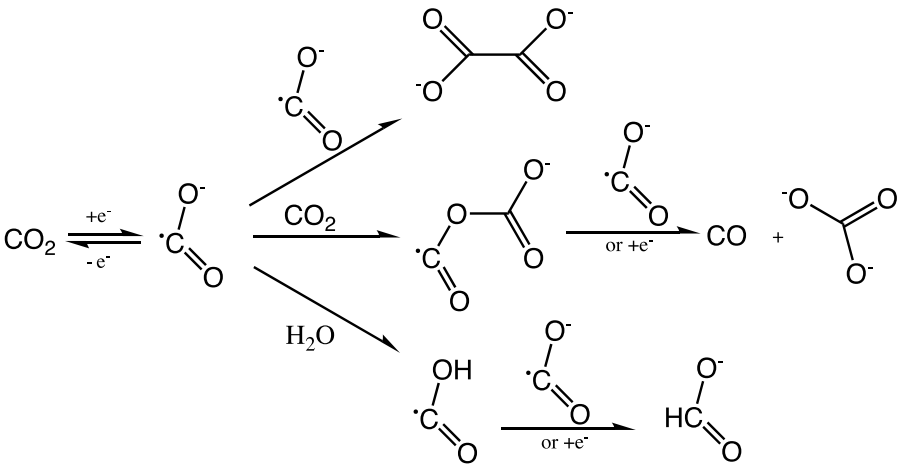

Scheme 1 Outer shell reaction mechanisms.

Homogeneous and heterogeneous catalysts both are being developed as strategies to obtain more efficient mechanisms; some examples of heterogeneous catalysts have already been discussed in the second chapter as copper alloys. Homogeneous catalysis has for the most part involved reduced states of transition metal complexes and many have been used for this purpose.

Metal Organic Molecules as Catalysts for CO_2RR

Catalysts for CO_2 reduction have been widely researched amongst the molecular metal-based systems as the transition metals generally have multiple redox states accessible that facilitate multielectron chemistry. The vast majority of these catalysts employ a single metal center,[3–9] usually Rhenium or Manganese. Albeit structurally similar, Re and Mn based catalysts show different electrochemical behavior. While rhenium complexes have been studied for longer time and historically thought to be the most efficient in CO_2RR, in a work by Chardon-Noblat, Deronzier and co-workers,[10] it was evidenced that Mn complexes (where Mn center is typically in the Mn(I) oxidation state) can act as a good CO_2 reduction catalysts as well. The complexes $[Mn(L_2)(CO)_3X]^n$ have become the focus of intense investigation in recent years as pre-catalysts for CO_2 reduction, in part due to

their high product selectivity for CO formation, but also because they are based on a cheaper and more earth-abundant metal, compared to their thoroughly investigated Re-based counterparts. These complexes present usually a bidentate ligand which is a polypyridyl species or a related (L_2) one, a monodentate neutral or anionic ligand like acetonitrile or Br^- (in the general formula represented by X if it is an halogen, more broadly by L) and three CO.

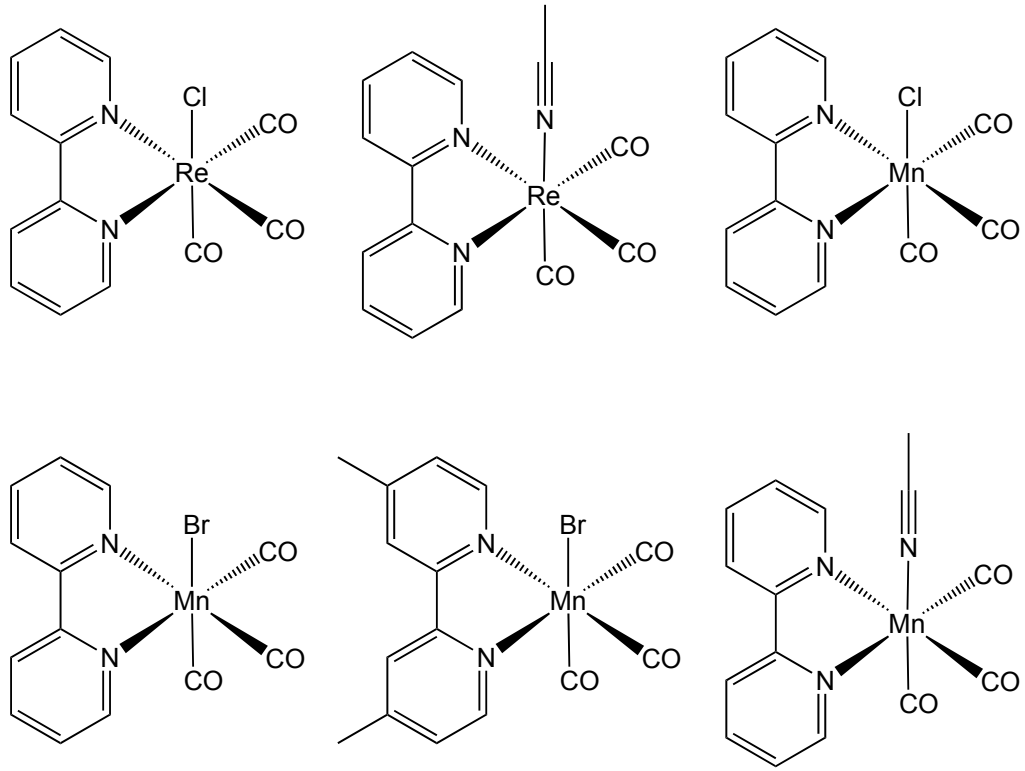

Scheme 2 Molecular structures of the most studied systems based on Re(I) and Mn(I). They share some basic elements such as the bidentate ligand, the three CO and a monodentate ligand with a general formula of $[M(L_2)(CO)_3L]^n$. [10–12]

The carbonyl species [Re(R-bpy)$(CO)_3$X] shows a reversible one-electron reduction bpy ligand-based at -1.4 V vs SCE, followed by a further irreversible one-electron reduction that involves the dissociation of the group X, thus opening the active site for CO_2RR at -1.76 V. The molecule CO_2 reacts slowly with the one-electron reduced species through an outer sphere mechanism consisting in a disproportionation reaction of the radical species $CO_2^{\bullet-}$:

$$2CO_2 + 2e^- = CO + CO_3^{2-} \quad (1)$$

On the other side, it is catalytically reduced at a much faster pathway with the two-electron reduced species:[13,14]

$$CO_2 + 2H^+ + 2e^- = CO + H_2O$$

(2)

In the case of the species [Mn(R-bpy)(CO)$_3$X], differently, the electrochemical behavior shows a one-electron reduction at -1.4 V, followed by a rapid loss of X providing the active species [Mn(R-bpy)(CO)$_3$]$^-$. The elimination of the monodentate ligand allows the active site to interact with CO_2 thus forming the Mn(I) metallocarboxylic acid intermediate as shown in Scheme 2 where all the pathways that may occur after the first and second reduction for both the systems are displayed.[15,16] The CO_2RR can then proceed through 2 routes: protonation first (preferred by Mn complexes) or reduction first (preferred by Re complexes).

Mechanistic studies of Rhenium-type catalysts have provided evidence for a concentration-dependent formation of dinuclear intermediates during catalysis.[14,17] Indeed, cofacial dinuclear Re complexes with rigid backbone structure, that prevents Re-Re bonding (which leads to the deactivation of carbon reduction catalysis), showed a beneficial interaction between the two reaction sites, clearly outperforming non-cofacial or mononuclear complexes at a double concentration[18].

This section will focus on the CO_2 reduction reaction catalyzed by two major types of systems: (i) complexes based on manganese (Mn) to explore the possible beneficial effects of a dinuclear geometry and (ii) systems containing rhenium (Re) inside nitrogen rich Covalent Organic Framework (COF). The latter have been synthetized from the reaction between melamine and 1,3,5-benzenetricarboxaldehy that has been demonstrated to have high efficient CO_2 capture capability.[19]

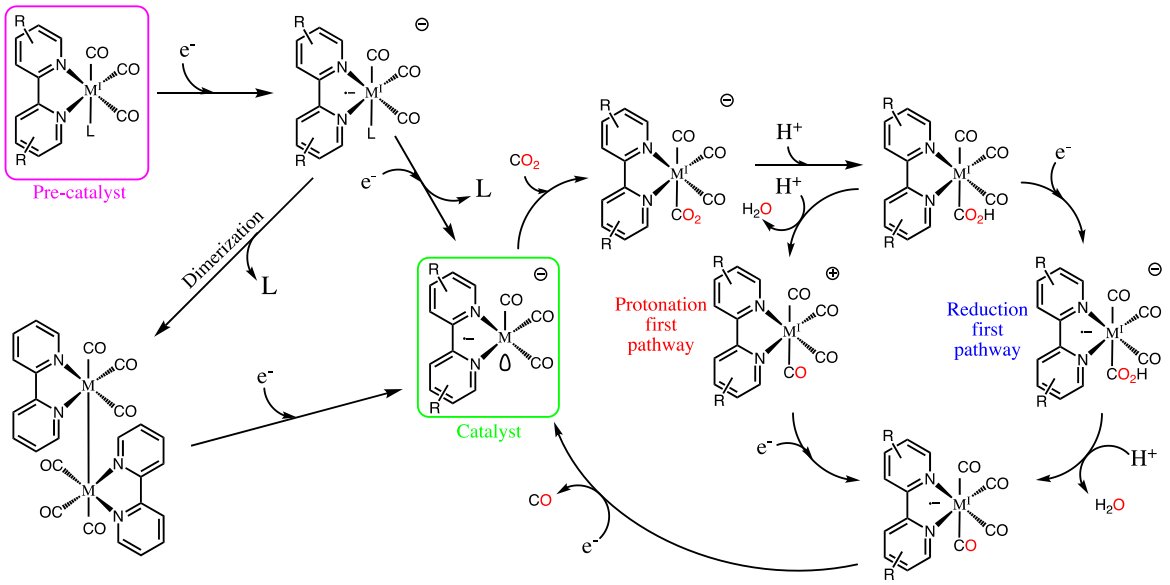

Scheme 3 Scheme showing activation, catalysis and side reactions of generic $[M(L_2)(CO)_3L]^n$ from computational and experimental investigations.[16]

Dinuclear Manganese Complexes and Others Materials

Synthesis of the complexes

The synthetic approaches, used for the synthesis of the manganese complexes here investigated, are depicted in Scheme 4. All the reactions and subsequent purification processes have been carried out in the darkest environment possible, due to the high photosensitivity of manganese complexes.

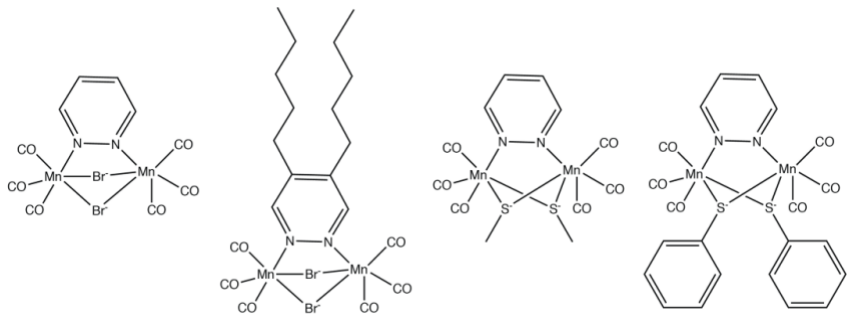

Scheme 4 Molecular structures of binuclear molecular systems investigated. Species EQ 1 and EQ 2 contain two halogens as bridge between the metal centers; EQ 3 and EQ 4 are complexes with sulfur as bridging ligand for the two metal centers by methylsulfane and phenylsulfane.

The $[Mn_2(\mu\text{-}Br)_2(CO)_6(\mu\text{-}pydz)]$ complexes were obtained by reacting equimolar amounts of pyridazine (EQ 1) or 4,5-bipentylpyridazine (EQ 2) and $Mn(CO)_5Br$ in toluene solution at 60 to 80 °C. The chalcogenide-bridged species EQ 3 and EQ 4 were instead obtained through the one-pot synthesis via "orthogonal bonding approach". Hence, two ligands were coordinate simultaneously and orthogonally (one axial and one equatorial) to a manganese binuclear skeleton, given by Mn_2CO_{10}. To avoid evaporation of the reagent the reaction is carried out in a sealed solvothermal bomb at 120°c in toluene solution.

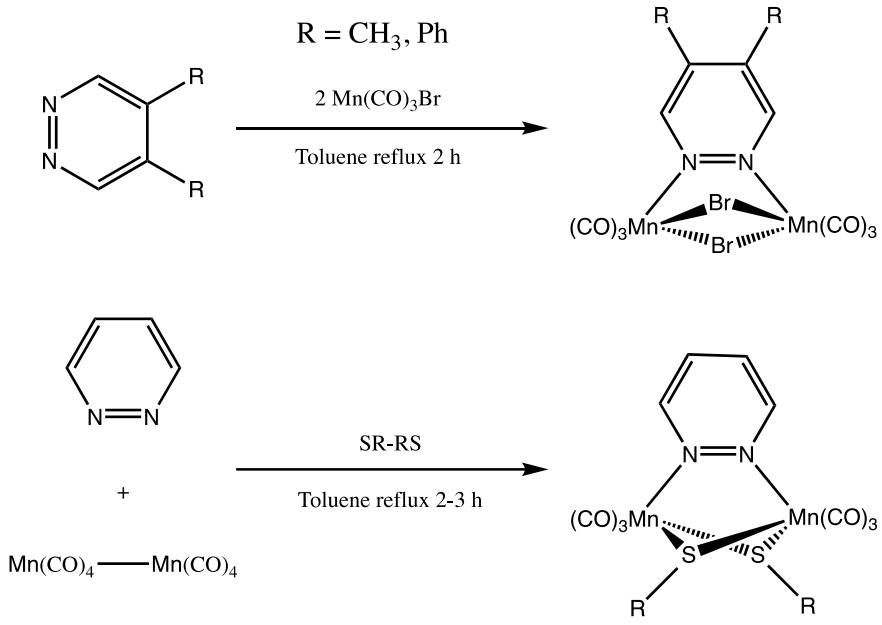

Scheme 5 Procedure for the synthesis of the dinuclear complexes here discussed.

Materials and General Experiments.

Tetrabutylammonium hexafluoro-phosphate (TBAH) 99.0% from Sigma-Aldrich was used as electrolyte, acetonitrile (ACN) 99.5% from Sigma-Aldrich and dimethyl formamide (DMF) 99.5% from Sigma-Aldrich as solvents. HCOOH/Na buffer solution prepared with formic acid and NaOH from Sigma-Aldrich. Electrochemical investigations by cyclic voltammetry (CV) were carried out using a BioLogic SP-300 instrument and a custom-made electrochemical cell. A 1 mm diameter GC disk was used as working electrode, the working electrode was polished with a 0.3 μm aluminum oxide (Buehler) slurry in distilled water on a felt pad. A Pt spiral wire acted as counter electrode and an Ag wire was used as pseudo reference electrode.

Results and Discussion

Dinuclear Manganese Complexes

EQ 1. The simplest Mn-based system, is the molecule here referred as EQ 1, which shows the reaction site free from functional groups. It was investigated in ACN/TBAH electrolyte solution as reported below in Figure 1. In Figure 1a the black line curve depicts the exploration of the wider potential window, having as vertex potentials +2.0 and -2.5 V. It shows a complex system of electron transfers. Nevertheless, successive scans at positive (red) and negative potentials (blue) were less defined. Especially when the potential is scanned at positive values, the molecule seamed to undergo some kind of degradation, filming the surface of the electrode and passivating it. For comparison purposes, the thin gray line represents a measurement of the background electrolyte solution. No reduction was appreciable when CO_2 was introduced (Figure 1b) and peak number and positions were not reproducible; these facts led us to hypothesize that this species is not enough stable in ACN solvent when it undergoes electron transfer processes. One possible explanation of this instability could be ACN acting as monodentate ligand by coordinating the nitrogen to the metal center. The catalyst active species is therefore vulnerable to attack by a solvent molecule.[10]

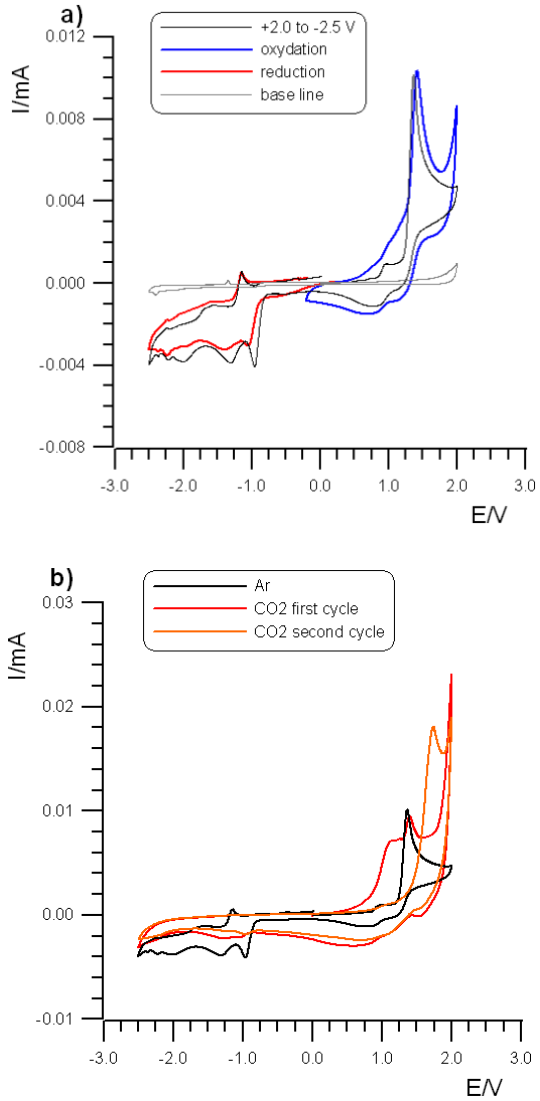

Figure 1 Electrochemical characterization of EQ 1 in ACN 0.67 mM trough CV. Sample behavior in Ar atmosphere in both reducing and oxidizing potentials (a), activity in CO_2 atmosphere and rapid degradation (b). WE: GC (7.85×10^{-3} cm^2); RE: Ag; scan rate: 0.2 V/s; T = 298K.

The species EQ 1 was also tested in PBS (pH 7) as heterogenous catalyst by preparing an ACN solution 1 g/L and drop casting 40 µL on to the GC electrode but no electrochemical activity was registered in both argon and carbon dioxide (Figure 2).

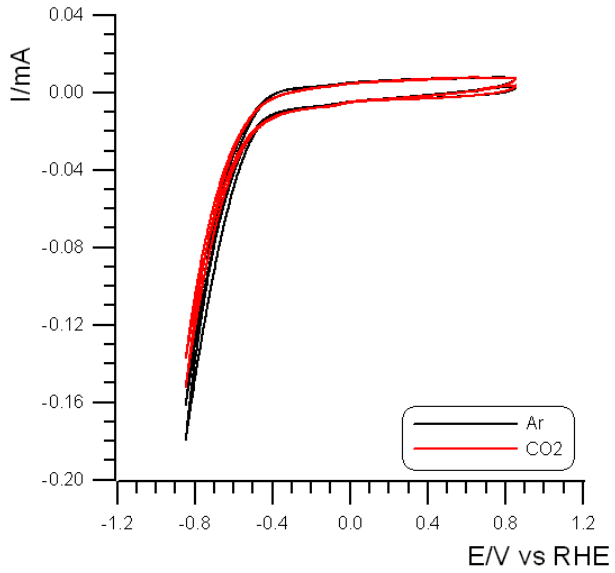

Figure 2 Electrochemical characterization of EQ 1 as heterogeneous catalyst in 0.1 M PBS. 40 μg of material was dropcasted on to the electrode surface. WE: GC (0.07 cm^2); RE: SCE; scan rate: 0,005 V/s; T = 298K.

EQ 2. The complex labeled as EQ 2 represents a small variation of the previous one EQ 1. An ACN solution of 0.8 mM was prepared using TBAH as supporting electrolyte. Figure 3a shows another complex peaks system rapidly losing definition with the introduction of CO_2 and passivating the electrode surface. This is better shown in Figure 3b, as it is evident the extent of the passivation after just eight cycles (red line).

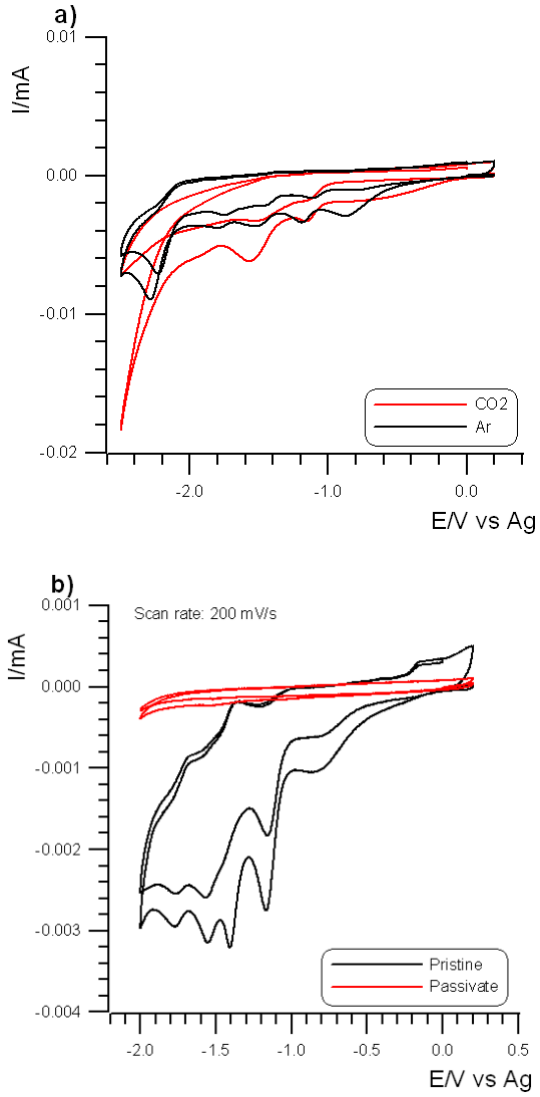

Figure 3 Electrochemical characterization of EQ 2 in ACN 0.76 mM trough CV. (a) Sample behavior in Ar (black) and CO_2 (red) atmosphere. (b) Molecule breaking down and passivating the WE First 2 cycles (black) vs 7° and 8° cycles (red). WE: GC (7.85×10^{-3} cm^2); RE: Ag; scan rate: 0.4 V/s; T = 298K.

EQ 3. EQ 3 and EQ 4 present sulfur bridges in the molecular structure that connect the metallic centers. This time a DMF 2.0 mM solution was prepared. Clear and reproducible results displayed two reduction processes at E = -1.0 V (one-electron process) and at E = -2.3 V (two-electron) in Ar atmosphere (Figure 4). The first reduction is completely reversible while the second one appears as completely irreversible giving rise to a series of three additional anodic processes at E = -1.5 V, -0.9 V, -0.4 V, suggesting a complicated reactivity of the molecule happening with the second process.

By saturating the solution with CO_2, an increase in current at E = -2.0 V is obtained, linked to the successful carbon dioxide reduction. This new current wave partially overlaps with

the two-electron process at E = -2.3 V but the complete absence of the three oxidations suggests the new process completely overturns the previously detected one.

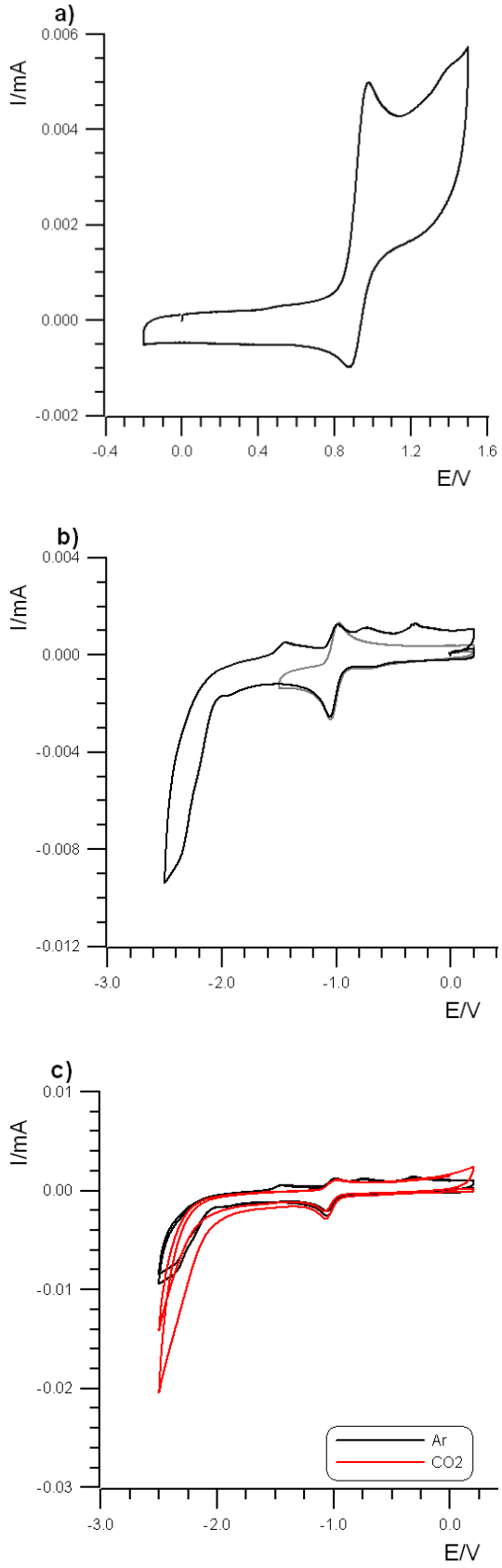

Figure 4 Electrochemical characterization of EQ 3 in DMF 2.02 mM trough CV. Cathodic scan (a) and anodic scan (b) in Ar atmosphere. Comparison between sample behavior in Ar (black) and in CO_2 (red) atmosphere (c). WE: GC (7.85×10^{-3} cm^2); RE: Ag; scan rate: 0,4 V/s; T = 298K.

Voltammetric curves recorded at 0.4 V/s showed a rapid electrode passivation like the previous species. This indicate a labile nature of these systems. However, mononuclear complexes related to these species are reported as stable durable species; the phenomenon of electrode passivation occurring so rapidly in our measurements suggests that this is not the case for these dinuclear complexes. Cleaning the surface of the electrode with alumina powder recovered back the activity.

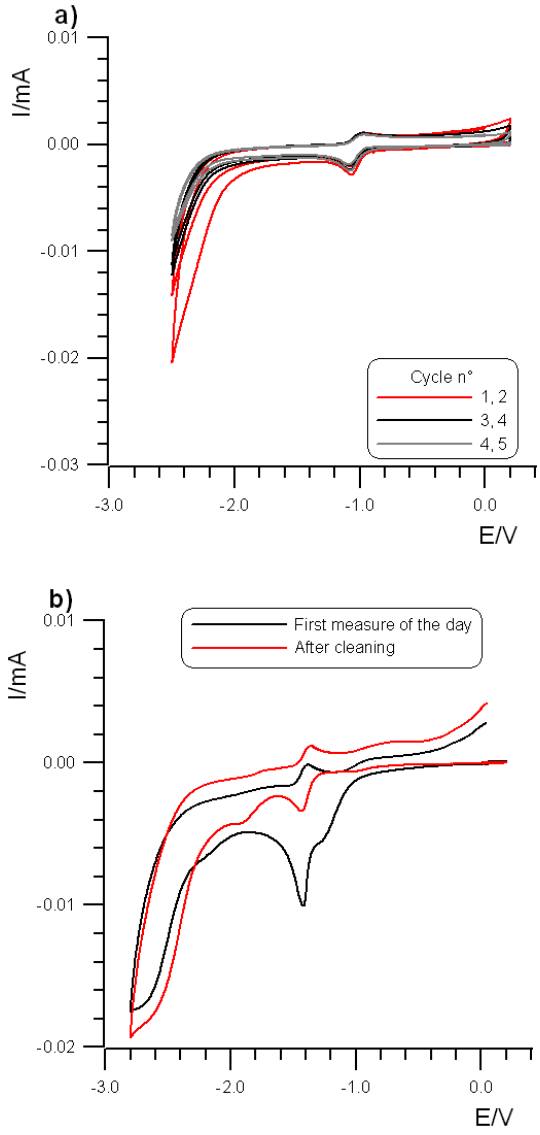

Figure 5 Electrochemical characterization of EQ 3. Evidence of sample activity loss in CO_2 (a) during the first (red), second (black) and third (gray) CV run in DMF. CO_2RR signal is recovered after electrode mechanical cleaning from an earlier experiment in ACN (b). WE: GC (7.85×10^{-3} cm^2); RE Ag; scan rate: 0.4 V/s; T = 298K.

To better understand the behavior seen in Ar saturated DMF electrolyte solution, simulations were performed to fit the experimental data (Figure 5). Experimental CVs

were run in a range of scan rates between 0.4 and 10.0 V/s. This is necessary to obtain a reliable fit: if the simulation parameters (kinetic constants, diffusion parameters, α values, etc.) fit well the experimental data in a two-order of magnitude of scan rates as in the case of Figure 6, then the mechanism hypothesized and the set of parameters used are acceptable.

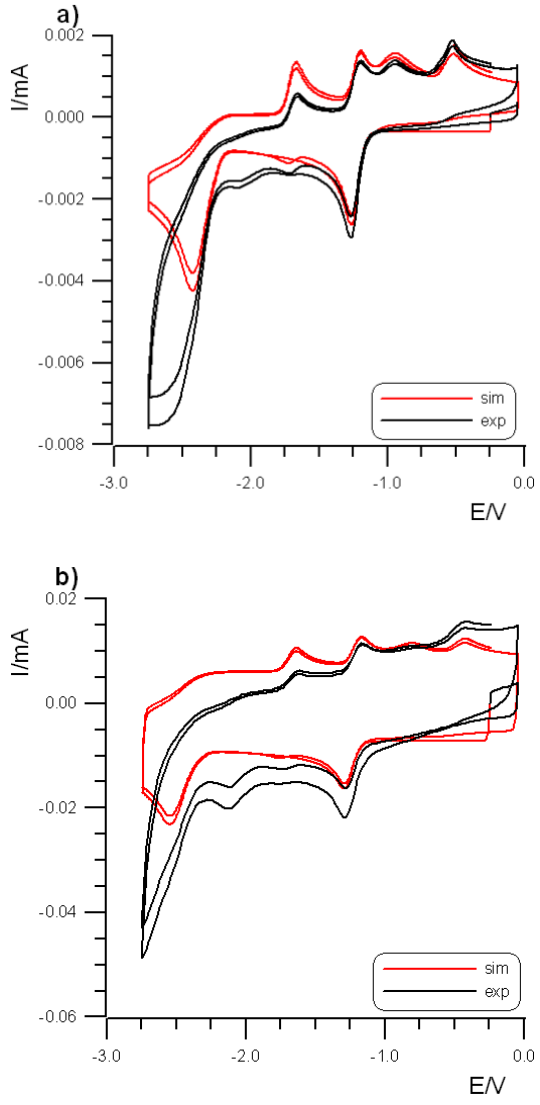

Figure 6 Simulations (by Antigona software) juxtaposed on the original experimental data of EQ 3. Simulations parameters fitted using experimental CVs with scan rate 0.4 V/s (a) and 10.0 V/s (b). Ar atmosphere, , TBAH/DMF electrolyte solution, GC as WE, T= 298 K.

The electrochemical mechanism that reasonably fits the experimental data is sketched below in Scheme 4; it shows a reversible one-electron process followed by an irreversible two-electron reduction, which can be considered as two closely-spaced one-electron

reductions. This second process leads to three different oxidations on the reverse scan back to the initial potential:

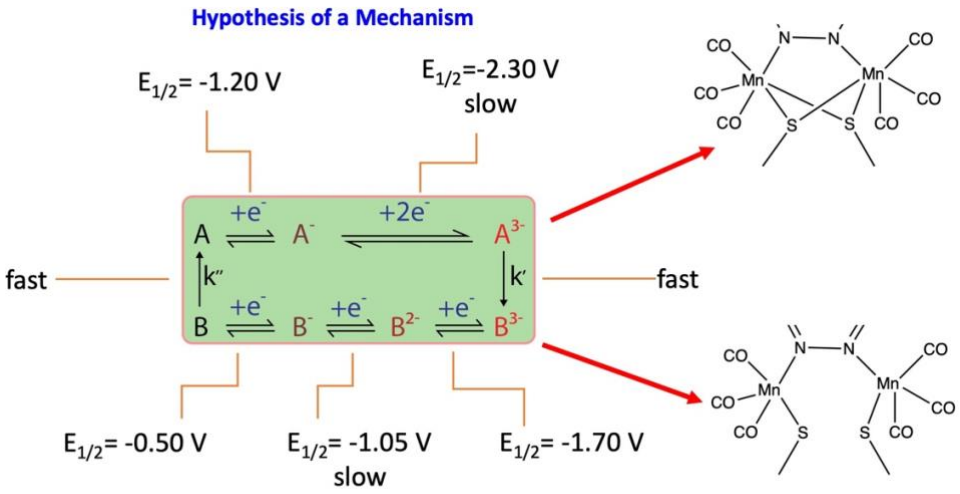

Scheme 6 Proposed Mechanism to rationalize the experimental data obtained from the CV investigation of EQ 3 in DMF solution. Double half arrows represent electron transfers and full arrows represent chemical reactions.

The reversible process, most probably attributed to the reduction of the aromatic ring, is an electron transfer that does not induce any bond breaking. The irreversibility of the second process indicates that the molecule is changing by a following up chemical reaction. It can be associated with the double reduction of the two metal centers and this has, most likely, a chemical consequence consisting in the breaking of the sulfur bridges linking the Mn. From the new formed isomeric structure, the re-oxidation to the original valence state is possible and the process is again irreversible because the electron transfers are affected by the chemical reaction. In fact, this last chemical process leads to re-establish the sulfur bridgings, thus originating a square-scheme mechanism as sketched in Scheme 4.

EQ 4. As a slight variation of EQ 3, a qualitative similar behavior was expected. Indeed, experiments in similar conditions delivered similar results and interaction with CO_2 as evidenced by comparing Figure 7 with the voltammetric pattern reported in Figure 4

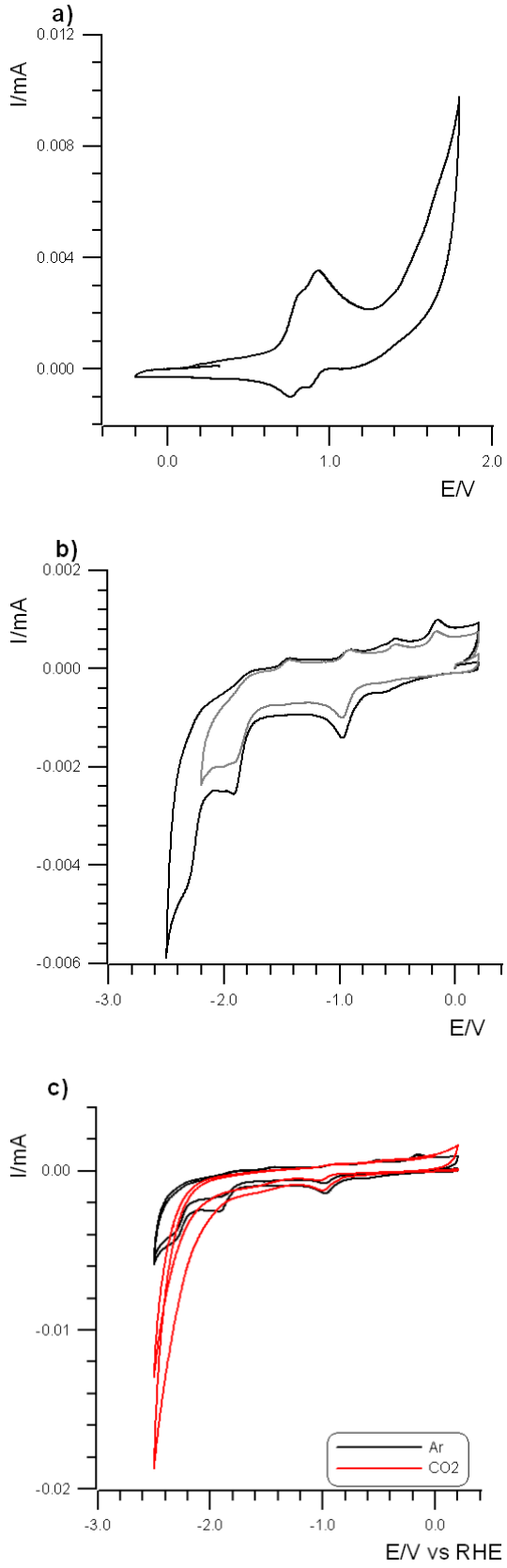

Figure 7 Electrochemical characterization of EQ 4 in DMF 0.29 mM trough CV. Cathodic scan (a) and anodic scan (b) in Ar atmosphere. Comparison between sample behavior in Ar (black) and in CO_2 (red) atmosphere (c). WE: GC (7.85×10^{-3} cm^2); RE: Ag; scan rate: 0.4 V/s; T = 298K. Potential corrected vs NHE using ferrocene.

In argon atmosphere the species EQ 4 presents peaks in the same potential window as for EQ 3 corresponding to the same processes but at slightly different energy values and current intensities. Most notably, the two-electron process seems splitted into two distinct peaks for EQ 4 and carbon reduction is much more prominent (Figure 8).

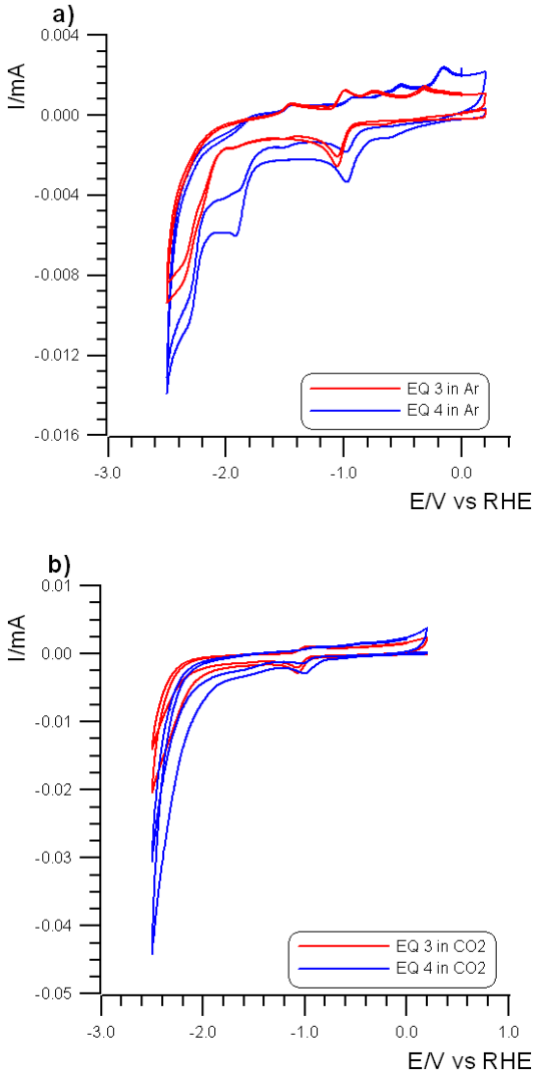

Figure 8 Comparison of the voltammetric behavior between EQ 3 0.7 mM and EQ 4 0.3 mM in TBAH/DMF electrolyte solution in the presence of Ar (a) and in CO_2 (b). WE: GC (7.85×10^{-3} cm^2); RE: Ag; scan rate: 0.4 V/s; T= 298K. For the species EQ 4 the current was multiplied by a factor of 2.36 to adjust the difference in concentration between the two complexes. Potential corrected vs NHE using ferrocene.

Light sensitivity and degradation

During characterization procedures the sample solutions were kept in a dark environment for the whole time as Mn complexes are extremely liable to photodegradation. To have an idea of how the data are impacted by degradation products and be able to isolate the out of

the signal, a Motic mlc-150c power lamp was turned on for brief time windows in between CV scans with a power of 000 W and a color temperature of 3200 K. The lamp was equipped with a optic fiber arm that was adjusted near the glass electrochemical cell to ensure an efficient light collection. After just few minutes voltammetric response was visibly changing (Figure 9).

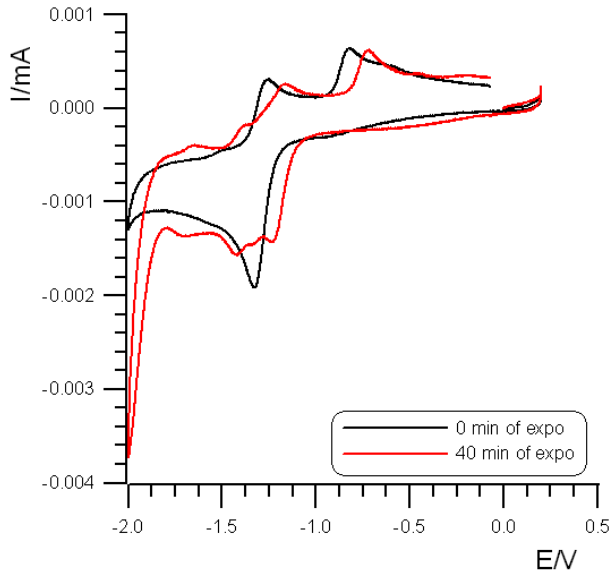

Figure 9 Electrochemical characterization of EQ 4 in ACN before (black) and after (red) 40 minutes of light exposure. Ar atmosphere; WE: GC (7.85×10^{-3} cm^2); RE: Ag; scan rate: 0.4 V/s; T= 298K.

TOF Analysis of EQ 3 and EQ 4

Reliable measurements showing clear CO_2RR occurred while characterizing EQ 3 and EQ 4 but, unfortunately, EQ 1 and EQ 2 did not deliver the same clarity and data gained so far only allowed for Turnover Frequency (TOF) calculations for 2 systems out of 4. By comparing peak current in presence of the substrate CO_2 (i_{cat}) and in its absence (i_p), is possible to calculate TOF for a homogeneous catalyst (in the case of a reversible electron-transfer reaction followed by a fast catalytic reaction) using equations:

$$i_{cat} = n_{cat}FA[cat](DK_{cat}[Q]^{y})^{1/2} \quad (3)$$

$$i_p = 0.4463n_p^{3/2}FA[cat]\left(\frac{F}{RT}\right)^{1/2}v^{1/2}D^{1/2} \quad (4)$$

$$TOF = k_{cat}[Q] \quad (5)$$

y is equal to 1 assuming a pseudo-first-order kinetics since the concentrations of the substrates Q, here CO_2, are large in comparison to the concentration of catalyst[20]. n_{cat} is the number of electrons required for the catalytic reaction (n_{cat} = 2 for the reduction of CO_2 to CO), F is Faraday's constant, A is the surface area of the electrode, [cat] is the catalyst concentration, D is the diffusion constant of the catalytically-active species, k_{cat} is the rate constant of the catalytic reaction, and [Q] is the substrate concentration. Equation 4 describes the peak current of a reversible electron transfer and with no following reaction[21]. R is the universal gas constant, T is temperature, n_p is the number of electrons in the reversible, non-catalytic reaction, and υ is scan rate (0.4 V/s). Dividing eq 3 by eq 4 allows for determination of i_{cat}/i_p and to further calculate the catalytic rate constant (k_{cat}) and the turnover frequency (TOF). Solving i_{cat}/i_p for $k_{cat}[Q]$ and combining with equation 5 you get:

$$TOF = k_{cat}[Q] = \frac{Fvn_p^3}{RT}\left(\frac{0.4463}{n_{cat}}\right)^2\left(\frac{i_{cat}}{i_p}\right) \tag{6}$$

In this equation, A cancels out because the same electrode was used for the experiments under CO_2 and Ar. D also cancels out because we are assuming that the diffusion constant of the catalytically-active species does not change significantly under CO_2 or Ar. Using experimental data from ACN solutions of EQ 3 and EQ 4 (Figure 10) TOF values were calculated with eq 6.

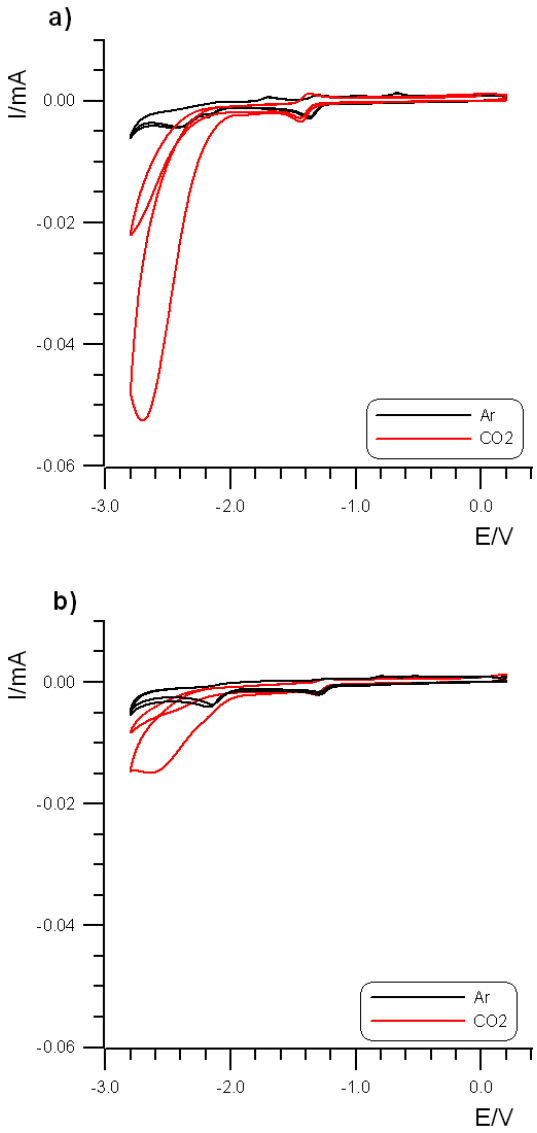

Figure 10 Comparison of the voltammetric behavior between EQ 3 0.9 mM (a) and EQ 4 0.3 mM (b) in TBAH/ACN. WE: GC (7.85×10^{-3} cm^2); RE: Ag; scan rate: 0.4 V/s; T= 298K.

Using the current peaks of the first CV cycle (to exclude electrode passivation as possible) TOF values are 114 s^{-1} for EQ 3 and 10 s^{-1} for EQ 4, much above the value reported by previous works on manganese-based systems of 7.2 s^{-1}.[15]

The order of magnitude of difference between the two systems can be proof of improved performance by dinuclear reaction site. In EQ 3 both Mn-S bonds cleavage take place almost simultaneously, this opens both the metal centers to interaction with CO_2. It is unlikely that two CO_2 molecules have enough room to interact independently with both nuclei, but, as previously discussed, a dinuclear reaction site can outperform two independent mononuclear ones, as demonstrated on Re-based systems.[18] In EQ 4, on the other hand, the two Mn-S bond cleavage are split in two processes far apart and the

CO_2RR peak takes place clearly when only the species with one metal center available for interacting with the substrate present in solution.

Metallorganic Rhenium Co-polymer

Metal and covalent organic frameworks (MOFs and COFs, respectively) represent a powerful technology for capture and sequestration of CO_2 gas, as these classes of coordination polymers, modular in character, match large porosities with surface areas and, mostly relevant, noticeable capability of CO_2 absorption and separation.[22–26] More recently, the preparation of transition metal COFs derivatives combining the properties of the two components has been explored, as the modular nature of these materials has facilitated the incorporation of known molecular catalysts through numerous available synthetic methods.[26,27] In this respect, the use of Re moieties in combination to a recently developed porous hyper crosslinked polymer with good CO_2 adsorption capabilities, seems to be attractive in view of the peculiar CO_2RR high activity of the metal.

The targeted covalent organic framework (COF) was synthesized using procedures described elsewhere[19,28] based on the condensation of melamine and benzene-1,3,5-tricarboxaldehyde under the solvothermal conditions, using dimethyl sulfoxide as a reaction medium. Part of the product material reacted with $Re(CO)_5Cl$ giving rise to powders constituted by new organometallic complex (ACM) while the rest was kept metal free.

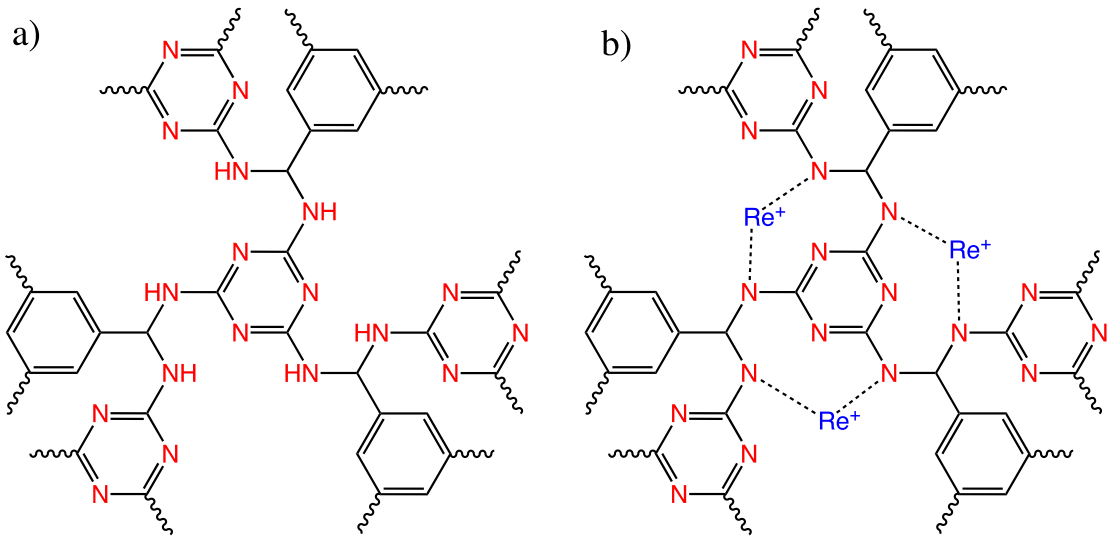

Scheme 7 Molecular structure of COF (a) and ACM (b) where Re+ represents the moiety $Re(CO)_3Cl$.

Rhenium complexed COF (ACM). The covalent organic framework (COF) material with Rhenium moieties (ACM) (see Scheme 7) was electrochemically checked for CO_2 reduction in dark environment. Its performances were investigated in two modalities: (i) as a drop-casted film on a 3 mm GC (0.07 cm^2) from an EtOH 1 g/L solution in a 0.2 M HCOOH/Na buffer solution (pH = 4) and (ii) in a DMF suspension 0.33 g/L using TBAH as electrolyte. In both cases control experiments using Rhenium-free COF were run in parallel. The polymer film was drop-casted in 8 aliquots 5 μL each following the same protocol consisting in a two-steps casting/drying procedure (dropping an aliquot on the electrode after the solvent was completely dried out for the previous deposition) until a total of 40 μg of material was reached.

ACM seams to express none or very low CO_2RR activity (Figure 11a); the current registered is not relatable to a reaction with CO_2 as it is not CO_2 concentration dependent. A similar phenomenon is observed also with the COF film (Figure 11c). The lack of variation by changing atmosphere composition evidences that this process is intrinsic of the materials and not a catalytic one. In Ar a progressive lowering of such process is probably due to degradation of the ACM and passivation of the electrode (Figure b).

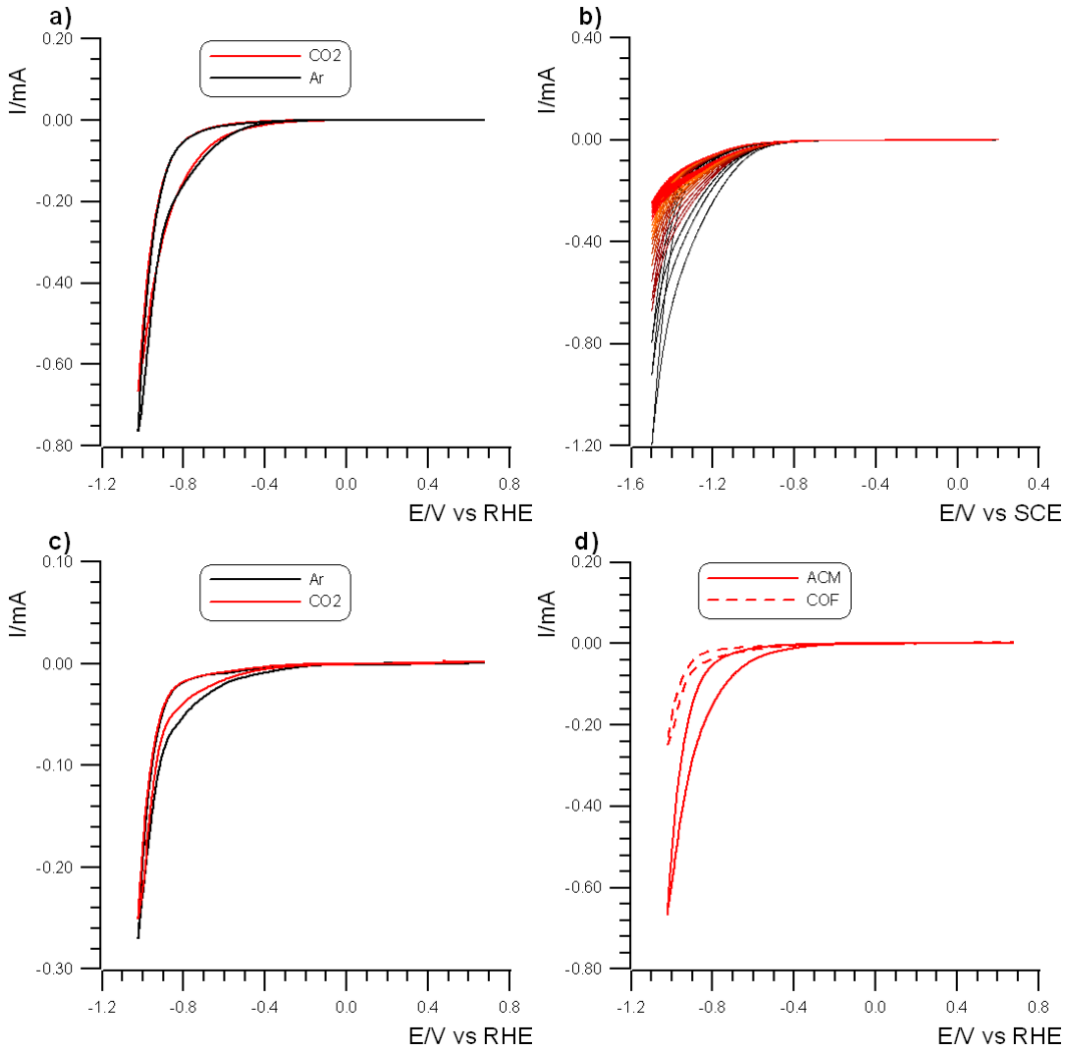

Figure 11 Electrochemical characterization of 40 µg ACM film in HCOOH/Na 0.2 M buffer solution (pH 4) in Ar and CO_2 atmosphere (a) and the irreversible modification of behavior from first cycle (black) to last (red) in Ar shown in progressive color shift (b). Control experiment using 40 µg COF film in the same conditions (c) and comparison between the two systems performing in CO_2 atmosphere (d). WE: GC (0.07 cm^2); RE: SCE; scan rate: 0,005 V/s; T = 298K.

Experiments run in DMF were conducted with the polymers in solution with concentrations (given in grams of material per Liter) of 0.33 g/L.

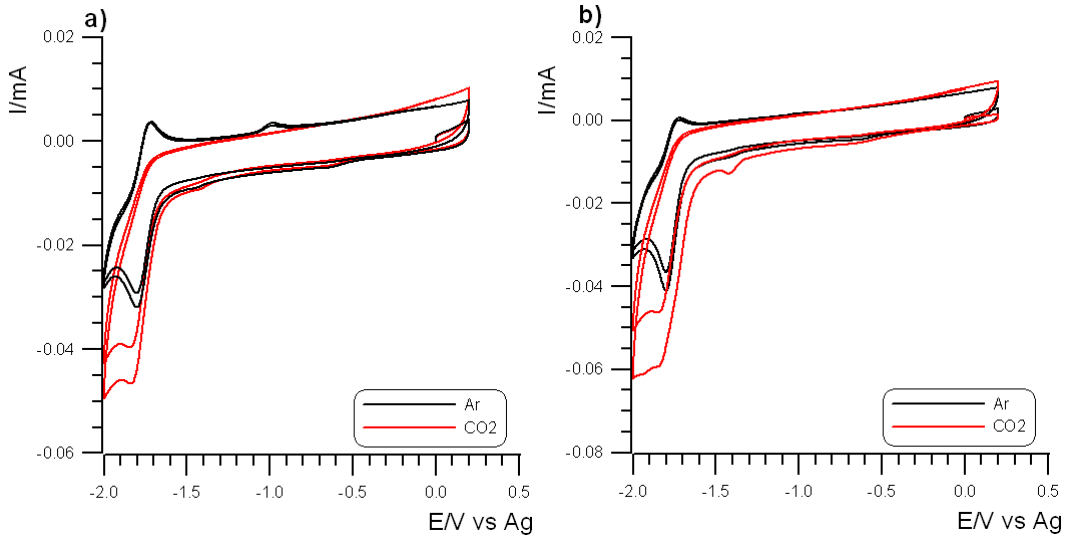

Figure 12 Electrochemical characterization of COF (a) and ACM (b) in dissolved in DMF (0.33 g/L) and Ar (black) and CO_2 (red) atmosphere. WE: GC (0.07 cm^2), RE: Ag, scan rate 0.4 V/s.

The COF exhibited a partially reversible process at E = -1.75 V vs Ag in DMF solvent and in Ar atmosphere, the same process is visible for ACM but significantly less reversible. It is reasonable to suppose that this electron transfer is associated with the presence of the ammine group and the loss in reversibility could be due to interaction with the metal ion of some nitrogen atoms. In presence of CO_2 atmosphere, the reversibility is completely lost for both samples. A small peak at -1.0 V is present on COF (Figure 13) and ACM and this is correlated to a second process at -2.2 V present on both samples (both samples have the -1.0 V process but in ACM is extremely week). Performig multiple cycles brings about to a substantial loss in activity of the -2.2 V wave without any consequence on the other processes.

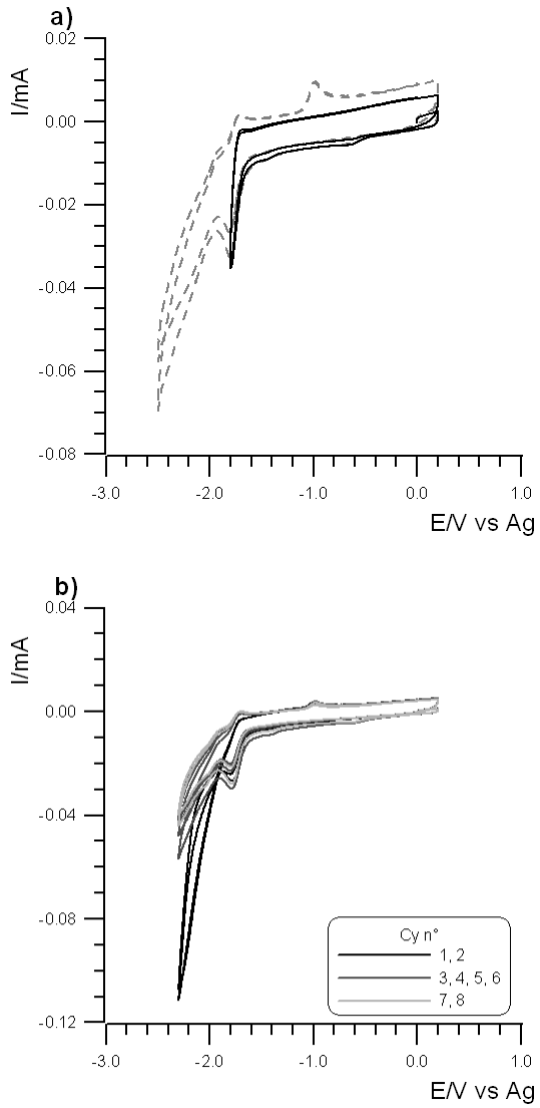

Figure 13 Relation between -2.2 V and -1.0 V peaks is showed here (a). Activity loss of -2.2 V process upon cycling (b). Solvent: DMF, WE: GC (0.07 cm^2), RE: Ag, scan rate 0.4 V/s.

Conclusions

We have described and characterized four molecular systems as homogeneous CO_2RR catalysts. The systems investigated are organometallic species represented by binuclear Mn complexes using different bridging ancillary ligands. The high photodegradation typical of this family of materials required the preparation and execution of the experiments to be done in the dark. Preliminary experiments were carried out in ACN but, possibly due to ligand-exchange reaction of solvent molecules in the complex, results obtained so far are quite tricky and not perfectly reproducible. Measurements in DMF were by far more useful. Species EQ 1 and EQ 2 containing two halogens as bridges showed to be labile molecules, especially in presence of CO_2, rapidly decomposing and passivating the electrodes. Complexes with sulfur as bridging ligand EQ 3 and EQ 4 were found to be much more stable and gave an impressive CO_2RR activity with TOF values of 114 s^{-1} for EQ 3 and 10 s^{-1} for EQ 4, much above the value reported by previous works on manganese-based systems of 7.2 s^{-1}.[15] The order of magnitude between the two values from systems very similar can give an interesting insight to the mechanism taking place at the reaction site. The reaction site for CO_2RR is formed when the bond with the bridging ligand is cleaved so that the CO_2 molecule can access the metal center. Catalytic activity in EQ 4 took place only when one metal center is available for interaction, preventing the improved performance by binuclear reaction site.

Then we studied the CO_2RR efficiency of a heterogeneous system consisting in a covalent organic framework (COF) functionalized with Re moieties (ACM). The two materials were reported to adsorb a significant amount of CO_2. Thus, its electrocatalytic performances were investigated both as a drop-casted film on a 3 mm GC in a 0.2 M HCOOH/Na buffer solution (pH = 4) and as a DMF suspension 0.33 g/L using TBAH as electrolyte. In both cases control experiments using Rhenium-free COF were run in parallel. ACM and COF did not show significant differences in behavior and little to no response toward CO_2 presence were detected when drop-casted.

References

1. Lamy, E., Nadjo, L. & Saveant, J. M. Standard potential and kinetic parameters of the electrochemical reduction of carbon dioxide in dimethylformamide. *J. Electroanal. Chem. Interfacial Electrochem.* **78**, 403–407 (1977).

2. Schwarz, H. A. & Dodson, R. W. Reduction potentials of CO2- and the alcohol radicals. *J. Phys. Chem.* **93**, 409–414 (1989).

3. Benson, E. E., Kubiak, C. P., Sathrum, A. J. & Smieja, J. M. Electrocatalytic and homogeneous approaches to conversion of CO 2 to liquid fuels. *Chem. Soc. Rev.* **38**, 89–99 (2009).

4. Yui, T., Tamaki, Y., Sekizawa, K. & Ishitani, O. Photocatalytic Reduction of CO2: From Molecules to Semiconductors. in 151–184 (2011). doi:10.1007/128_2011_139.

5. Finn, C., Schnittger, S., Yellowlees, L. J. & Love, J. B. Molecular approaches to the electrochemical reduction of carbon dioxide. *Chem. Commun.* **48**, 1392–1399 (2012).

6. Appel, A. M. *et al.* Frontiers, Opportunities, and Challenges in Biochemical and Chemical Catalysis of CO 2 Fixation. *Chem. Rev.* **113**, 6621–6658 (2013).

7. Kang, P., Chen, Z., Brookhart, M. & Meyer, T. J. Electrocatalytic Reduction of Carbon Dioxide: Let the Molecules Do the Work. *Top. Catal.* **58**, 30–45 (2015).

8. Takeda, H., Cometto, C., Ishitani, O. & Robert, M. Electrons, Photons, Protons and Earth-Abundant Metal Complexes for Molecular Catalysis of CO 2 Reduction. *ACS Catal.* **7**, 70–88 (2017).

9. Francke, R., Schille, B. & Roemelt, M. Homogeneously Catalyzed Electroreduction of Carbon Dioxide—Methods, Mechanisms, and Catalysts. *Chem. Rev.* **118**, 4631–4701 (2018).

10. Bourrez, M., Molton, F., Chardon-Noblat, S. & Deronzier, A. [Mn(bipyridyl)(CO)3Br]: An Abundant Metal Carbonyl Complex as Efficient Electrocatalyst for CO2 Reduction. *Angew. Chemie Int. Ed.* **50**, 9903–9906 (2011).

11. Hawecker, J., Lehn, J.-M. & Ziessel, R. Efficient photochemical reduction of CO 2

to CO by visible light irradiation of systems containing Re(bipy)(CO) 3 X or Ru(bipy) 3 2+ –Co 2+ combinations as homogeneous catalysts. *J. Chem. Soc., Chem. Commun.* 536–538 (1983) doi:10.1039/C39830000536.

12. Hartl, F., Rossenaar, B. D., Stor, G. J. & Stufkens, D. J. Role of an electron-transfer chain reaction in the unusual photochemical formation of five-coordinated anions [Mn(CO) 3 (α-diimine)] − from fac -[Mn(X)(CO) 3 (α-diimine)] (X = halide) at low temperatures. *Recl. des Trav. Chim. des Pays-Bas* **114**, 565–570 (1995).

13. Hawecker, J., Lehn, J.-M. & Ziessel, R. Electrocatalytic reduction of carbon dioxide mediated by Re(bipy)(CO) 3 Cl (bipy = 2,2′-bipyridine). *J. Chem. Soc., Chem. Commun.* 328–330 (1984) doi:10.1039/C39840000328.

14. Breikss, A. I. & Abruña, H. D. Electrochemical and mechanistic studies of Re(CO)3(dmbpy)CI] and their relation to the catalytic reduction of CO2. *J. Electroanal. Chem. Interfacial Electrochem.* **201**, 347–358 (1986).

15. Riplinger, C., Sampson, M. D., Ritzmann, A. M., Kubiak, C. P. & Carter, E. A. Mechanistic contrasts between manganese and rhenium bipyridine electrocatalysts for the reduction of carbon dioxide. *J. Am. Chem. Soc.* **136**, 16285–16298 (2014).

16. Grills, D. C., Ertem, M. Z., McKinnon, M., Ngo, K. T. & Rochford, J. Mechanistic aspects of CO2 reduction catalysis with manganese-based molecular catalysts. *Coord. Chem. Rev.* **374**, 173–217 (2018).

17. Sullivan, B. P., Bolinger, C. M., Conrad, D., Vining, W. J. & Meyer, T. J. One- and two-electron pathways in the electrocatalytic reduction of CO 2 by fac-Re(bpy)(CO) 3 Cl (bpy = 2,2′-bipyridine). *J. Chem. Soc., Chem. Commun.* 1414–1416 (1985) doi:10.1039/C39850001414.

18. Yang, W. *et al.* Electrocatalytic CO2 Reduction with Cis and Trans Conformers of a Rigid Dinuclear Rhenium Complex: Comparing the Monometallic and Cooperative Bimetallic Pathways. *Inorg. Chem.* **57**, 9564–9575 (2018).

19. Liu, L., Li, P. Z., Zhu, L., Zou, R. & Zhao, Y. Microporous polymelamine network for highly selective CO2 adsorption. *Polymer (Guildf).* **54**, 596–600 (2013).

20. Sampson, M. D. *et al.* Manganese Catalysts with Bulky Bipyridine Ligands for the Electrocatalytic Reduction of Carbon Dioxide: Eliminating Dimerization and Altering Catalysis. *J. Am. Chem. Soc.* **136**, 5460–5471 (2014).

21. Bard J. Allen, F. R. L. *ELECTROCHEMICAL METHODS*. (2001).

22. Qiu, S., Xue, M. & Zhu, G. Metal–organic framework membranes: from synthesis to separation application. *Chem. Soc. Rev.* **43**, 6116–6140 (2014).

23. Sumida, K. *et al.* Carbon Dioxide Capture in Metal–Organic Frameworks. *Chem. Rev.* **112**, 724–781 (2012).

24. Li, J.-R., Sculley, J. & Zhou, H.-C. Metal–Organic Frameworks for Separations. *Chem. Rev.* **112**, 869–932 (2012).

25. Nenoff, T. M. Hydrogen purification: MOF membranes put to the test. *Nat. Chem.* **7**, 377–378 (2015).

26. Yu, J. *et al.* CO 2 Capture and Separations Using MOFs: Computational and Experimental Studies. *Chem. Rev.* **117**, 9674–9754 (2017).

27. Das, S. K., Bhanja, P., Kundu, S. K., Mondal, S. & Bhaumik, A. Role of Surface Phenolic-OH Groups in N-Rich Porous Organic Polymers for Enhancing the CO 2 Uptake and CO 2 /N 2 Selectivity: Experimental and Computational Studies. *ACS Appl. Mater. Interfaces* **10**, 23813–23824 (2018).

28. Schwab, M. G. *et al.* Catalyst-free Preparation of Melamine-Based Microporous Polymer Networks through Schiff Base Chemistry. *J. Am. Chem. Soc.* **131**, 7216–7217 (2009).

Chapter IV

Molecular Graphene Quantum Dots (GQD): Materials for Catalytic and Optoelectronic Devices.

Introduction to GQDs.

Single sheets of graphene with sizes in both dimensions in the scale of few nanometers leads to what is called graphene quantum dots. Quantum dots (QDs) are in their own category of materials due to their unique structure-related properties, such as optical, electrical and optoelectrical. Graphene quantum dots GQDs (with size generally below 100 nm) are considered their own kind of QDs, as they are chemically and physically exceptionally stable because of their intrinsic inert carbon property, non-toxic and biologically safe. This class of materials is promising in particular for a reason: their electronic, optical, and spin properties can be in principle controlled by designing their size, shape and edges.[1–4]

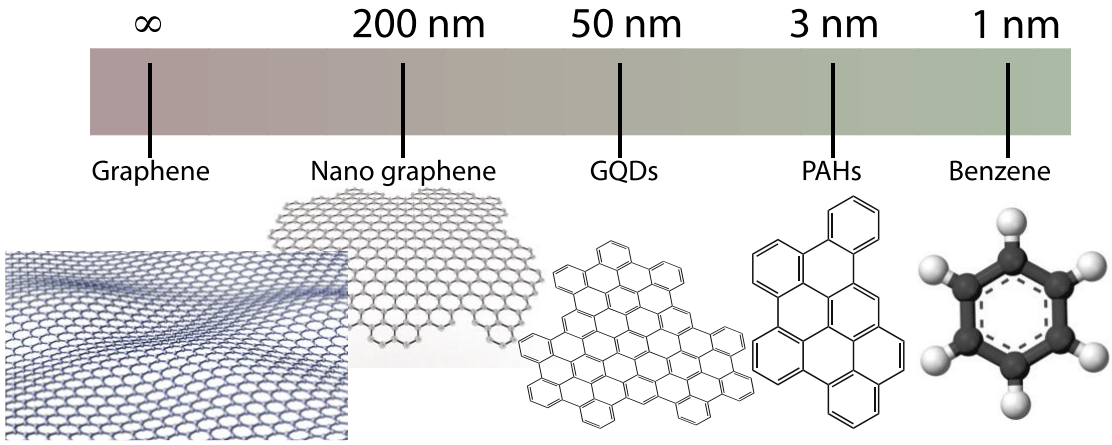

Scheme 1 Schematic illustration of graphene terminology defined according to their size scale. Classic graphene has a large enough structure that the edges do not participate to the overall characteristics of the material and the molecule can be modelled as virtually infinite. It is referred as nano graphene every sheet small enough to have a significant fraction of its carbon atoms on the edge greatly influencing its properties. GQDs are a subset of nano graphene where the quantum confinement of its valence electrons manifests a band gap.

The size of the π system is small enough that quantum mechanics makes the special properties arise. Due to quantum confinement effect, the electrons can be excited and

perform photoluminescence.[5,6] The quantum confinement effect is a phenomenon that happens when a particle is confined in a potential well smaller than the free roaming territory of its exciton. In other words, when the electron and hole pair generated by an excitation (exciton) is confined in a space smaller than twice of the Bohr radius, it takes quantized energy levels. Bohr radius refers to the size of the exciton (spatial distance between electron-hole pair). In an intuitive way to put it: when the particle is inside a room small enough that can "feel" its walls, it stops behaving as a classical object (Figure 1).

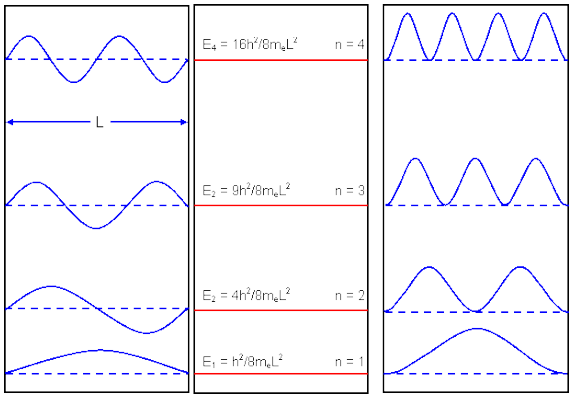

Figure 1 The easely recognizable "particle in a box" model. If the "walls" are close enough, the energy levels have appreciable gaps between them.

It is now clear why size and shape are so central in QDs research; smaller size leads to a larger bandgap, which result in shorter wavelength photoluminescence. The high photoluminescence and the low toxicity make GQDs promising tools for bioimaging, were the bigger systems are preferred as red and near infrared (NIR) photons have longer penetration depth through biological tissues.[7,8] Generally, with an increasing size of the conjugated system, or with increasing degree of functionalization, GQDs express more red-shifted emission. Nevertheless, the complex ecosystem for this class of materials is not entirely so straightforward and the precise tuning of their photoluminescence has not yet been achieved.

Also, QDs have been investigated as photosensitizers for photocatalysis.[9,10] Upon light absorption, they supply electrons to an electrocatalyst, however do not participate in the catalyzed reactions and do not improve the energy efficiency of the electrocatalysis. But recently, GQDs have been also tested as a ligand for metal ions for electrocatalytic and photocatalytic CO_2 reduction. With a tightly controlled nanographene structure, the resulting system was a well-defined molecular nanographene-rhenium complex with the

nanographene as an integral part of the catalyst itself. Electron delocalization over the ligand and the metal ion significantly decrease the electrical potential needed for the CO_2 reduction, resulting in a highly selective reaction to CO.[11] In this case the QD part both photosensitized and improved overall catalytic performances, adding to this category of materials the potential to be a useful tool in the field of catalysis too. As good progress has been made with metal-porphyrin systems for CO_2 reduction using highly available first row transition metals,[12–18] it was interesting for us to explore a similar approach using Zn-porphyrin derivatives, studying the possibility of expanding the electron delocalization using ligands containing pendant polyaromatic systems.

Molecular GQDs

GQDs have been mostly synthesized by top–down approaches, such as the oxidation of carbon fibers or graphene.[19,20] These methods are excellent for producing big quantities of nanoparticles but such particles do not have all the same molecular structure, as are more of a cluster of different similar systems near in size to each other that make them not suitable to produce well-defined properties. Bottom–up synthesis is able to achieve samples of GQDs with coherent chemical structure, and in the last decade efficient methods have been developed opening the way to a precise control of the GQD structure. However, these materials often face the problems of aggregation, that hinder the possibility to make the link between their structure and their intrinsic properties.[21,22] Bottom-up approaches involves the synthesis of the GQDs from molecular precursors, mostly benzene derivatives, that are condensed to form bigger systems. Few examples of these systems are shown, below, in Scheme 2.

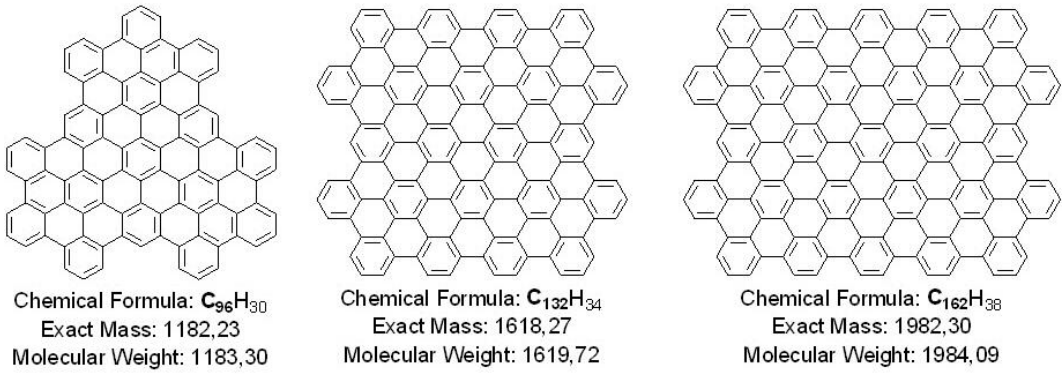

Scheme 2 Three examples of graphene quantum dots. They can be viewed as large polycyclic aromatic hydrocarbons (PAH) or as very small graphene sheets, but in this "middle-ground" size range (≈10 nm from edge to edge) they show characteristic properties like semi-conductivity or a very efficient one-photon emission in the visible and NIR range.

The small size of a GQD opens a band gap between π and π* orbitals that in normal graphene is otherwise absent, giving to this class of materials semiconductor and photoluminescence emission properties. The good single-photon emission, brightness, and photostability of GQDs have been already characterized showing that they are very promising materials for applications requiring single photon emitters.[23]

Electrochemical and Spectroelectrochemical Characterization of Molecular Graphene Quantum Dots (GQD)

Methods and Principles

The study of the electrochemical properties of the sample materials in this work have been carried out by Cyclic Voltammetry (CV) and spectrophotometry. The intent was to obtain information on the energy levels accessible by photochemistry and electrochemistry which are directly influenced by the size, shape and functionalization of the π system.

The Spectrophotometer

Spectrophotometry is a quantitative technique that measures the wavelengths of light and how much of it a substance is able to absorb as a way to understand its molecular peculiarities. These measurements are carried out using a spectrophotometer, a device comprising a light source comprehensive of wavelengths from UV to NIR, a monochromator that selects the light to send through the sample, the sample holder, a detector that collects the light passing through and a signal amplifier. The sample, usually in solution, is kept inside a transparent cuvette of known optical pathlength and is positioned in the dark chamber.

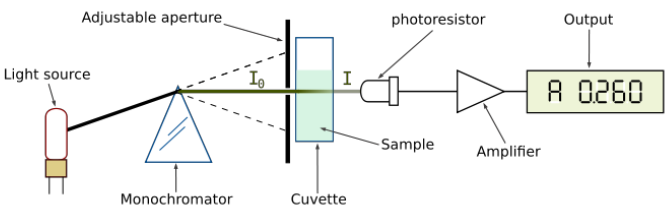

Scheme 3 Schematic representation of the fundamental parts in a spectrophotometer device.

The light transmission logarithmic data is used to plot the sample response in an *absorbance* (A) vs *wavelength* (λ) graph. Absorbance is defined in terms of the fraction of light passing through the sample (*transmittance*), as follows:

$$A = -log_{10}(T)$$

Were T being a number comprised between 1 (total transmittance) and 0 (no transmittance). Transmittance and absorbance contain the same information about how much light has been absorbed or scattered by the sample, but the logarithmic nature of absorbance makes it a better quantity to work with the exponential nature of light absorption from matter. The Lambert-Beer law relates linearly absorbance A to concentration c and the optical path length l:

$$A = \varepsilon lc$$

Here ε is the absorptivity coefficient specific of the analyte. By knowing l (the pathlength of the cuvette) and c, is possible to convert the A vs λ graph into a ε vs λ graph. The absorption of light is due to the interaction of the photon with the electronic and vibrational modes of molecules and this depends on the molecular structure.

Molecular GQD and Extended π Systems for NIR Single Photon Emission

In this thesis one of these graphene quantum dot systems, here referred as *C96*, was analyzed by electrochemical and photophysical means. Together with other three systems, labelled as Zn-SNP, Zn-SAP and Zn-SPP (see Scheme 3) that were electrochemically characterized by voltammetry. These porphyrins can be used as precursors to obtain π-extended metal-containing planar systems by thermal treatment, as shown in Scheme 4 and labeled as *fused-1*, *fused-2* and *fused-3*. Such π-extended nanostructures can be seen as porphyrins with an extended skeleton that is able to participate to the delocalization of the electrons and thus exhibit structures, electronic and optical properties significantly different from those of the parent porphyrins in what starts to become an hybrid between metal-organic emitter and a GQD.[24–32] Recent works demonstrated that anthracene or anthracene-like moieties could be fused on the porphyrin core leading to a large shift of the absorption properties toward the NIR. The general term of "fusion" describes the set of reactions able to connect molecular fragments to the porphyrin core by at least two bonds that prevent the free rotation between subunits, flatten the molecular assemblies and afford fully conjugated systems. The fusion of PAHs on porphyrins is achieved by thermal treatment of the parent porphyrins (Zn-SNP, Zn-SAP and Zn-SPP) in a tubular quartz oven under a nitrogen atmosphere. Here we were interested in the electrochemical characterization of the precursor species and their eventual planarization by electrochemistry. The investigation of redox behavior of the Zn-porphyrin species Zn-SNP, Zn-SAP and Zn-SPP, bearing PAH moieties, has been carried out in highly dry dichloromethane solution, devoting particular attention to the oxidation processes.

The species C96 was characterized by UV-Vis-NIR spectroscopy for which a solution or suspension of single molecules isolated systems was necessary. It must be noticed that even a pure sample of GQD is hard to precisely characterize as the single sheets easily stack upon each other, and in dry conditions particles of heights up to 4 nm (10 sheets) have been reported.[33] Staked molecules strongly interact leading to observed behaviors that resemble very little to the single isolated system. In previous works reported in literature,[34,35] similar nanostructures were successfully maintained in solutions in anionic form for indefinite time using chemical reduction. The complete dissolution of a given drop-casted quantity of a sample, to obtain a solution of appreciable concentration, would

be desirable for further experimentation with the system. For instance, in line with the main aim of this thesis, an interesting route would be to synthetize non-noble metal nanoparticles on the graphene molecules, thus creating a composite system similar to some examples that have shown to give good results for HER and ORR.[36] To obtain a single molecule species of C96 in solution for photo-physical characterization a spectro-electrochemical setup was used. Inside a spectrophotometer a special 1 mm glass cuvette was inserted in the sample holder. This cuvette is designed to be an electrochemical cell able to house working electrode (WE), counter (CE) and reference electrodes (RE) connectable to a potentiostat outside the spectrophotometer. The chosen working electrode was a platinum net were the sample can be drop-casted on letting light from the spectrophotometer to still pass through. By reducing C96 to $[C96]^-$ the electrostatic repulsive forces of the delocalized added electron should break the cluster while not altering significantly the properties.

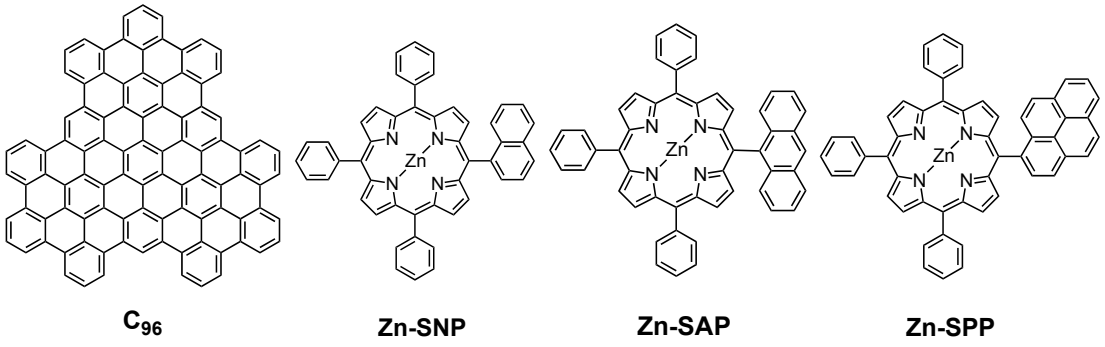

Scheme 4 The structure of the four species analyzed in this section: the GQD C96 and the three precursors porphyrins.

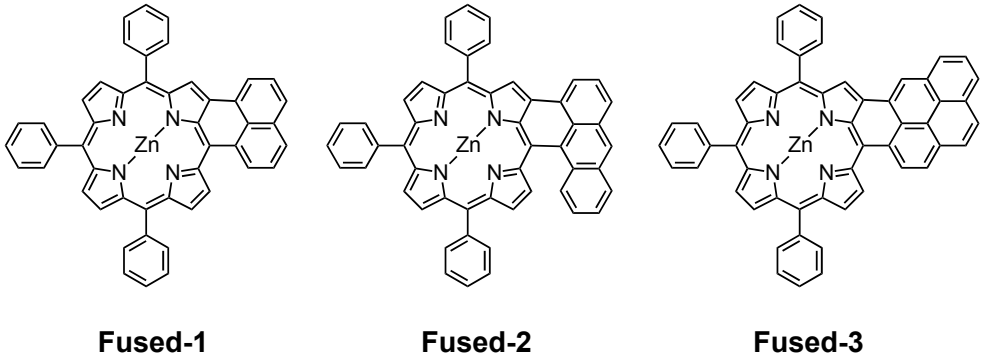

Scheme 5 The structure of the three π-extended porphyrins.

Experimental Section

Materials and General Experiments.

The C96 molecular system have been synthesized in two simple steps using readily available materials. The Diels–Alder reaction of commercially available 1,3,5-triethynylbenzene with excess 2,3,4,5-tetraphenylcyclopenta-2,4-dien-1-one in o-xylene at 180 °C gave the corresponding polyphenylene compounds in nearly quantitative yields (Scheme 6).[37] The second step is the oxidative cyclodehydrogenation of polyphenylene precursors with nitromethane.[38]

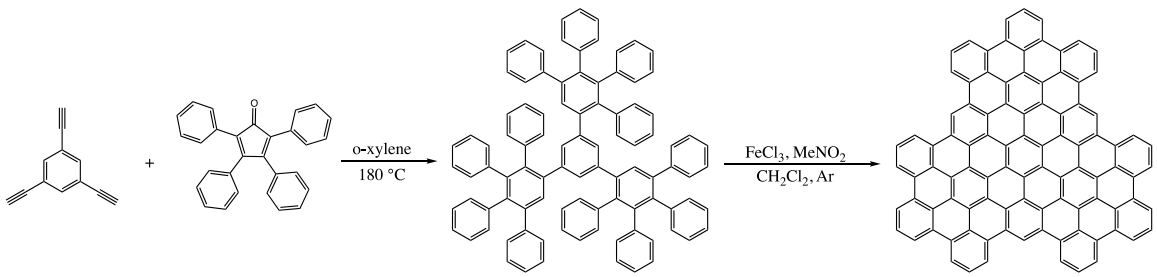

Scheme 6 Reaction route to the production of C96.

The spectroelectrochemical experiments have been carried out using a quartz OTTLE (optically transparent thin layer electrode) cell acting as cuvette with a 0.03 cm optical path length. The body of the cell is constructed from PTFE. The cuvette was custom-built by Heraeus Silica and Metals Ltd. (Byfleet, England) from Infrasil quartz; it has a reservoir area attached to the top to hold the reference and auxiliary electrodes. Additional Infrasil quartz windows (0.4 mm thick) on either side of the cuvette create compartments immediately adjacent to the cuvette. Temperature control was achieved by using two N_2 flows, one at room temperature and one which was cooled (by passing it through a coiled tube in a dewar of liquid N_2), being passed through these compartments in contact with the cuvette optical surfaces. The tube carrying the cold N_2 was insulated to prevent ice build-up. The two flow rates could each be controlled independently by means of a needle valve (Jencons, item 313-018) attached to a flow-meter (Jencons, tem 315-045) in each N_2 path, and by varying the relative flow rates of warm and cold components the temperature at the cuvette could be varied between room temperature and -50 °C with an accuracy of better

than ±0.5°C. The temperature at the cuvette was monitored with a thermocouple attached to a digital thermometer (CAL-9000). To prevent condensation on the outer surfaces of the cold Infrasil windows the sample compartment of the spectrometer was kept purged with dry N_2 at room temperature. The working electrode was a Pt–Rh (90 : 10) gauze with about 45 wires per centimeter and a wire thickness of 0.06 mm (manufactured by Engelhard-CLAL, Chessington, England); this results in an optical transparency of about 40%. The auxiliary electrode was a thick Pt wire, and the reference electrode was an Ag–AgCl electrode; these were inserted into the reservoir at the top of the cuvette, isolated from the bulk of the solvent by glass frits. The potentials were applied using an Amel model 552 potentiostat connected to an Amel model 566 function generator, and spectra were recorded approximately every 2 to 5 min. Reversibility was checked by reversing the potential. All the spectra have been recorded by a Varian Cary 5.

Before drop cast, C96 was suspended with concentration 1 g/L in Ethanol (EtOH, 99.5%, Sigma-Aldrich), by ultrasonicating for 20 minutes and leaving afterward under stirring to prevent that the material aggregates back to macroscopic grains. The suspension was then drop-casted onto the Pt–Rh gauze WE for photoelectrochemical characterization.

Species Zn-SNP, Zn-SAP and Zn-SPP were characterized via cyclic voltammetry. During these CV measurements, electrochemical or analytical grade tetrabutylammonium hexafluorophosphate (TBAH) from Sigma-Aldrich was used as received as a supporting electrolyte. Solvent dichloromethane (DCM) from Sigma-Aldrich was purified and dried by refluxing over and successively distilling from B_2O_3 and activated 4 Å molecular sieves. Afterward, it was stored in specially designed Schlenk flasks over 3 Å activated molecular sieves, protected from light, and kept under vacuum prior to use, as reported elsewhere.

The solvent was distilled via a closed system into a custom designed electrochemical cell containing the supporting electrolyte and the species under examination, immediately before performing the experiment. Electrochemical experiments were carried out in an airtight single-compartment cell using platinum as working and counter electrodes and a silver spiral as a quasi-reference electrode. The drift of the quasi-reference electrode was negligible during the time required for an experiment. All the $E_{1/2}$ potentials have been directly obtained from cyclic voltammetric curves as averages of the cathodic and anodic peak potentials and by digital simulation in the case of not Nernstian or overlapping processes. The $E_{1/2}$ values have been determined by adding ferrocene (Fc), at the end of

each experiment, as an internal standard and measuring them with respect to the ferrocinium/ferrocene couple ($Fc^{+/0}$) standard potential (at 298 K it is +0.42 V vs SCE, i.e., the aqueous Saturated Calomel Electrode). The cell containing the supporting electrolyte and the electroactive compound was dried under vacuum at 100 - 110 °C for at least 48 hours before each experiment. The pressure measured in the electrochemical cell prior to perform the trap-to-trap distillation of the solvent was typically $1x10^{-5}$ mbar. Voltammograms were recorded with a custom made fast and low current potentiostat controlled by an AMEL Mod. 568 programmable function generator. The potentiostat was interfaced to a Nicolet Mod. 3091 digital oscilloscope and the data transferred to a personal computer by the program Antigona. Minimization of the uncompensated resistance effect in the voltammetric measurements was achieved by the positive-feedback circuit of the potentiostat. Digital simulations of the cyclic voltammetric curves were carried out either by Antigona or DigiElch 7, utilizing a best fitting procedure of the experimental curves recorded at different scan rates spanning over, at least, two orders of magnitude.

C96 Spectroelectrochemical Characterization

Spectroelectrochemical investigation of the GQD was carried out at room temperature in THF using TBAH as electrolyte with a concentration of 27 mM. This unusually low TBAH concentration is to prevent flocculation of the analyte as this family of systems are highly responsive to the ionic power of the medium they are in and, therefore, hard to maintain dissolved.

The UV-vis spectra of C96 here discussed shows the evolution of absorbance as the concentration of the reduced species increases in solution. Starting from a polarization of -1.1 V the insoluble C96 deposited on the platinum gauze was slowly reduced to its anionic form ($[C96]^-$) and dissolved into solution. Due to electrostatic repulsion, the reduced species is easily observed as an isolated single molecule in solution. The polarization was continuously applied for the entire duration of the experiment and absorbance spectra were taken 5 minutes apart from each other. The voltage was increased four times (-1.5 V, -1.8 V, -2.2 V, -2.4 V), as the difference in absorbance between two consecutive measurements became not appreciable. After a total elapsed time of 3 and a half hours the potential was reversed to 0.0 V (and subsequently to +0.5 V and +0.8 V) to observe the re-oxidation of C96 and hence its flocculation in the electrolyte solution.

At least 6 peaks of which two especially prominent are shown in Figure 2 at wavelength λ=229 nm and 289 nm. The 289 nm peak is positioned were a typical graphene absorption is expected.[39] A 274 nm peak starting to grow after the potential exceeded -1.8 V is probably due to a second species coming from the degradation of C96 (Figure 2b). After 3 and a half hours, unfortunately, only a small fraction of the material was transferred to the solution, not really enough compared to that required in a synthetic experiment. Thus, the investigation of such a nano-system was limited only to its fundamental aspects.

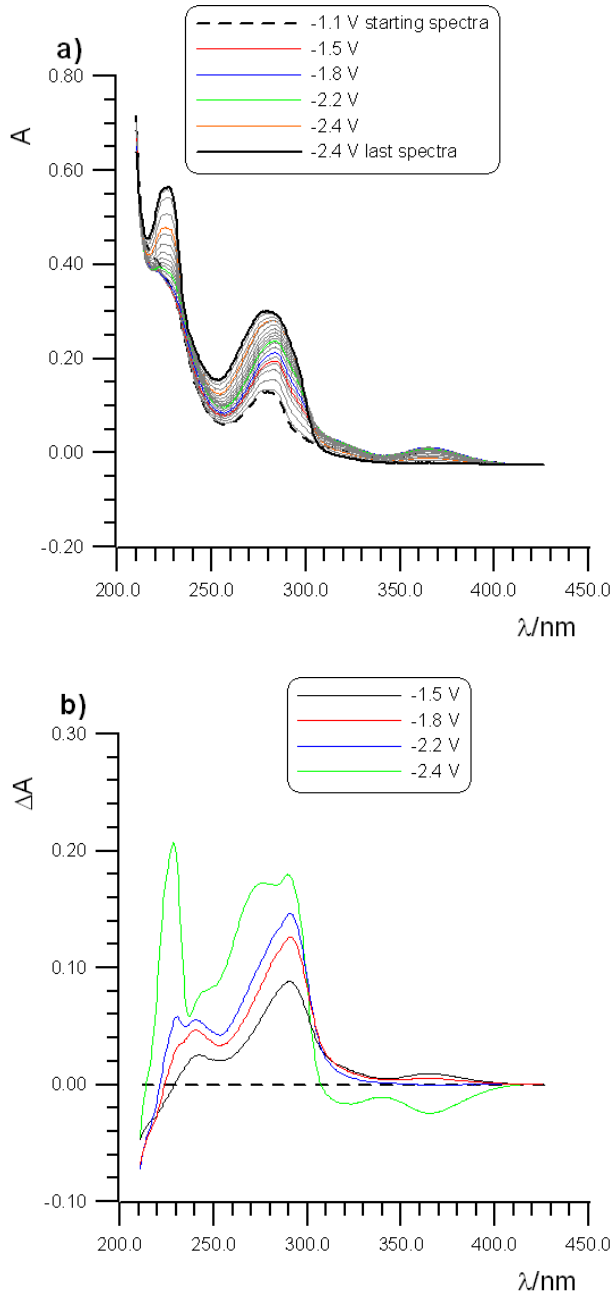

Figure 2 UV-vis spectroelectrochemistry of a C96 dropcasted on the Pt gauze being reduced and dissolved in TBAH/THF 27 mM. In (a) is shown the evolution of the absorbance during the process of reduction, every coloured line reported represent an increase in applied voltage. Voltage was increased when dissolution slowed too much. Same data (b) edited to show the difference spectra (spectrum of the pristine drop cast subtracted) to highlight the contrimution of the $C96^{-}$ species dissolving. Dashed line represent the starting specta in both graphs.

During the reduction process the isosbestic point moved (blue-shifted) by 20 nm, indicating that either a second reduction process was happening or a chemical modification of reduced C96 was occurring (Figure 3a). The last curve was taken at an applied potential of –2.4 V, after that the potential was reverted back to 0.0 V and slowly increased with steps to + 0.5 V and +0.8 V, observing a slow oxidation and flocculation of the dissolved C96 anion (Figure 3b).

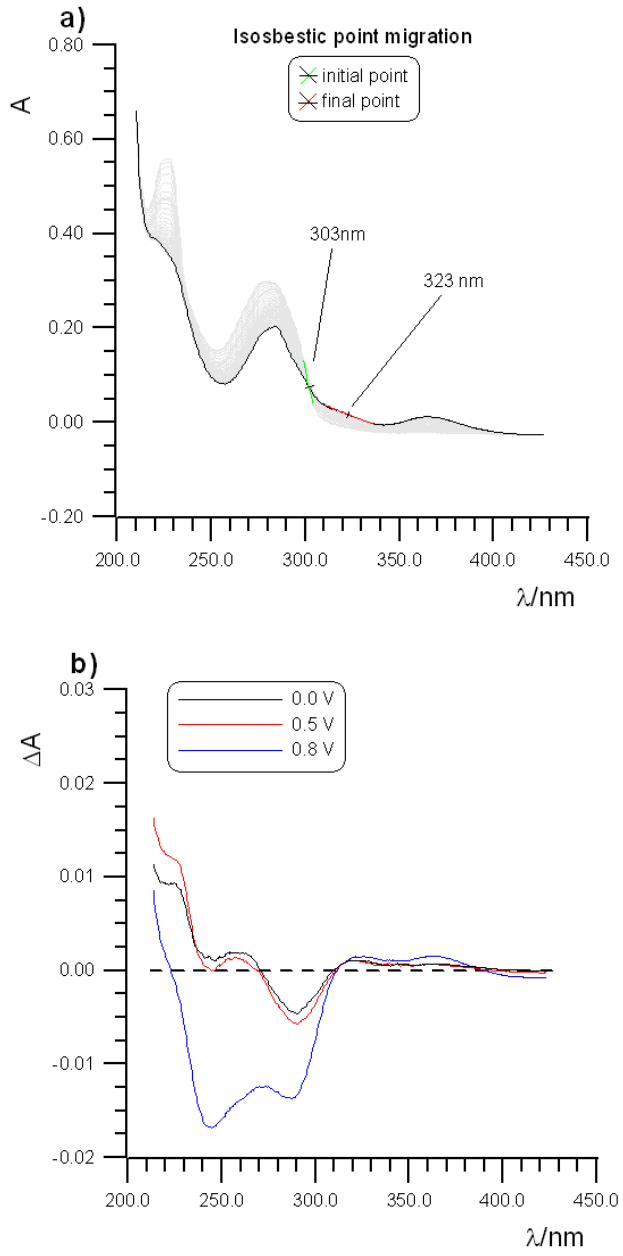

Figure 3 UV-vis spectroelectrochemistry of a C96 dropcasted on the Pt gauze. Graph (a) shows the migation of the isosbestic point between the starting spectra and the second spectra (black and red line crossing) and the starting spectra and the last spectra (black and green line crossing). In (b) is shown the difference spectra (spectrum of the last scan during reduction subtracted) during the process of oxidation.

Porphyrins Characterization

The cyclic voltammetric curves of the three porphyrins sketched in Scheme 4 are reported in Figure 4. For all the compounds the redox processes studied are within the potential window comprised between about -1.5 V and +2.4 V and the redox processes occur at the

positive potential region. The species show globally 4, 3 and 4 voltammetric waves for Zn-SAP, Zn-SNP and Zn-SPP respectively. The species Zn-SAP and Zn-SPP show the first three peaks as reversible voltammetric one-electron transfers while the last peak is a completely irreversible process that happens at the foot of a subsequent oxidation that has not been further investigated.

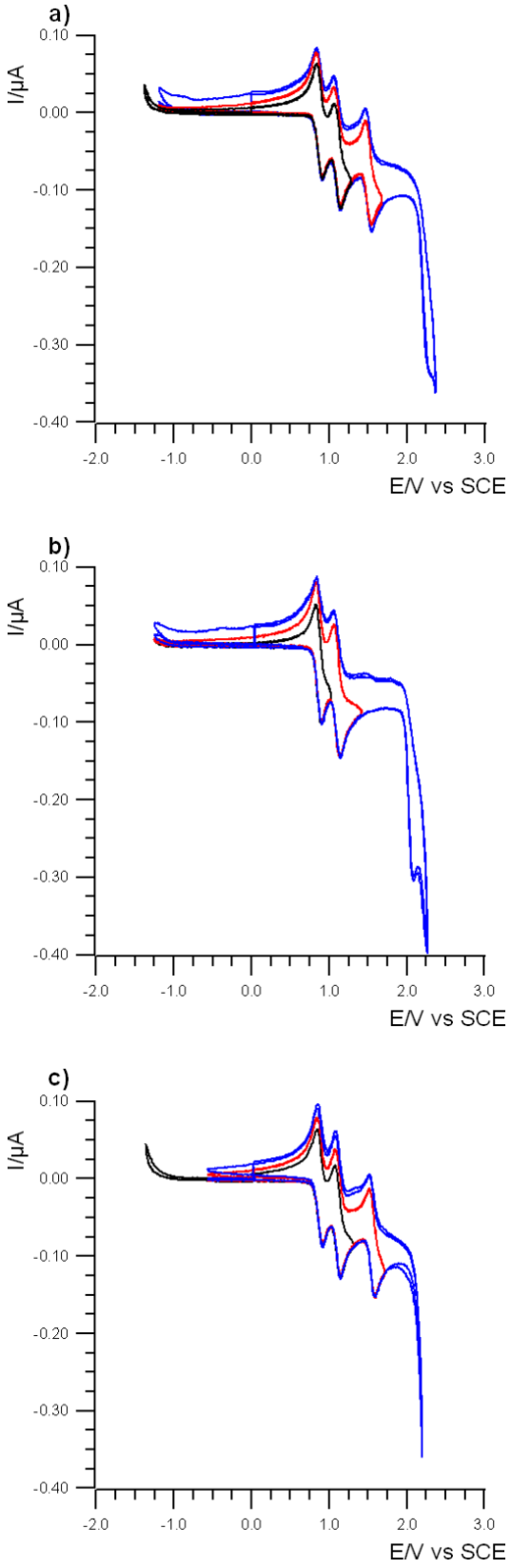

Figure 4 Cyclic voltammetric curves of 0.8 mM porphyrin (a) Zn-SAP, (b) Zn-SNP and (c) Zn-SPP recorded in TBAH/DCM at 298 K; scan rate: 1 V/s; WE: Pt disk (diameter 125 µm); RE: SCE.

The prophyrin Zn-SNP at odd with the other two homologue species shows the first two oxidations as reversible processes whereas the third one is completely irreversible. The $E_{1/2}$ potentials of the various processes are collected in Table 2. From an electronic point of view, the three porphyrins can be considered as constituted by two nearly independent moieties: the porphyrinic ring and the polyaromatic fragment, that are mostly arranged in a perpendicular conformation with respect to each other. Therefore, it is possible to attribute the main localization of the electron transfers on the basis of comparison of the redox potentials of the various species.

Table 1 Half-Wave ($E_{1/2}$) redox potentials (vs SCE) of porphyrin compounds recorded in TBAH/DCM solution at 25 °C. Marked as (a) are irreversible processes and (b) computationally predicted processes.

Species	**$E_{1/2}$(oxidation) / V**			
	I	***II***	***III***	***IV***
Zn-SAP	0.87	1.10	1.51	2.30[a]
Zn-SNP	0.87	1.10	2.09[a]	
Zn-SPP	0.88	1.11	1.57	2.23[ab]

Thus, from the values in Table 2 it is evident that the first two oxidations are centered on the porphyrinic moiety for all the compounds whereas the following ones interest the polyaromatic fragment. Moreover, the species Zn-SNP shows only one oxidation localized on the naphthalene moiety, at a potential rather high with respect to the corresponding oxidations of the other species bearing anthracene and pyrene. This agrees with the oxidation potentials of the corresponding polyaromatic hydrocarbons. The third oxidation for the species Zn-SNP and the fourth one for both Zn-SAP and Zn-SPP are completely irreversible processes that bring about to the deposition of a conducting thin film on the electrode surface, which can be even visually seen as a colored deposit. As matter of facts, cycling repeatedly the potential scan up to include the irreversible process at about +2 V, the current starts to increase at each scan and new peaks starts to develop which cannot be attributed to the pristine molecule in solution. Such a voltammetric behavior is in line with

the deposition of a conducting polymer or a conducting film obtained by nanostructures made insoluble by some kind of a reaction of the parent molecule in solution. One hypothesis might be the planarization of the PAH moiety with the porphyrinic core, as the oxidation of polyaromatic hydrocarbon, under our experimental conditions, are known to undergo an intramolecular Carbon-Carbon coupling.[40] A mass spectra investigation of the film deposited on ITO electrode substrate, through MALDI-TOF technique, did not give a clear evidence about the chemical nature of such a deposit and further experiments are currently undergoing.

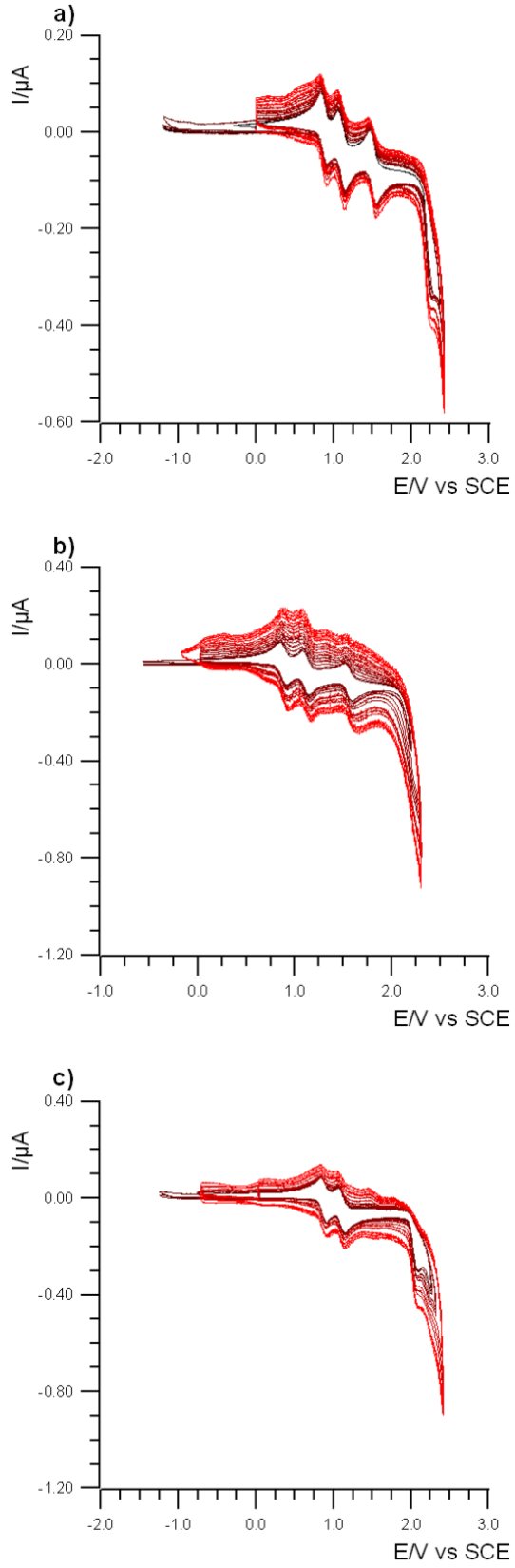

Figure 5 Multiscan Cyclic voltammetric curves of 0.8 mM porphyrin (a) Zn-SAP, (b) Zn-SPP and (c) Zn-SNP recorded in TBAH/DCM at 298 K; scan rate: 1 V/s; WE: Pt disk (diameter 125 µm); RE: SCE.

Conclusions

To conclude, in this chapter we have worked to expand our knowledge on the physical chemistry of GQDs and more in general the effect of an extended π system integrated to well established catalysts. As said before, GQDs are already used as sensitizers in photocatalysis working in tandem with the actual catalyst or pre-catalyst; the possibility to have great control over their size and shape during synthesis and, also, the ability to directly build supramolecular systems were the GQD becomes part of the catalyst influencing its energy levels allow us to customize them are mayor tools in our toolbox for the search for better materials. As the space of possibility is wide, there is still much to be studied on the physics and chemistry of these molecules, especially the bigger and more complex ones.

Here spectroelectrochemical measurements were conducted in THF of a solid sample of a GQD containing 96 carbon atoms, here simply referred as C96, drop-casted on a Pt gauze. The material was reduced in an anionic state, $[C96]^-$, only in small amounts by applying a constant potential in inert atmosphere and thermostatic environment. The anions repelled by electrostatic forces from each other and their increased affinity for the polar solvent allowed the cast deposit to be dissolved and their absorption spectra could be analyzed. The process was partially reversible, with the re-oxidation of the material and its flocculation. The appearance of a new peak in by having the applied potential exceed -1.5 V alongside with a blueshift of the isosbestic point between consecutive scans suggests partial decomposition of the C96 molecule. The quantities of dissolved material were scarce and no further investigation was attempted of the obtained $[C96]^-$ sample.

Three Zn porphyrin complexes dissolved in DCM were electrochemically characterized by CV between a potential window comprised between about -1.5 V and +2.4 V in Ar atmosphere. The three systems differed by the PAH attached covalently to the porphyrin ring. The three PAH being naphthalene, anthracene, and 1,9-dihydropyrene derivates groups. The results showed the porphyrin and the PAH behaving as separate entities. The voltammograms showed two low potential oxidation processes identifiable as porphyrin centered and others high potential oxidations corresponding to the equivalent PAH molecule. This kept identity of the two moieties is in contrast to the highly changed behavior of the fused product, where the system act as a single entity. At higher oxidation potentials the formation of a conducting film on the electrode surface would suggest that a

planarization of the PAH moiety with the porphyrin one is occurred or some other kind of dimerization (eventually oligomerization) can be hypothesized. Further mass and microscopy characterizations on the deposited film are currently undergoing to infer such an hypothesis.

References

1. Tomović, Ž., Watson, M. D. & Müllen, K. Superphenalene-Based Columnar Liquid Crystals. *Angew. Chemie Int. Ed.* **43**, 755–758 (2004).
2. Debije, M. G. *et al.* The Optical and Charge Transport Properties of Discotic Materials with Large Aromatic Hydrocarbon Cores. *J. Am. Chem. Soc.* **126**, 4641–4645 (2004).
3. Yan, X., Cui, X. & Li, L. Synthesis of Large, Stable Colloidal Graphene Quantum Dots with Tunable Size. *J. Am. Chem. Soc.* **132**, 5944–5945 (2010).
4. Konishi, A. *et al.* Synthesis and Characterization of Teranthene: A Singlet Biradical Polycyclic Aromatic Hydrocarbon Having Kekulé Structures. *J. Am. Chem. Soc.* **132**, 11021–11023 (2010).
5. Ponomarenko, L. A. *et al.* Chaotic Dirac Billiard in Graphene Quantum Dots. *Science (80-.).* **320**, 356–358 (2008).
6. Takagahara, T. & Takeda, K. Theory of the quantum confinement effect on excitons in quantum dots of indirect-gap materials. *Phys. Rev. B* **46**, 15578–15581 (1992).
7. Zhu, S. *et al.* Strongly green-photoluminescent graphene quantum dots for bioimaging applications. *Chem. Commun.* **47**, 6858 (2011).
8. Chong, Y. *et al.* The in vitro and in vivo toxicity of graphene quantum dots. *Biomaterials* **35**, 5041–5048 (2014).
9. Han, Z., Qiu, F., Eisenberg, R., Holland, P. L. & Krauss, T. D. Robust Photogeneration of H2 in Water Using Semiconductor Nanocrystals and a Nickel Catalyst. *Science (80-.).* **338**, 1321–1324 (2012).
10. Wu, K. & Lian, T. Quantum confined colloidal nanorod heterostructures for solar-to-fuel conversion. *Chem. Soc. Rev.* **45**, 3781–3810 (2016).
11. Qiao, X. *et al.* Well-Defined Nanographene-Rhenium Complex as an Efficient Electrocatalyst and Photocatalyst for Selective CO2 Reduction. *J. Am. Chem. Soc.* **139**, 3934–3937 (2017).
12. Davethu, P. A. & De Visser, S. P. CO2 Reduction on an Iron-Porphyrin Center: A Computational Study. *J. Phys. Chem. A* **123**, 6527–6535 (2019).
13. Lashgari, A. *et al.* Enhanced Electrocatalytic Activity of a Zinc Porphyrin for CO2 Reduction: Cooperative Effects of Triazole Units in the Second Coordination Sphere. *Chem. - A Eur. J.* 1–9 (2020) doi:10.1002/chem.202002813.
14. Zhu, M. *et al.* Inductive and electrostatic effects on cobalt porphyrins for heterogeneous electrocatalytic carbon dioxide reduction. *Catal. Sci. Technol.* **9**,

974–980 (2019).

15. Zhao, H.-Z., Chang, Y.-Y. & Liu, C. Electrodes modified with iron porphyrin and carbon nanotubes: application to CO2 reduction and mechanism of synergistic electrocatalysis. *J. Solid State Electrochem.* **17**, 1657–1664 (2013).
16. Mohamed, E. A., Zahran, Z. N. & Naruta, Y. Efficient electrocatalytic CO 2 reduction with a molecular cofacial iron porphyrin dimer. *Chem. Commun.* **51**, 16900–16903 (2015).
17. Okabe, Y., Lee, S. K., Kondo, M. & Masaoka, S. Syntheses and CO2 reduction activities of π-expanded/extended iron porphyrin complexes. *J. Biol. Inorg. Chem.* **22**, 713–725 (2017).
18. Sinha, S. & Warren, J. J. Unexpected Solvent Effect in Electrocatalytic CO 2 to CO Conversion Revealed Using Asymmetric Metalloporphyrins. *Inorg. Chem.* **57**, 12650–12656 (2018).
19. Li, L. *et al.* Focusing on luminescent graphene quantum dots: current status and future perspectives. *Nanoscale* **5**, 4015 (2013).
20. Bacon, M., Bradley, S. J. & Nann, T. Graphene Quantum Dots. *Part. Part. Syst. Charact.* **31**, 415–428 (2014).
21. Müllen, K. Evolution of Graphene Molecules: Structural and Functional Complexity as Driving Forces behind Nanoscience. *ACS Nano* **8**, 6531–6541 (2014).
22. Zhao, S. *et al.* Fluorescence from graphene nanoribbons of well-defined structure. *Carbon N. Y.* **119**, 235–240 (2017).
23. Zhao, S. *et al.* Single photon emission from graphene quantum dots at room temperature. *Nat. Commun.* **9**, 3470 (2018).
24. Mori, H., Tanaka, T. & Osuka, A. Fused porphyrinoids as promising near-infrared absorbing dyes. *J. Mater. Chem. C* **1**, 2500 (2013).
25. Yamane, O. *et al.* Pyrene-Fused Porphyrins: Annulation Reactions of meso-Pyrenylporphyrins. *Chem. Lett.* **33**, 40–41 (2004).
26. Kurotobi, K., Kim, K. S., Noh, S. B., Kim, D. & Osuka, A. A Quadruply Azulene-Fused Porphyrin with Intense Near-IR Absorption and a Large Two-Photon Absorption Cross Section. *Angew. Chemie Int. Ed.* **45**, 3944–3947 (2006).
27. Tanaka, M. *et al.* Novel unsymmetrically π-elongated porphyrin for dye-sensitized TiO 2 cells. *Chem. Commun.* 2069–2071 (2007) doi:10.1039/B702501G.
28. Davis, N. K. S., Thompson, A. L. & Anderson, H. L. Bis-Anthracene Fused Porphyrins: Synthesis, Crystal Structure, and Near-IR Absorption. *Org. Lett.* **12**,

2124–2127 (2010).

29. Lewtak, J. P. *et al.* Naphthalene-fused metallo-porphyrins–synthesis and spectroscopy. *Org. Biomol. Chem.* **9**, 8178 (2011).
30. Davis, N. K. S., Thompson, A. L. & Anderson, H. L. A Porphyrin Fused to Four Anthracenes. *J. Am. Chem. Soc.* **133**, 30–31 (2011).
31. Diev, V. V. *et al.* Porphyrins Fused with Unactivated Polycyclic Aromatic Hydrocarbons. *J. Org. Chem.* **77**, 143–159 (2012).
32. Chen, Q. *et al.* Synthesis of Triply Fused Porphyrin-Nanographene Conjugates. *Angew. Chemie Int. Ed.* **57**, 11233–11237 (2018).
33. Pierrat, P. & Gaumet, J.-J. Graphene quantum dots: Emerging organic materials with remarkable and tunable luminescence features. *Tetrahedron Lett.* **61**, 152554 (2020).
34. Vallés, C. *et al.* Solutions of Negatively Charged Graphene Sheets and Ribbons. *J. Am. Chem. Soc.* **130**, 15802–15804 (2008).
35. Pénicaud, A., Poulin, P., Derré, A., Anglaret, E. & Petit, P. Spontaneous Dissolution of a Single-Wall Carbon Nanotube Salt. *J. Am. Chem. Soc.* **127**, 8–9 (2005).
36. Liu, M. *et al.* Carbon supported noble metal nanoparticles as efficient catalysts for electrochemical water splitting. *Nanoscale* **12**, 20165–20170 (2020).
37. Ogliaruso, M. A., Romanelli, M. G. & Becker, E. I. Chemistry of Cyclopentadienones. *Chem. Rev.* **65**, 261–367 (1965).
38. Kovacic, P. & Jones, M. B. Dehydro coupling of aromatic nuclei by catalyst-oxidant systems: poly(p-phenylene). *Chem. Rev.* **87**, 357–379 (1987).
39. Catheline, A. *et al.* Graphene solutions. *Chem. Commun.* **47**, 5470 (2011).
40. Ussano Eleonora. Electrochemistry of molecular systems for new nanostructured materials and bioelectronic devices. (ALMA MATER STUDIORUM, UNIVERSITÀ DI BOLOGNA, 2016).